ISSN: 2153-1196 Volume 10, Number 11, October 2019

Scientific Research Publishing

Journal of Modern Physics

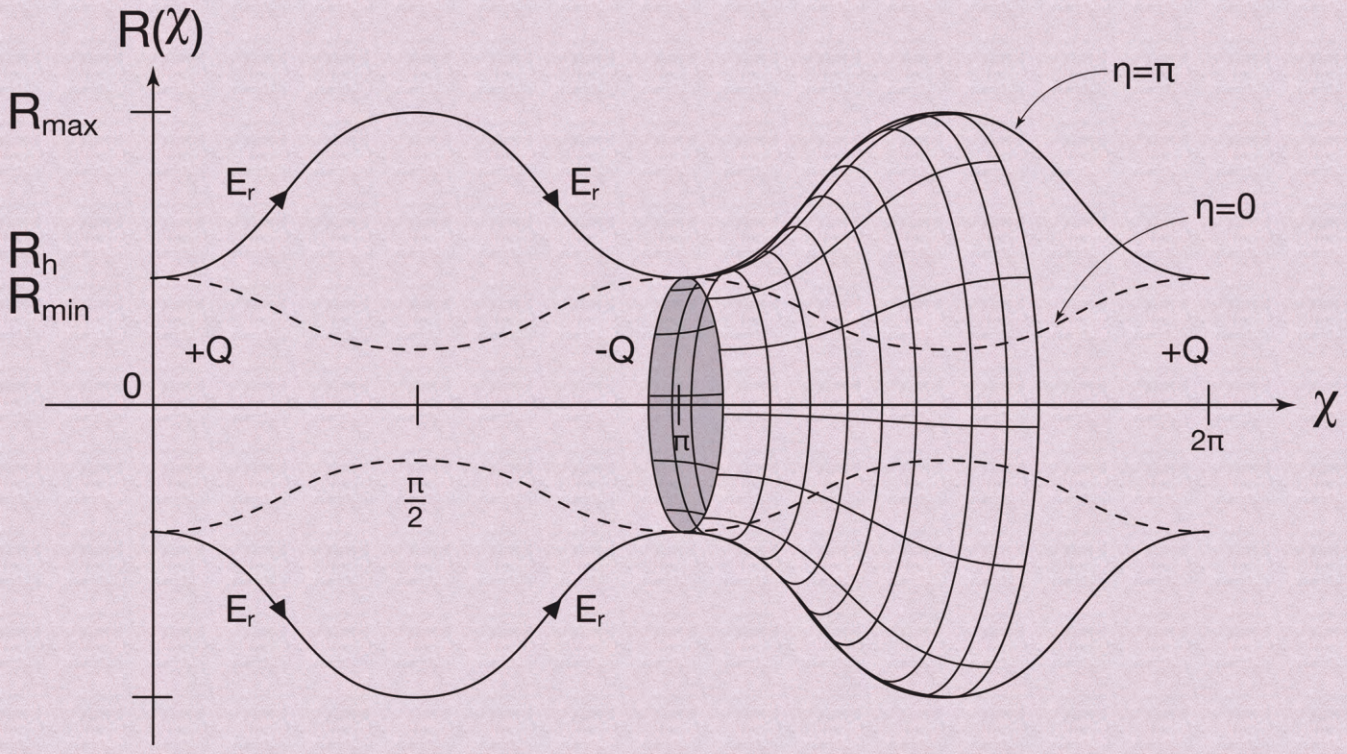

ISSN: 2153-1196
9 772153 119007 11

https://www.scirp.org/journal/jmp

Journal Editorial Board

ISSN: 2153-1196 (Print) ISSN: 2153-120X (Online)
https://www.scirp.org/journal/jmp

Editor-in-Chief

Prof. Yang-Hui He	City University, UK

Editorial Board

Prof. Nikolai A. Sobolev	Universidade de Aveiro, Portugal
Dr. Mohamed Abu-Shady	Menoufia University, Egypt
Dr. Hamid Alemohammad	Advanced Test and Automation Inc., Canada
Prof. Emad K. Al-Shakarchi	Al-Nahrain University, Iraq
Prof. Tsao Chang	Fudan University, China
Prof. Stephen Robert Cotanch	NC State University, USA
Prof. Peter Chin Wan Fung	University of Hong Kong, China
Prof. Ju Gao	The University of Hong Kong, China
Prof. Sachin Goyal	University of California, USA
Dr. Wei Guo	Florida State University, USA
Prof. Cosmin Ilie	Los Alamos National Laboratory, USA
Prof. Haikel Jelassi	National Center for Nuclear Science and Technology, Tunisia
Prof. Santosh Kumar Karn	Dr. APJ Abdul Kalam Technical University, India
Prof. Christophe J. Muller	University of Provence, France
Prof. Ambarish Nag	National Renewable Energy Laboratory, USA
Dr. Rada Novakovic	National Research Council, Italy
Prof. Tongfei Qi	University of Kentucky, USA
Prof. Mohammad Mehdi Rashidi	University of Birmingham, UK
Dr. A. L. Roy Vellaisamy	City University of Hong Kong, China
Prof. Yuan Wang	University of California, Berkeley, USA
Prof. Fan Yang	Fermi National Accelerator Laboratory, USA
Prof. Peter H. Yoon	University of Maryland, USA
Prof. Meishan Zhao	University of Chicago, USA
Prof. Pavel Zhuravlev	University of Maryland at College Park, USA

Scientific Research Publishing

Journal of Modern Physics, 2019, 10, 1299-1400
https://www.scirp.org/journal/jmp
ISSN Online: 2153-120X
ISSN Print: 2153-1196

Table of Contents

Volume 10 Number 11 October 2019

The figure on the front cover is from the article published in Journal of Modern Physics, 2019, Vol. 10, No. 11, pp. 1299-1309 by Yu. A. Khlestkov, *et al.*

Journal of Modern Physics (JMP)
Journal Information

SUBSCRIPTIONS

The *Journal of Modern Physics* (Online at Scientific Research Publishing, https://www.scirp.org/) is published monthly by Scientific Research Publishing, Inc., USA.

Subscription rates:
Print: $89 per issue.
To subscribe, please contact Journals Subscriptions Department, E-mail: sub@scirp.org

SERVICES

Advertisements
Advertisement Sales Department, E-mail: service@scirp.org

Reprints (minimum quantity 100 copies)
Reprints Co-ordinator, Scientific Research Publishing, Inc., USA.
E-mail: sub@scirp.org

COPYRIGHT

Copyright and reuse rights for the front matter of the journal:
Copyright © 2019 by Scientific Research Publishing Inc.
This work is licensed under the Creative Commons Attribution International License (CC BY).
http://creativecommons.org/licenses/by/4.0/

Copyright for individual papers of the journal:
Copyright © 2019 by author(s) and Scientific Research Publishing Inc.

Reuse rights for individual papers:
Note: At SCIRP authors can choose between CC BY and CC BY-NC. Please consult each paper for its reuse rights.

Disclaimer of liability
Statements and opinions expressed in the articles and communications are those of the individual contributors and not the statements and opinion of Scientific Research Publishing, Inc. We assume no responsibility or liability for any damage or injury to persons or property arising out of the use of any materials, instructions, methods or ideas contained herein. We expressly disclaim any implied warranties of merchantability or fitness for a particular purpose. If expert assistance is required, the services of a competent professional person should be sought.

PRODUCTION INFORMATION

For manuscripts that have been accepted for publication, please contact:
E-mail: jmp@scirp.org

Journal of Modern Physics, 2019, 10, 1299-1309
https://www.scirp.org/journal/jmp
ISSN Online: 2153-120X
ISSN Print: 2153-1196

Gravitational Description and Graphics of a Wormhole Structure—A Galactic Megamaximon

Yu. A. Khlestkov, N. Yu. Lukashina, M. Yu. Lukashin, P. Yu. Lukashin, N. S. Trushkin

National Research Nuclear University MEPhI, Moscow, Russia
Email: khlestkov@yandex.ru

How to cite this paper: Khlestkov, Yu.A., Lukashina, N.Yu., Lukashin, M.Yu., Lukashin, P.Yu. and Trushkin, N.S. (2019) Gravitational Description and Graphics of a Wormhole Structure—A Galactic Megamaximon. *Journal of Modern Physics*, **10**, 1299-1309.
https://doi.org/10.4236/jmp.2019.1011086

Received: September 10, 2019
Accepted: September 27, 2019
Published: September 30, 2019

Copyright © 2019 by author(s) and Scientific Research Publishing Inc.
This work is licensed under the Creative Commons Attribution International License (CC BY 4.0).
http://creativecommons.org/licenses/by/4.0/
Open Access

Abstract

Using the new exact solution of Einstein and Maxwell equations in the general relativity theory, they studied the internal structure of a geometric object with a nontrivial topology, the wormhole. They showed that the galactic black hole recently discovered by astronomers and astrophysicists as the part of the Event Horizon Telescope project with the radius about 10^{16} cm and the mass of about 10^{43} g can be a wormhole almost neutralized in charge with parameters close to critical—megamaximon, the radius of its neck curvature is equal to the so-called critical radius coinciding with half of the gravitational radius.

Keywords

Gravitation, Wormhole, Exact Solution, Megamaximon

1. Introduction

Gravitational interaction in cosmological scales (galaxies, universes) prevails. Great interest in this area is manifested in the study of objects with nontrivial properties—dark (exotic) matter, black holes, wormholes, etc. [1] [2]. This interest is increasing due to the recent discovery of such an object in deep space by astrophysicists (the Event Horizon Telescope project [3]).

This paper is devoted to the study of new exact particular solution of the Einstein and Maxwell equations use in the general relativity theory (GRT) [4] [5] [6] [7] to describe the internal structure and calculate the parameters of a compact stationary object—the wormhole within the scales of the galaxy and the universe. Previously, this method was applied to the microworld—to elementary particle and atomic nucleus lengths and showed good agreement with experimental results [7].

In this paper, we describe this solution, show the procedure of a wormhole occurrence analytically and graphically, and apply this model to study the possi-

ble nature of a galactic object experimentally discovered and described in [3].

2. Description of GRT Equations Particular Solution

Using galactic lengths, let's consider the simplest spherically symmetric system of the neutral dust (the matter without pressure and temperature with zero entropy) with the energy density ε_s, with the energy-momentum tensor $\overset{s}{\overbrace{T_{\mu\nu}}}$ depending on 4-dust velocity u_μ,

$$\overset{s}{\overbrace{T_{\mu\nu}}} = \varepsilon_s u_\mu u_\nu, \tag{1}$$

and from free electromagnetic field (without sources, *i.e.* with the electric charge density $\rho_f = 0$), described by the electromagnetic field tensor $F_{\mu\nu}$ and energy-momentum tensor $\overset{f}{\overbrace{T_\mu^\nu}}$:

$$\overset{f}{\overbrace{T_\mu^\nu}} = \frac{1}{4\pi}\left(F_\mu^\lambda F_\lambda^\nu + \frac{1}{4}\delta_\mu^\nu F_{\alpha\beta}F^{\alpha\beta}\right), \tag{2}$$

the interval square in which (metrics)

$$\mathrm{d}s^2 = g_{\mu\nu}\mathrm{d}x^\mu \mathrm{d}x^\nu \tag{3}$$

in spherical coordinates

$$x^\mu = \left\{x^0 = \tau; r; \theta; \varphi\right\} \tag{4}$$

has the following form [8]:

$$\mathrm{d}s^2 = \mathrm{e}^{\nu(\tau,r)}\mathrm{d}\tau^2 - \mathrm{e}^{\lambda(\tau,r)}\mathrm{d}r^2 - R^2(\tau,r)\left(\mathrm{d}\theta^2 + \sin^2\theta \mathrm{d}\varphi^2\right), \tag{5}$$

and described by Einstein's system of equations,

$$G_{\mu\nu} = \kappa T_{\mu\nu}, \quad \kappa = \frac{8\pi k}{c^4}, \tag{6}$$

where $G_{\mu\nu}$ is Einstein's geometric tensor,

$$T_{\mu\nu} = \overset{s}{\overbrace{T_{\mu\nu}}} + \overset{f}{\overbrace{T_{\mu\nu}}}, \tag{7}$$

and Maxwell's equations,

$$F_{;\nu}^{\mu\nu} = 0. \tag{8}$$

The system of Equations (1)-(8) in the associated with dust comoving frame of reference $u^\mu = \delta_0^\mu u^0$, where the energy-momentum tensor $T_{\mu\nu}$ of the internal space takes the following form:

$$T_\mu^\nu = diag\left(\varepsilon_s + \varepsilon_f; \varepsilon_f; -\varepsilon_f; -\varepsilon_f\right), \tag{9}$$

where ε_f is the energy density of the electromagnetic field, and it looks like this ($\dot{} = \frac{\partial}{\partial\tau}$, $' = \frac{\partial}{\partial r}$):

$$\varepsilon = \frac{4\pi R}{\kappa}\left(1 - \mathrm{e}^{-\lambda}R'^2 + e^{-\nu}\dot{R}^2\right), \tag{10}$$

$$\varepsilon^{\cdot} = 4\pi R^2 R^{\cdot} \varepsilon_f,\ \varepsilon' = 4\pi R^2 R' \left(\varepsilon_s + \varepsilon_f\right),$$

$$\varepsilon_f^{\cdot} = -4\frac{R^{\cdot}}{R}\varepsilon_f, \tag{11}$$

$$\varepsilon_f' = -4\frac{R'}{R}\varepsilon_f,\ \varepsilon_s^{\cdot} = -\frac{1}{2}\left(\lambda^{\cdot} + 4\frac{R^{\cdot}}{R}\right)\varepsilon_s.$$

After the integration of the Equations (10)-(11) for the case of a system that is periodic in time and limited in space without relativistic rotation, we obtain the following particular solution of it [7]:

$$\varepsilon = \varepsilon_g\left(r\right) - \frac{Q^2}{2R},$$

$$\mathrm{e}^{\nu} = \mathrm{e}^{\nu_\tau(\tau)},$$

$$\mathrm{e}^{\lambda} = \frac{R'^2}{f^2\left(r\right)}, \tag{12}$$

$$\varepsilon_f = \frac{R_c^2}{\kappa R^4},$$

$$\varepsilon_s = \frac{R_g'\left(r\right)}{\kappa R^2 R'},$$

$$f^2 < 1, \begin{cases} R = \dfrac{R_g}{2\left(1-f^2\right)}\left(1-\delta\left(r\right)\cos\eta\right), \\ \tau - \tau_r\left(r\right) = \dfrac{R_g}{2\left(1-f^2\right)^{\frac{3}{2}}}\left(\eta - \delta\left(r\right)\sin\eta\right). \end{cases} \tag{13}$$

Here $\varepsilon_g\left(r\right)$ is the total gravitational internal energy of the system on the radial coordinate r—an arbitrary function of r—the first integral of the system of differential Equations (10)-(11) of second order, Q is the second first integral of this system, in this case the constant arising from its integration is electric system charge (which, we recall, was absent during the problem formulation—we considered the free electric field without sources. This means that the gravitational system generated electrical charge Q, whose geometric image in curved space will be clarified below.

$\nu_\tau\left(\tau\right)$ is an arbitrary function of time associated with the arbitrariness in the method of time coordinate τ measurement. Let $\nu_\tau = 0$.

$f\left(r\right)$—the third first integral of the system—an arbitrary function of r, in this case, $f^2 < 1$.

R_c —the so-called critical radius of the system (10)-(11),

$$R_c = \frac{\sqrt{k}}{c^2}Q. \tag{14}$$

Gravitational radius proportional to the total gravitational mass of the system $M\left(r\right) = \varepsilon_g\left(r\right)/c^2$:

$$R_g = \frac{2kM\left(r\right)}{c^2}, \tag{15}$$

$\delta(r)$—the function of r, expressed through three independent first integrals of the Equations (10)-(11),

$$\delta = \sqrt{1-\frac{4R_c^2}{R_g^2}\left(1-f^2\right)}, \tag{16}$$

satisfying the following condition:

$$0 \le \delta(r) < 1. \tag{17}$$

So, this system makes from uncharged dust and free radial electric field

$$E_r = \sqrt{8\pi\varepsilon_f} = \frac{Q}{R^2} \tag{18}$$

(in the comoving frame of reference) an object—the electric charge Q. When $Q=0$, it passes into Tolman's well-known solution [8]—a system of dust-like neutral matter without an electromagnetic field. When $R_g = const$, it passes into the well-known static vacuum world of Reissner-Nordstrom [9] of a point charge Q with mass $M = const$.

Singularity is a characteristic feature of Tolman and Reissner-Nordstemm's worlds, special cases of this solution

$$R = 0, - \tag{19}$$

the point at which the curvature of space-time becomes infinite. This physically corresponds to the inversion of dust energy density (Tolman) or the energy density of the electromagnetic field (Reissner-Nordstrom) into infinity. The latter entails the most important feature—the Coulomb divergence of the point charge field.

This solution eliminates this singularity due to the formation of an object with a non-trivial topology—an unclosed wormhole.

3. Wormhole Internal Structure and Parameters

The appearance of a new wormhole in a curved space-time is due to inequality (17). Since $\delta(r)<1$, the solution (13) for $R(\tau,r)$—the radius of the 2-Gaussian curvature of the surface $\{\theta,\varphi\}$, at $R_g(r)>0$ shows that $R(\tau,r)$ does not vanish at any point:

$$R(\tau,r) > 0. \tag{20}$$

So, the electric field intensity (18) does not turn into infinity at any point.

$$E_r(\tau,r) \ne \infty. \tag{21}$$

Thus, the Coulomb divergence of the point charge field, which is present in all models within the special relativity theory (SRT), *i.e.* in flat Minkowski space, is eliminated.

Figure 1, Figure 2 show how the wormhole is formed. The family of coordinate surfaces (spheres = $R = const$ and cones $\theta = const$) in a flat space has the feature (singularity) $R=0$. If $R(\tau,r)\ne 0$, then the family of cones turns into the family of surfaces of hyperbolic type with negative Gaussian curvature,

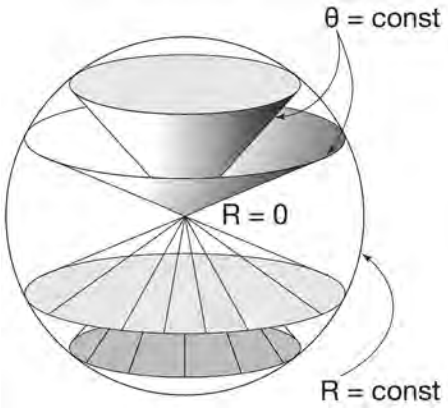

Figure 1. The family of coordinate surfaces $R = const$ and $\theta = const$ in the empty flat space of SRT.

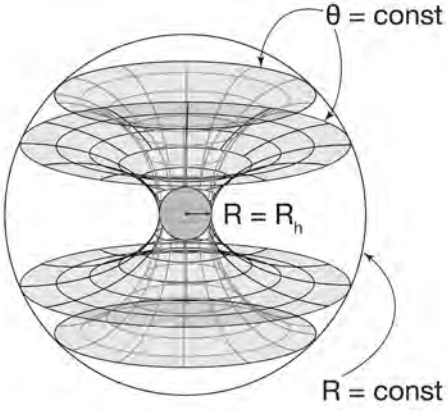

Figure 2. The family of coordinate surfaces $R = const$ and $\theta = const$ in the curve space of GRT in the world with a constant charge $Q = const$. The neck radius makes R_h.

similar to one-cavity hyperboloid, whose main radii lie on opposite sides of these 2-surfaces, that is, they have different signs (Figure 2). This is a wormhole with a neck (horn, throat)—the sphere of an extreme radius $R_h = const$.

According to the solution (13), this wormhole has extreme static surfaces—the necks with a constant radius of 2-Gaussian curvature R_h, determined from the following condition:

$$r = r_h,\ R_h^{\bullet} = 0, \tag{22}$$

which is always equal to doubled classical radius R_f if we substitute the conditions (22) into the hole Equation (13):

$$R_f(r) = \frac{Q^2}{2Mc^2} = \frac{R_c^2}{R_g}, \tag{23}$$

$$R_h = 2R_{fh} = \xi R_c = \frac{R_{gh}}{2}\xi^2,$$

where ξ is the ratio of the electric charge Q to the gravitational "charge"

$\sqrt{k}M_h$ at the neck :

$$\xi = \frac{Q}{M_h\sqrt{k}}. \tag{24}$$

We will solve the Cauchy problem with the initial conditions. Let the radius of curvature $R(0,r) = R(0)$ will be a periodic function of the radial coordinate r at $\tau = 0$ ($\eta = \pi$):

$$R(0) = \frac{R_{\max}}{2} + \frac{R_h}{2} - \frac{R_{\max} - R_h}{2}\cos 2\chi, \tag{25}$$

where $\chi = \pi\dfrac{r}{r_h}$, $R_{\max}$ is the radius R at $\chi = \dfrac{\pi}{2}$ in the state of maximum expansion of the wormhole's internal space. Let us set the initial change rate of this radius, for example:

$$R^{\cdot}(0,r) = R^{\cdot}(0) = 0, \tag{26}$$

and let the dust energy density is homogeneous in the initial state for simplicity:

$$\varepsilon_s(0) = \varepsilon_{sh} = const, \tag{27}$$

where ε_{sh} is the dust energy density on the wormhole neck.

The initial data (25)-(27) allows to express all functions of r and constants through the dimensionless parameter $\xi = \dfrac{R_h}{R_c} = \dfrac{Q}{\sqrt{k}M_h}$, the critical radius R_c and $R(0)$:

$$\begin{gathered}
R_g = R_{gh}\left(\frac{R(0)}{R_h}\right)^3,\\
R_{gh} = \frac{2R_c}{\xi},\\
\varepsilon_{sh} = \frac{6}{\kappa R_c^2}\frac{1}{\xi^4},\\
1 - f^2 = \frac{R_g}{R(0)} - \frac{R_c^2}{R^2(0)},\\
1 - f_h^2 = \frac{1}{\xi^2},\\
\delta = 1 - \frac{2R_c^2}{R_g R(0)},\\
\delta_h = 0,\\
R_{\max} = \frac{1}{2}R_c\xi^2\sqrt{1+\sqrt{1+\frac{8}{\xi^4}}},\\
R_{\min} = 2R_c\frac{1}{\xi^2}\frac{1}{\sqrt{1+\sqrt{1+\frac{8}{\xi^4}}}},\\
R_{\max}R_{\min} = R_c^2.
\end{gathered} \tag{28}$$

A geometric object whose $\xi = 1$, that is, the electric charge Q is equal to the gravitational $\sqrt{k}M_h$ is called a maximon. It has extreme parameters:

$$R_h = R_c = 2R_{fh} = \frac{R_{gh}}{2}, \quad R_{\max} = R_{\min} = R_c, \tag{29}$$

$$\varepsilon_s(0) = \varepsilon_{sc} = \frac{6}{\kappa R_c^2}.$$

Thus, this simplest solution of the GTR equations describes the world that is periodic in time and space, formed by a free radial electric field and a neutral dust-like substance, which is a pulsating unclosed wormhole geometrically, which is an electric charge Q itself generated by a curved space changing its sign through the spatial period $r_h\left(\chi \in [0,\pi]\right)$, like the electric field E_r (**Figure 3**).

This tunnel ("well") can be cut off over a period along r and glued to the vacuum static world of Reissner-Nordstrom [9] through two static necks—an external solution for the field of the point charge Q of mass M_h —asymptotically flat in vacuum at infinity (**Figure 4**).

4. Universality of Gravitational Interaction

Traditionally, the gravitational interaction is considered to be vanishingly small as compared to both electromagnetic and nuclear one in the microworld, but it prevails in the megaworld, at the lengths of galaxies and universes. However, this is not quite true. Gravitational interaction is universal. The first argument is in plain sight. The internal structure of the proton was detected experimentally: its charge radius, as measured by the Lamb shift on muon hydrogen, turned out to be equal to 0.8409×10^{-13} cm [10]. This is already enough to consider space-time as curved, *i.e.* formed by a gravitational field.

The logic is simple. If it were flat (with the Riemann-Christoffel curvature tensor identically equal to zero), then it would be necessary to be empty, according to the Einstein equations, $G_{\mu\nu} = \kappa T_{\mu\nu}$: if $G_{\mu\nu} \equiv 0$, then the matter energy-momentum tensor is identically zero, $T_{\mu\nu} \equiv 0$. So the space would be empty. This also means that if there can be material objects in it, then they must be the point features of the field that do not belong to Riemannian space itself, including proton, and any other particles. And this is contrary to the experiment. Therefore, the solution of the Einstein and Maxwell equations given in this paper is applicable at any lengths.

This conclusion confirms the Einstein equations in General relativity: they do not contain a fundamental constant of dimension of length (of the two constants c and k it is impossible to construct such a value).

So, being applied to a proton, it gives the value of its neck radius R_h, equal to 0.8412×10^{-13} cm [7]. This coincides with its experimental value 0.8409×10^{-13} cm [7] within the accuracy of 0.04%.

Thus, for the first time, we obtain reliable experimental confirmation of GRT in the relativistic region of the microworld, in which the influence of space-time curvature, *i.e.* gravitational field, was considered negligible.

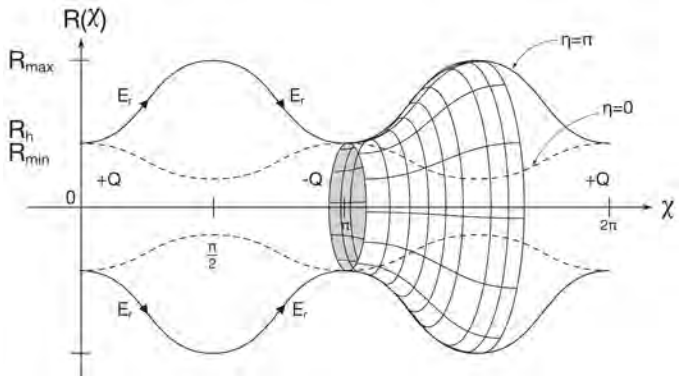

Figure 3. The internal space of the electric charge Q (wormhole)—the tunnel that does not close in time and in space in the state of maximum ($\eta=\pi$) expansion and maximum compression ($\eta=0$). The cyclic coordinate φ is directed orthogonally to the plane of the figure. The cyclic coordinate θ is not shown.

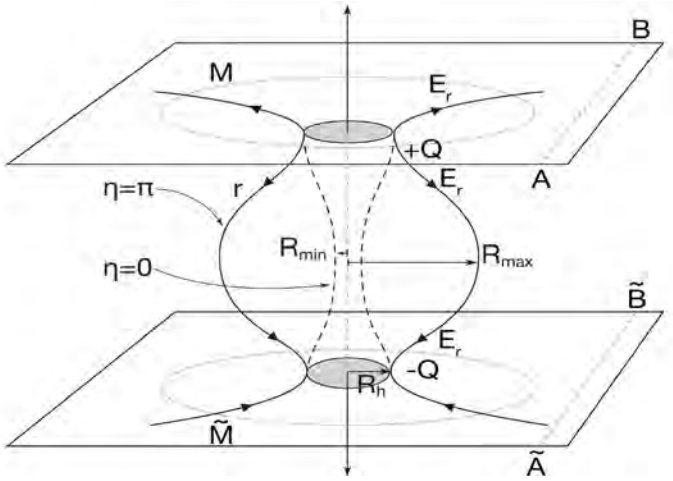

Figure 4. A wormhole pulsating from the state of maximum expansion ($\eta=\pi$) to the state of maximum compression ($\eta=0$), cut off and glued on the necks within the period with two parallel asymptotically flat worlds—M and $\tilde{M}$, a geometric image of an electric charge Q—pair particle—antiparticle. The coordinate r is directed by arrows, the cyclic coordinate φ is orthogonal to the picture, the cyclic coordinate θ is not shown. If you cut the worlds M and $\tilde{M}$ along dashed lines AB and $\widetilde{AB}$ and glue them together, you will get one space with two holes (Wheeler's handle).

5. Galactic Megamaximon

In this paper, we apply the solution of GRT Equations (10)-(11) to the megaworld: let's show that an object found in the constellation Virgo with the radius R_h of about 10^{16} cm and the solar mass of about 6.5×10^9 mass of the Sun that was discovered by astrophysicists and astronomers within the Event Horizon Telescope project can be an extreme wormhole—megamaximon (*i.e.* it has $\xi=1$).

According to (23), the radius of the wormhole neck curvature makes.

$$R_h = 2R_{fh} = \frac{Q^2}{M_h c^2}.$$

Let express the electric charge Q through the fundamental charge e and the number of such uncompensated charges on the neck N_Q:

$$Q = eN_Q = eN_p\left(1-\eta_e\right), \tag{30}$$

where N_p is the number of protons in the nuclei of atoms, $\eta_e = \left|1-\frac{N_e}{N_p}\right|$ is the charge neutralization factor, N_e is the number of electrons in the neck atoms.

The mass of the neck is estimated by the number of nucleons in the nuclei:

$$M_h = m_p N_p\left(1+\eta_n\right), \tag{31}$$

where $\eta_n = \frac{N_n}{N_p}$ is the neutronization coefficient of nuclei.

Substituting (30) and (31) in (23), we obtain the following for the hole radius:

$$R_h = \frac{e^2}{m_p c^2} N_p \cdot \frac{\left(1-\eta_e\right)^2}{\left(1+\eta_n\right)}. \tag{32}$$

From the calculation of the proton parameters as a wormhole [7] it follows that

$$\frac{e^2}{m_p c^2} = \frac{r_{hp*}}{\gamma_{*p}}, \tag{33},$$

where r_{hp*} is the radius of the proton neck, taking into account the spin, γ_{*p} is the Lorentz factor of the proton on its neck.

Substituting (33) in (32), we get the following:

$$R_h = \frac{r_{hp*}}{\gamma_{*p}} N_p \frac{\left(1-\eta_e\right)^2}{\left(1+\eta_n\right)}. \tag{34}$$

from this, having entered the mass of the mega-wormhole neck M_h from (31), we have for the coefficient of neutralization the following:

$$\left|1-\eta_e\right| = \sqrt{\frac{R_h \gamma_{*p}}{r_{hp*}} \frac{m_p\left(1+\eta_n\right)^2}{M_h}}. \tag{35}$$

Substituting the numerical values of the its quantities in (35):

$m_p = 1.6726\times10^{-24}$ g,

$r_{h*p} = 0.8412\times10^{-13}$ cm,

$R_h = 10^{16}$ cm,

$M_h = 5.6\times10^9 \times 1.9885\times10^{33}$ g,

$\gamma_{*p} = 0.548\times10^3$,

$\eta_n \approx 1$,

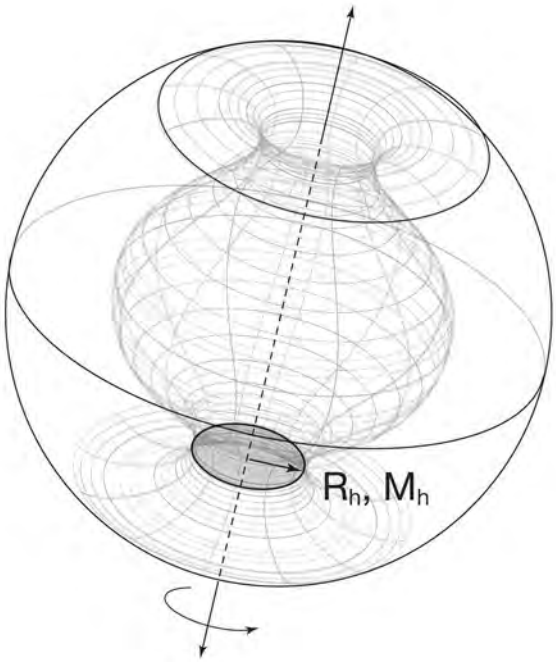

Figure 5. "Wandering" galactic wormhole with extreme radius R_h and the neck mass M_h (megamaximon).

we obtain the following:

$$\left|1-\eta_e\right| \approx 0.63\times 10^{-17} \ll 1. \tag{36}$$

This means that this wormhole is almost neutralized by charge: $\eta_e \to 1$.

Let's estimate the value of the dimensionless parameter ξ:

$$\xi = \frac{R_h}{R_c},\ R_c = \frac{Q\sqrt{k}}{c^2} = \frac{e\sqrt{k}}{c^2} N_p \left|1-\eta_e\right|,\ \xi = \frac{r_{hp*}\left|1-\eta_e\right|}{\gamma_{*p}\left(1+\eta_n\right) r_c}. \tag{37}$$

$r_c = 1.3807\times 10^{-34}$ cm [7].

Substituting the values of the parameters in (37), we obtain the following for ξ:

$$\xi = \frac{0.8412\times 10^{-13}\times 0.3\times 10^{-17}}{1.3807\times 10^{-34}\times 2\times 0.548\times 10^{3}} \approx 3.5 \to 1. \tag{38}$$

Thus, the object discovered by astronomers and astrophysicists in the galaxy is the wormhole, the practical maximum wormhole by parameters, the megamaximon.

Considering that it is geometrically similar to a torus on the photo, it can be assumed that this is the wormhole wandering between galaxies, obtained from the solution (13) by gluing through two necks with two Reissner-Nordstrom vacuum worlds, which are cut and glued along the circles of radius, much larger radius of the neck (**Figure 5**).

6. Summary

The paper describes the solution of general relativity equations for spherically

symmetric dust-like matter and the radial electric field and shows analytically and graphically that it describes a space object of nontrivial topology—the wormhole, with its two necks extending into two parallel vacuum asymptotically flat worlds or into one world if these surfaces are cut and glued accordingly.

This model is used to describe the newly discovered galactic black hole (presumably) with a radius of about 10^{16} cm and a mass of 10^{43} g by astrophysicists and astronomers in Virgo constellation within the Event Horizon Telescope project. It is shown that it can be a hole (do not confuse it with a Black Hole) in space-time—the wormhole that is almost compensated by electric charge with the radius equal to the critical R_c, and equal to half of the gravitational radius R_g. That is, this object is megamaximon.

Acknowledgements

We express our gratitude to S.I. Okov for his help in translating the article.

Conflicts of Interest

The authors declare no conflicts of interest regarding the publication of this paper.

References

[1] Visser, M. (1996) Lorentzian Wormholes. Springer Verlag, Berlin.

[2] Bronnikov, K.A., Fabris, J.C. and Rodrigues, D.C. (2015) *International Journal of Modern Physics D*, **25**, Article ID: 1641005. https://doi.org/10.1142/S0218271816410054

[3] Akiyama, K., Alberdi, A, Alef, W., Asada, K., Azulay, R., Baczko, A.-K., Ball, D. and Volokovic, M. (2019) *The Astrophysical Journal Letters*, **875**, L4.

[4] Khlestkov, Yu.A. (2005) *Journal of Experimental and Theoretical Physics*, **101**, 259. https://doi.org/10.1134/1.2047791

[5] Khlestkov, Y.A. and Sukhanova, L.A. (2016) *Foundation Physics*, **46**, 668-688. https://doi.org/10.1007/s10701-016-9998-6

[6] Khlestkov, Yu.A. and Sukhanova, L.A. (2017) *Chinese Journal of Physics*, **55**, 1794-1807. https://doi.org/10.1016/j.cjph.2017.08.007

[7] Khlestkov, A.Yu. and Khlestkov, Yu.A. (2019) *Russian Physics Journal*, **62**, 264-283. https://doi.org/10.1007/s11182-019-01709-9

[8] Landau, L.D. and Lifshitz, E.M. (1975) The Course of Theoretical Physics. Vol. 2. The Classical Theory of Fields. Butterworth-Heinemann, London.

[9] Hawking, S.W. and Ellis, G.F.R. (1975) The Large Scale Structure of Space-Time. Cambridge University Press, Cambridge.

[10] Pole, R., *et al.* (2010) *Nature*, **466**, 213.

Journal of Modern Physics, 2019, 10, 1310-1341
https://www.scirp.org/journal/jmp
ISSN Online: 2153-120X
ISSN Print: 2153-1196

Split Membrane 11D Spacetime = 1D Eleventh Dimension Interval Space + 6D Rishon Space + 3D Higgs Space + 1D Einstein Time: Cosmology

Ding-Yu Chung

Utica, Michigan, USA
Email: dy_chung@yahoo.com

How to cite this paper: Chung, D.-Y. (2019) Split Membrane 11D Spacetime = 1D Eleventh Dimension Interval Space + 6D Rishon Space + 3D Higgs Space + 1D Einstein Time: Cosmology. *Journal of Modern Physics*, **10**, 1310-1341.
https://doi.org/10.4236/jmp.2019.1011087

Received: August 30, 2019
Accepted: October 9, 2019
Published: October 12, 2019

Copyright © 2019 by author(s) and Scientific Research Publishing Inc.
This work is licensed under the Creative Commons Attribution International License (CC BY 4.0).
http://creativecommons.org/licenses/by/4.0/
Open Access

Abstract

The paper posits that the cyclic universe cosmology involves the split of the membrane 11D (11 dimensional) spacetime into the 1D eleventh dimension orbifold interval space to form gravity, the 6D discrete interior rishon space (TTT-VVV for positron-neutrino or TTV-TVV for u-$\bar{d}$ quarks) to form the Standard Model, the 3D Higgs space (attachment space to attach matter or detachment space to detach matter) to form the Higgs or reverse Higgs field, and 1D Einstein time to be shared by all spaces. To establish particle masses, spacetime dimension number decreases with decreasing speed of light, decreasing vacuum energy, and increasing rest mass. The 4D and the 10D have zero and the highest vacuum energies, respectively. The cyclic universe cosmology starts with the zero-energy 4D inter-universal void and the positive-energy membrane and negative-energy antimembrane 11D dual universe which is split into four equal 10D string branes, including the 10D positive-energy weak-gravity brane with matter, negative-energy strong-gravity brane, negative-energy weak-gravity brane with antimatter, and positive-energy strong-gravity brane in the 11D bulk with the 1D eleventh dimension interval space in between the strong and the weak-gravity branes. To form the home universe where we inhabit, the 10D positive-energy weak-gravity brane with attachment space absorbed the zero-energy 4D inter-universal void with detachment space, resulting in the combination of rest mass from attachment space and kinetic energy from detachment space, the formation of the 4D spacetime universe by transforming 6D connected exterior space into 6D discrete interior rishon space, and cosmic inflation. The other three branes did not absorb the inter-universal void, resulting in the oscillating dimension branes between 10D and 4D stepwise without kinetic energy. The three branes are hidden when D > 4, and they are dark energy when D = 4. The split 11D spacetime and cosmology provide the mat-

ter-antimatter imbalance and the accurately calculated masses for leptons, quarks, hadrons, gauge bosons, the Higgs boson, gravity, dark matter, and dark energy.

Keywords

String Theory, Rishon, Cyclic Universe Cosmology, Dark Energy, Dark Matter, Particle Masses

1. Introduction

String theory proposes to produce a theory of everything that describes all known particles and forces [1]. String theory with the inclusion of the 11th dimension is called M-theory. The extra dimensions of 11D (11 dimensional) M-theory or 10D string theory are the compact manifolds with sizes about the order of the Planck length, 10^{-33} cm, such that they remain hidden to the experiment, explaining why we see only four dimensions. The compactification of the extra space dimensions specifies a shape for the extra space dimensions. Different shapes correspond to different possible universes. The number of the shapes is typically estimated to be around 10^{500}, which can accommodate almost any phenomena [2].

To avoid the problem of 10^{500} universes due to the compactification, an alternative to the compactification is the Randall-Sundrum model for five dimensional spacetime [3]. In the RS1 (Randall-Sundrum model 1) of the Randall-Sundrum model [4] [5], the fifth dimension as the extra space dimension is an orbifold interval space between the Planckbrane (strong-gravity brane) and the Tevbrane (weak-gravity brane) in the warped five dimensional bulk. In this warped spacetime which is only warped along the fifth dimension, the gravity is extremely high at the strong-gravity brane, but it drops exponentially as it moves closer towards the weak-gravity brane. Gravity on the weak-gravity brane is much weaker than on the strong-gravity brane. The weak-gravity brane contains matter as the Standard Model particles, while the strong-gravity brane is dominated by gravity. The Randall-Sundrum model explains the hierarchy problem between the weak-gravity and the strong electromagnetic force and the other fundamental forces. Using the Randall-Sundrum model, this paper posits that the 1D eleventh dimension interval space was the space between the two string branes (the weak-gravity string brane and the strong-gravity string brane) in the warped 11D membrane bulk. The two string 10-branes are the progenitors of the home universe where we inhabit and dark energy. The comparison between the RS1-5D spacetime and the RS1-11D spacetime is as **Figure 1**.

The Standard Model of particle physics consists of 17 elementary particles including 6 leptons (electron, muon, and tau, electron neutrino, muon neutrino, tau neutrino), 6 quarks (down, up, strange, charm, bottom, and top), 4 gauge bosons (photon, W boson, Z boson, and gluon), and the Higgs boson. The 4

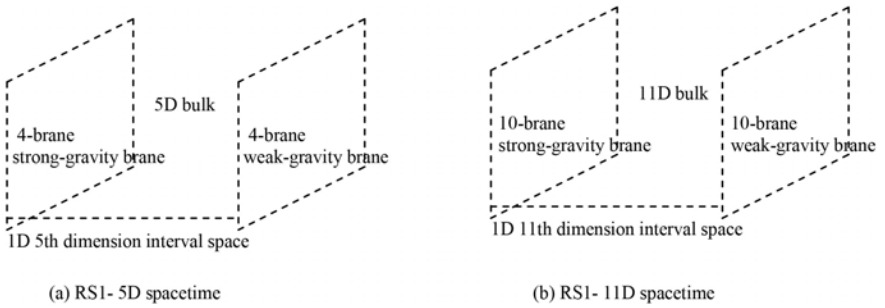

Figure 1. (a) RS1-5D spacetime: the 5D bulk with the two 4-branes (the weak-gravity brane and the strong-gravity brane) and 1D 5th dimension interval space. (b) RS1-11D spacetime: the 11D bulk with the two 10-branes (the weak-gravity brane and the strong-gravity brane) and 1D 11th dimension interval space.

gauge bosons have the gauge symmetry U(1) X SU(3) X $SU(2)_L$. The Standard Model explains very well the relations among the 17 elementary particles, but the Standard Model cannot explain the masses of 17 elementary particles, the origins of the 17 elementary particles and the gauge symmetry, neutrino oscillation, the apparent matter-antimatter imbalance in the universe, gravity, dark matter, and dark energy.

To explain the origin of leptons and quarks in the Standard Model, preon models propose simple substructure particles in leptons and quarks [6] [7]. One of the preon models is the Rishon Model by Haim Harari [8] and Michael A. Shupe [9]. The two fundamental substructure particles are rishons consisting of T with 1/3 charge and ½ spin and neutral V with ½ spin. TTT is positron, while VVV is electron neutrino. TTV, TVT and VTT are the three colors of up quark, while TVV, VTV and VVT are the three colors of down quark. Hypercolor is required to confine rishons in leptons and quarks [10]. The Rishon Model provides the origin of the first generation fermions in the Standard Model, but there is no experimental evidence for the existence of rishons as the substructure particles Quarks and leptons have been found to be point-like particles without substructure particles [11].

To avoid the difficulty of substructure particles of the Rishon model, Sundance Bilson-Thompson proposes the Helon Model with the discrete topological properties of discrete trivalent twisted strand braids [12] [13]. Each rishon is a helon (H_+, H_-, or H_0) which is a twisted strand, and three twisted strands form a braid in the Helon Model. H_+ H_+ H_+, H_0 H_0 H_0, H_+ H_+ H_0, and $H_+H_0H_0$ correspond to TTT, VVV, TTV, and TVV, respectively.

This paper proposes the Rishon Space Model where rishon is space instead of substructure particle. The Rishon Space Model is derived from the transformation from 10D string spacetime into 4D observed spacetime by converting the 6D connected space into the 6D discrete rishon space in the form of the two sets of three (trivalent) discrete one-dimensional strands as in the Helon Model. The 6D discrete rishon space consists of TTT-VVV or TTV-TVV space for the space of positron-neutrino or u-$\bar{d}$ quarks, respectively. The two sets of the trivalent

dimensional space in the 6D rishon space have the symmetry of isospin between TTT and VVV and between TTV and TVV. TTT represents one integer charge, VVV is neutral, and TTV and TVV represent fractional charges [14]. The reason for the confined trivalent rishon space is to match the confined trivalent 3D connected space in the observed 4D spacetime, so the trivalent discrete rishon space becomes the interior space to determine the properties (flavor, charge, isospin, and color) of leptons and quarks, while the trivalent connected space becomes the exterior space to determines the momenta and positions of leptons and quarks.

The transformation from 10D string spacetime into 4D observed by converting the 6D connected space into the 6D Rishon Space with TTTVVV or TTVTVV is the continuation of the RS1-11D spacetime where the 10D weak-gravity brane is converted into the 4D home universe where we inhibit with the 6D rishon space as **Figure 2**.

In conventional Higgs mechanism, the Higgs field is the place where a massless particle gains mass through spontaneous symmetry breaking. The scalar Higgs Field exists permanently in the universe. The problem with such permanent Higgs field is the cosmological constant problem from the huge gravitational effect by the Higgs field in contrast to the observation [15]. To avoid the cosmological problem, the previous paper [16] posits that the Higgs field is transitional, and appears only during spontaneous symmetry breaking. The Higgs field disappears after spontaneous symmetry breaking. The permanent space precursor of the Higgs field is attachment space that attaches matter to space, and relates to rest mass. The permanent space precursor of the transitional reverse Higgs field is 3D detachment space which detaches matter from space, and relates to kinetic energy. Attachment space and detachment space are the Higgs space which interacts with matter. Because the Higgs field and the reverse Higgs field are transitional, the cosmological constant problem disappears. The mixed Higgs spaces as the combinations of n units of attachment space (denoted as 1) and n units of detachment space (denoted as 0) consist of binary partition space, (1)n(0)n, as the space of wave-particle duality, binary miscible space, (1+0)n, as the space of relativity, and binary lattice space, (1 0)n, as the space of virtual gauge rishon boson in quantum field theory. The Higgs space is the interior space to determine the properties (attachment and detachment to matter) of

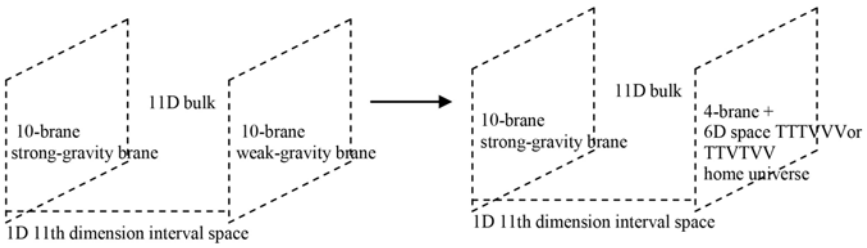

Figure 2. The transformation from the 10D weak-gravity brane to the home universe with 4D spacetime + 6D space (TTTVVV or TTVTVV).

elementary particles, while the exterior space determines the momenta and positions of elementary particles. A particle with the discrete interior rishon space moves with the different bound Higgs spaces under different conditions.

As shown later, detachment space is originally from the inter-universal void in the multiverse. To form the home universe where we inhabit, the 10D weak-gravity brane with attachment space absorbed the zero-energy 4D inter-universal void with detachment space, resulting in the combination of rest mass from attachment space and kinetic energy from detachment space and the formation of the 4D spacetime universe by transforming 6D connected exterior space into 6D discrete interior rishon space as **Figure 3**.

According to Johan Hansson, one of the ten biggest unsolved problems (quantum gravity, particle masses, the "measurement" problem, turbulence, dark energy, dark matter, complexity, the matter-antimatter asymmetry, friction, and the "arrow of time") in physics [17] is the incalculable particle masses of leptons, quarks, gauge bosons, and the Higgs boson. The Standard Model of particle physics contains the particles masses of leptons, quarks, and gauge bosons which cannot be calculated or predicted theoretically. From a theoretical point of view the particle mass is a total unsolved problem—they might as well have been random numbers drawn from a hat. The repetition of leptons and quarks with increasing masses has also remained an unsolved problem. Max Jammer [18] concluded that nobody knows what particle masses really are. The mass parameters experimentally measured for elementary particles have no theoretical explanation whatsoever. From the vantage point of theory the masses could just as well be a set of randomly generated numbers.

In this paper, the masses of elementary particles are calculated accurately by dimension numbers. As discussed in the previous papers [19] [20], between 4D spacetime and 10D spacetime, dimension number decreases with decreasing speed of light, decreasing vacuum energy, and increasing rest mass. The 4D and the 10D have zero and the highest vacuum energies, respectively. Each spacetime dimension D associates with mass dimension d where D + d = 14 initially. All elementary particles for baryonic matter (leptons, quarks, gauge bosons, gravity, the Higgs boson, and cosmic rays) and dark matter (sterile neutrinos) can be placed in the periodic table of elementary particles based on the two sets of the seven mass dimensions [21] [22]. The periodic table of elementary particles

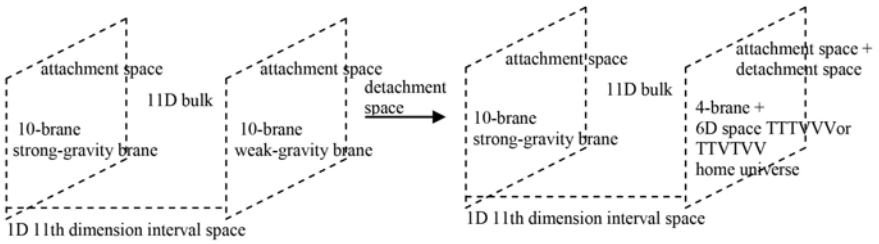

Figure 3. The addition of detachment space from the zero-energy 4D inter-universal void to the 10D weak-gravity brane to form the home universe with both attachment space and detachment space.

provide the accurate calculated masses for leptons, quarks, hadrons, gauge bosons, the Higgs boson, gravity, dark matter, and dark energy.

This paper posits that the origin of the split is from the cyclic universe cosmology in the multiverse. As mentioned in the previous papers [19] [20], the multiverse consists of the zero-energy inter-universal void with 4D detachment space and the multiple 11D positive-energy membrane-antimembrane and negative-energy anti-membrane dual universes with 11D attachment space. The total energy of a dual 11D universe is zero. Detachment space in the inter-universal void prevents the collision of the 11D dual universes, while attachment space in a dual universe allows the existence of mass-energy in the space of the dual universe.

The cyclic universe cosmology starts with the zero-energy inter-universal void and the positive-energy membrane and negative-energy antimembrane 11D dual universe which is split into four equal 10D string branes, including the 10D positive-energy weak-gravity brane with matter, negative-energy strong-gravity brane, negative-energy weak-gravity brane with antimatter, and positive-energy strong-gravity brane in the 11D bulk. The 1D eleventh dimension interval space is between the strong and the weak-gravity branes as in Randall-Sundrum model. To form the home universe where we inhabit, the positive-energy weak-gravity brane with attachment space absorbed the zero-energy 4D inter-universal void with detachment space, resulting in the combination of rest mass from attachment space and kinetic energy from detachment space and the formation of the 4D spacetime universe by transforming 6D connected exterior space into the 6D discrete interior rishon space. The result was cosmic inflation from high vacuum energy (10D) to zero vacuum energy (4D). The other three branes did not absorb the inter-universal void, resulting in the oscillating dimension branes between 10D and 4D stepwise without kinetic energy. The three branes are hidden when $D > 4$, and they are dark energy when $D = 4$. Afterward, when $D > 4$ for the three branes, the home universe and the three branes start to contract, and eventually return to the original four 10D string branes and then to the original 11D membrane-antimembrane dual universe for the cyclic universe cosmology. Different spacetimes are shown in **Table 1**.

Section 2 deals with the rishon space. Section 3 describes the Higgs space. Section 4 explains the spilt membrane 11D spacetime based on the cyclic universe cosmology in the multiverse. The 11D split spacetime and cosmology provides the matter-antimatter imbalance and the accurate calculated masses for all elementary baryonic matter particles, dark matter, and dark energy.

2. The Rishon Space

The paper posits that the membrane 11D spacetime is split into the 1D eleventh dimension orbifold interval space, the 6D discrete topological rishon space, the 3D bound Higgs space, and the 1D Einstein time. The 6D discrete topological rishon space is derived from the Rishon Model by Haim Harari [8] and Michael A. Shupe [9] which explains the origin of leptons and quarks in the Standard

Table 1. Spacetimes.

spacetime	origin	topology	relate to
11D spacetime	original 11D membrane universe	large and connected	attachment space for rest mass
4D spacetime	original 4D inter-universal void	large and connected	detachment space for kinetic energy
10D spacetime	original 10D string brane	large and connected	attachment space for rest mass
oscillating D spacetime	the three oscillating branes between 10D and 4D	large and connected	dark energy when D = 4
1D 11th dimension interval space	interval space between the two string branes in 11D membrane bulk	orbifold interval space	gravity
6D rishon space	transformation from 10D spacetime to 4D spacetime by transforming 6D connected exterior space into 6D discrete interior rishon space	discrete trivalent twisted strand braids	space (TTT-VVV or TTV-TVV) of positron-neutrino or up-down quarks
3D Higgs space	the absorption of 4D inter-universal void by the 10D string brane	bound to all spaces	the space precursors of the transitional Higgs field and reverse Higgs field
1D Einstein time	11 D spacetime and 4D spacetime	bound to all spaces	all split spaces share the same time

Model. The Rishon Model proposes that the two fundamental substructure particles are rishons consisting of T with 1/3 charge and ½ spin and neutral V with ½ spin. TTT is positron, while VVV is electron neutrino. TTV, TVT and VTT are the three colors of up quark, while TVV, VTV and VVT are the three colors of down quark. The Rishon Model provides the origin of the first generation fermions in the Standard Model, but there is no experimental evidence for the existence of rishons as the substructure particles. Quarks and leptons have been found to be point-like particles without substructure particles [11].

To avoid the difficulty of substructure particles, Sundance Bilson-Thompson proposes the Helon Model with the discrete topological properties of discrete trivalent twisted strand braids [12] [13]. Each rishon is a helon which is a twisted strand as H_+, H_-, or H_0 as shown in **Figure 4**. In the helon model, helons are topological in nature, and helons are not considered as substructure particles. The integral twists of strands represent the quantized electric charges of particles. Three twisted strands form a braid in the Helon Model. H_+ H_+ H_+, H_0 H_0 H_0, H_+ H_+ H_0, and $H_+H_0H_0$ as the trivalent twisted strand braids represent positron, neutrino, up quark, and down quark, respectively. The permutations of twists on certain braids naturally account for the color charges of quarks and gluons.

This paper proposes the Rishon Space Model where rishon is space instead of substructure particle. The Rishon Space Model is derived from the transformation from 10D string spacetime into 4D observed spacetime by converting the 6D connected space into the 6D discrete rishon space in the form of the two sets of three (trivalent) discrete one-dimensional strands as in the Helon Model. The 6D discrete rishon space consists of TTT-VVV or TTV-TVV space for the space of positron-neutrino or u-$\bar{d}$ quarks, respectively. The two sets of the trivalent dimensional space in the 6D rishon space have the symmetry of isospin between TTT and VVV and between TTV and TVV. TTT represents one integer charge, VVV is neutral, and TTV and TVV represent fractional charges. The reason for the confined trivalent rishon space is to match the confined trivalent 3D

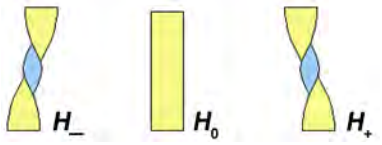

Figure 4. Twist helons.

connected space in the observed 4D spacetime, so the trivalent discrete rishon space becomes the interior space to determine the properties (flavor, charge, isospin, and color) of leptons and quarks, while the trivalent connected space becomes the exterior space to determines the momenta and positions of leptons and quarks. The transformation from the 6D connected exterior space into 6D discrete interior rishon space is as follows.

$$\begin{aligned}&\text{9D connected exterior space in 10D connected exterior spacetime for string}\\&\xrightarrow{\text{from 10D to 4D}}\text{6D discrete interior rishon space}\left(\text{TTTVVV}\right)\text{ for e-}\nu\text{ in 4D}\\&\text{connected exterior spacetime or 6D discrete interior rishon space}\left(\text{TTVTVV}\right)\quad(1)\\&\text{for u-}\bar{\text{d}}\text{ in 4D connected exterior spacetime}\longrightarrow\text{TTT for e and VVV for }\nu\\&\text{or TTV for u and TVV for }\bar{\text{d}}\text{ in 4D connected exterior spacetime}\end{aligned}$$

The rishon space and helon are shown in Table 2 and Figure 5. The interactions among leptons and quarks are through the 4 gauge bosons (photon, W boson, Z boson, and gluon). The 4 gauge bosons have the gauge symmetry U(1) X $SU(3)_c$ X $SU(2)_L$.

3. The Higgs Space

The 3D Higgs space consists of attachment space as the space precursor of the transitional Higgs field and detachment space as the space precursor of the transitional reverse Higgs field. Attachment space that attaches matter to the space relates to rest mass, detachment space that detaches matter from the space relates to kinetic energy. The Higgs space involves the Higgs mechanism for the transformation between massless particle and massive particle and the space structures from the combination of attachment space and detachment space. The Higgs space is the interior space to determine the properties (attachment and detachment to matter) of elementary particles, while the exterior space determines the momenta and positions of elementary particles.

3.1. The Higgs Mechanism

In conventional physics, space does not couple with particles, and is the passive zero-energy ground state space. Under spontaneous symmetry breaking in conventional physics, the passive zero-energy ground state is converted into the active, permanent, and ubiquitous nonzero-energy Higgs field, which couples with massless particle to produce the transitional Higgs field-particle composite. Under spontaneous symmetry restoring, the transitional Higgs field-particle composite is converted into the massive particle with the longitudinal component on zero-energy ground state without the Higgs field as follows.

Table 2. The rishon space and helon.

particles	rishon space	helon
positron	TTT	$H_+ H_+ H_+$
electron	$\bar{T}\bar{T}\bar{T}$	$H_- H_- H_-$
neutrino	VVV	$H_0 H_0 H_0$
u quark	TTV, TVT, VTT	$H_+ H_+ H_0$. $H_+ H_0 H_+$, $H_0 H_+ H_+$,
$\bar{d}$ quark	TVV, VTV. VTT	$H_+ H_0 H_0$, $H_0 H_+ H_0 H_0$, $H_0 H_0 H_+$
$\bar{u}$ quark	$\bar{T}\bar{T}\bar{V}$, $\bar{T}\bar{V}\bar{T}$, $\bar{V}\bar{T}\bar{T}$	$H_- H_- H_0$, $H_- H_0 H_-$, $H_- H_- H_0$
d quark	$\bar{T}\bar{V}\bar{V}$, $\bar{V}\bar{T}\bar{V}$, $\bar{V}\bar{V}\bar{T}$	H_- H0 H_0, H_0 H_- H_0, H_0 H_0 H_-

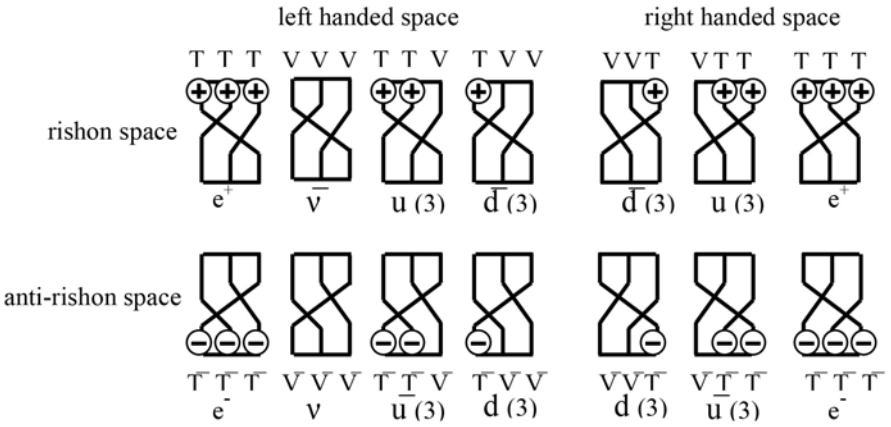

Figure 5. The fermions are represented by the rishon space and helon. Charged fermions have two handedness states each, while ν and $\bar{\nu}$ have only one each. (3) denotes that there are three possible permutations, identified as the quark colors.

$$\begin{aligned}&\text{zero-energy groud state space} \xrightarrow{\text{spontaneous symmetry breaking}}\\ &\text{nonzero-energyscalar Higgs field} \xrightarrow{\text{massless particle}}\\ &\left[\text{the transitional nonzero-energy Higgs field} - \text{particle composite}\right]\\ &\xrightarrow{\text{spontaneous symmetry restoring}} \text{massive particle with the longitudinal}\\ &\text{component on zero-energy ground state space without the Higgs field}\end{aligned} \tag{2}$$

In conventional physics, the nonzero-energy scalar Higgs Field exists permanently in the universe. The problem with such nonzero-energy field is the cosmological constant problem from the huge gravitational effect by the nonzero-energy Higgs field in contrast to the observation [15].

Unlike passive space in conventional physics, the Higgs space [16] as the zero-energy ground state space couples with particles. Attachment space is the space precursor of the Higgs field. Under spontaneous symmetry breaking, attachment space as the active zero-energy ground state space couples with massless particle to form momentarily the transitional non-zero energy Higgs field-particle composite. The Higgs field is momentary and transitional, avoiding the cosmological constant problem. Under spontaneous symmetry restoring,

the transitional nonzero-energy Higgs field-particle composite is converted into massive particle with the longitudinal component on zero-energy attachment space without the Higgs field as follows.

$$\begin{aligned}&\text{massless particle} + \text{zero-energy attachment space} \xrightarrow{\text{spontaneous symmetry breaking}} \\ &\left[\text{the transitional non-zero energy Higgs field} - \text{particle composite}\right] \\ &\xrightarrow{\text{spontaneous symmetry restoring}} \text{massive particle with the longitudinal} \\ &\text{component on zero-energy attachment space without the Higgs field}\end{aligned} \tag{3}$$

Detachment space is the space precursor of the reverse Higgs field. Unlike the conventional model, detachment space actively couples to massive particle. Under spontaneous symmetry breaking, the coupling of massive particle to zero-energy detachment space produces the transitional nonzero-energy reverse Higgs field-particle composite which under spontaneous symmetry restoring produces massless particle on zero-energy detachment space without the longitudinal component without the reverse Higgs field as follows.

$$\begin{aligned}&\text{massive particle} + \text{zero-energy detachment space} \xrightarrow{\text{spontaneous symmetry breaking}} \\ &\left[\text{the transitional nonzero-energy reverse Higgs field} - \text{particle composite}\right] \\ &\xrightarrow{\text{spontaneous symmetry restoring}} \text{massless particle without the longitudinal} \\ &\text{component on zero-energy detachment space without the reverse Higgs field}\end{aligned} \tag{4}$$

For the electroweak interaction in the Standard model where the electromagnetic interaction and the weak interaction are combined into one symmetry group, under spontaneous symmetry breaking, the coupling of the massless weak W, weak Z, and electromagnetic A (photon) bosons to zero-energy attachment space produces the transitional nonzero-energy Higgs fields-bosons composites which under partial spontaneous symmetry restoring produce massive W and Z bosons on zero-energy attachment space with the longitudinal component without the Higgs field, massless A (photon), and massive Higgs boson as follows.

$$\begin{aligned}&\text{massless WZ} + \text{zero-energy WZ attachment space} + \text{massless A} \\ &+ \text{zero-energy A attachment space A} \xrightarrow{\text{spontaneous symmetry breaking}} \\ &\left[\text{the transitional nonzero-energy WZ Higgs field} - \text{WZ composite}\right] \\ &+ \left[\text{nonzero-energy A Higgs field} - \text{A composite}\right] \xrightarrow{\text{partial spontaneous symmetry restoring}} \\ &\text{massive WZ with the longitudinal component on attachment space without} \\ &\text{the Higgs field} + \text{massless A} + \text{the nonzero energy massive Higgs boson}\end{aligned} \tag{5}$$

In terms of mathematical expression, the conventional permanent Higgs field model and the transitional Higgs field model are identical. The interpretations of the mathematical expression are different for the permanent Higgs field model and the transitional Higgs field model. The transitional Higgs field model avoids the cosmological problem in the permanent Higgs field model.

In the Higgs mechanism, gauge bosons are assumed to be massless originally. Elementary fermions (leptons and quarks) can be assumed to be massive originally. However, the observed neutrinos are nearly massless and left-handed only.

The paper posits that the left handed became massless through the reverse Higgs mechanism. For the symmetrical massive left handed neutrinos and right-handed neutrinos under spontaneous symmetry breaking, the coupling of the massive left handed neutrinos and the massive right handed neutrinos to zero-energy detachment space produces the transitional nonzero-energy reverse Higgs fields-neutrinos composites which under partial spontaneous symmetry restoring produce massless left handed neutrinos on zero-energy detachment space without the longitudinal component without the reverse Higgs field, massive right-handed neutrinos (dark matter), and the massive reverse Higgs boson as follows.

$$\begin{aligned}&\text{massive } \nu_{\mathrm{L}} + \text{zero energy } \nu_{\mathrm{L}} \text{ detachment space} + \text{massive } \nu_{\mathrm{R}}\\&+ \text{zero-energy } \nu_{\mathrm{R}} \text{ detachment space} \xrightarrow{\text{spontaneous symmetry breaking}}\\&\left[\text{the transitional nonzero-energy } \nu_{\mathrm{L}} \text{ reverse Higgs field} - \nu_{\mathrm{L}} \text{ composite}\right]\\&+\left[\text{nonzero-energy } \nu_{\mathrm{R}} \text{ reverse Higgs field} - \nu_{\mathrm{R}} \text{ composite}\right]\\&\xrightarrow{\text{partial spontaneous symmetry restoring}} \text{massless } \nu_{\mathrm{L}} \text{ without the longitudinal}\\&\text{component on det achment space without the Higgs field}\\&+\text{massive } \nu_{\mathrm{R}} + \text{the nonzero energy massive reverse Higgs boson}\end{aligned} \tag{6}$$

As described in the previous paper [21], the reverse Higgs boson was observed as the two unusual steeply upward-going ultra-high-energy (UHE) cosmic ray events with energies of ≈0.6 EeV [23] and ≈0.56 EeV [24] in the Antarctic Impulsive Transient Antenna (ANITA) experiment [25]. These shower events have the characteristics of the decay of a tau lepton, which emerges from the surface of the ice, and the tau lepton is explained as the product of a UHE parent tau neutrino by the charged-current interactions with the Earth matter. However, such UHE tau neutrino cannot survive the passage through the Earth. The previous paper posits that the upward-going ANITA events are derived from the cosmic ray of the baryonic-dark matter reverse Higgs boson that travels through the Earth. The calculated value for the reverse Higgs boson is 0.47 EeV in good agreement with the observed 0.56 and 0.6 EeV. As shown in Section 4, dark matter (sterile neutrinos) is part of the periodic table of elementary particles for baryonic matter and dark matter.

3.2. The Space Structures

The symmetrical combination of n units of attachment space as 1 and n units of detachment space as 0 brings about three different space structures: binary partition space, miscible space, or binary lattice space as below.

$$\underset{\text{attachment space}}{(1)_n} + \underset{\text{detachment space}}{(0)_n} \xrightarrow{\text{combination}} \underset{\text{binary partition space,}}{(1)_n(0)_n}, \quad \underset{\text{miscible space,}}{(1+0)_n}, \text{ or } \underset{\text{binary lattice space}}{(1\,0)_n} \tag{7}$$

Binary partition space, $(1)_n(0)_n$, consists of two separated continuous phases of multiple quantized units of attachment space and detachment space. In miscible space, $(1+0)_n$, attachment space is miscible to detachment space, and there is no separation of attachment space and detachment space. Binary lattice space, (1

$0)_n$, consists of repetitive units of alternative attachment space and detachment space. In conventional physics, space does not couple with particles. In the rest-movement system, space couples with particles.

In binary partition space $(1)_n(0)_n$, an entity is both in constant motion as standing wave for detachment space and in stationary state as a particle for attachment space, resulting in the wave-particle duality. Such duality can be described by the uncertainty principle. The uncertainty principle for quantum mechanics is expressed as follows.

$$\sigma_x \sigma_p \geq \frac{\hbar}{2} \tag{8}$$

The position, x, and momentum, p, of a particle cannot be simultaneously measured with arbitrarily high precision. The uncertainty principle requires every physical system to have a zero-point energy (non-zero minimum momentum) and to have a non-zero minimum wavelength as the Planck length. In terms of the binary partition space, detachment space relating to kinetic energy as momentum is σ_p, and attachment space relating to space (wavelength) for a particle is σ_x. In binary partition space, neither detachment space nor attachment space is zero in the uncertainty principle, and detachment space is inversely proportional to attachment space. Quantum mechanics for a particle follows the uncertainty principle defined by binary partition space. Binary partition space $(1)_n(0)_n$ can also be described by the Schrodinger in quantum mechanics where total energy equals to kinetic energy related to $(0)_n$ plus potential energy related to $(1)_n$.

In binary partition space, for every detachment space, there is its corresponding adjacent attachment space. Thus, no part of the mass-energy can be irreversibly separated from binary partition space, and no part of a different mass-energy can be incorporated in binary partition space. Binary partition space represents coherence as wavefunction. Binary partition space is for coherent system. Any destruction of the coherence by the addition of a different mass-energy to the mass-energy causes the collapse of binary partition space into miscible space. The collapse is a phase transition from binary partition space to miscible space.

$$\underset{\text{binary partition space}}{(0)_n (1)_n} \xrightarrow{\text{collapse}} \underset{\text{miscible space}}{(0+1)_n} \tag{9}$$

Another way to convert binary partition space into miscible space is gravity. Penrose [26] pointed out that the gravity of a small object is not strong enough to pull different states into one location. On the other hand, the gravity of large object pulls different quantum states into one location to become miscible space. Therefore, a small object without outside interference is always in binary partition space, while a large object is never in binary partition space.

The information in miscible space is contributed by the miscible combination of both attachment space and detachment space, so information can no longer be non-localized. Any value in miscible space is definite and deterministic. All

observations in terms of measurements bring about the collapse of wavefunction, resulting in miscible space that leads to eigenvalue as definite quantized value. Such collapse corresponds to the appearance of eigenvalue, E, by a measurement operator, H, on a wavefunction, Ψ.

$$H\Psi = E\Psi \tag{10}$$

In miscible space, attachment space is miscible to detachment space, and there is no separation of attachment space and detachment space. In miscible space, attachment space contributes zero speed, while detachment space contributes the speed of light. For a moving massive particle consisting of a rest massive part and a massless part, the massive part with rest mass, m_0, is in attachment space, and the massless part with kinetic energy, K, is adjacent to detachment space. The combination of the massive part in attachment space and massless part in detachment leads to the propagation speed in between zero and the speed of light. To maintain the speed of light constant for a moving particle, the time (t) in moving particle has to be dilated, and the length (L) has to be contracted relative to the rest frame.

$$\begin{aligned} t &= t_0 \Big/ \sqrt{1 - v^2/c^2} = t_0\gamma, \\ L &= L_0/\gamma, \\ E &= K + m_0c^2 = \gamma m_0c^2 \end{aligned} \tag{11}$$

where $\gamma = 1\Big/\left(1 - v^2/c^2\right)^{1/2}$ is the Lorentz factor for time dilation, and length contraction, E is the total energy, and K is the kinetic energy. Binary lattice space, (1 0)n, as the space of virtual gauge rishon boson in quantum field theory will be described in Section 4.

4. Cosmology

The paper posits that the cyclic universe cosmology in the multiverse involves the split of the membrane 11D spacetime into the 1D eleventh dimension orbifold interval space to form gravity, the 6D discrete interior rishon space (TTT-VVV for positron-neutrino or TTV-TVV for u-$\bar{\text{d}}$ quarks) to form the Standard Model, the 3D Higgs space (attachment space to attach matter or detachment space to detach matter) to form the Higgs or reverse Higgs field, and 1D Einstein time to be shared by all spaces.

4.1. The Multiverse

This paper posits that the origin of the split is derived from the cyclic universe cosmology in the multiverse. The multiverse consists of the zero-energy inter-universal void with 4D detachment space and the multiple 11D positive-energy membrane and negative-energy anti-membrane dual universes with 11D attachment space which has zero total energy. Detachment space in the inter-universal void prevents the collision of the 11D dual universes, while attachment space in the dual universe allows the existence of mass-energy in the space of the dual universe. The dual universe with zero total energy can emerge

from the zero-energy inter-universe. Each of the positive-energy 11D universe and the negative-energy 11D universe does not conserve the energy-mass conservation, but the energy sum of the positive-energy 11D universe and the negative-energy 11D universe is zero which conserves the energy-mass conservation.

The cyclic universe cosmology starts with the zero-energy inter-universal void and the positive-negative energy 11D membrane dual universe which is split into four 10D string branes as the dual two-string branes, including the positive-energy weak-gravity string brane, the negative-energy weak-gravity string brane, the positive-energy strong-gravity string brane, and the negative-energy strong-gravity string brane in the 11D dual universe bulk. The positive-energy weak string brane contains matter, while the negative-energy string brane contains antimatter. The matter-antimatter balance occurs in the balance between the matter in the positive-energy weak-gravity string brane and the antimatter in the negative-energy weak-gravity string brane as in Figure 6. Each brane has the matter-antimatter imbalance initially. Afterward, all subsequent events in each brane have the matter-antimatter balance for CP symmetry. The strong string branes are dominated by gravity. All four branes have equal mass-energy. The 1D interval space is between the 10D strong-gravity string brane and the 10D weak-gravity string brane in the 11D membrane bulk.

In conventional physics, space-time dimension numbers are fixed. Compactization is required to account for the observed 4D [2]. As described previously [19] [20], the space-time dimension numbers oscillate reversibly between 10D and 4D reversibly dimension by dimension without compactization. The oscillating space-time numbers from 10D to 4D relate to varying speed of light. Varying speed of light has been proposed to explain the horizon problem of cosmology [27] [28]. J. D. Barrow [29] proposes that the time dependent speed of light varies as some power of the expansion scale factor *a* in such way that

$$c(t) = c_0 a^n, \tag{12}$$

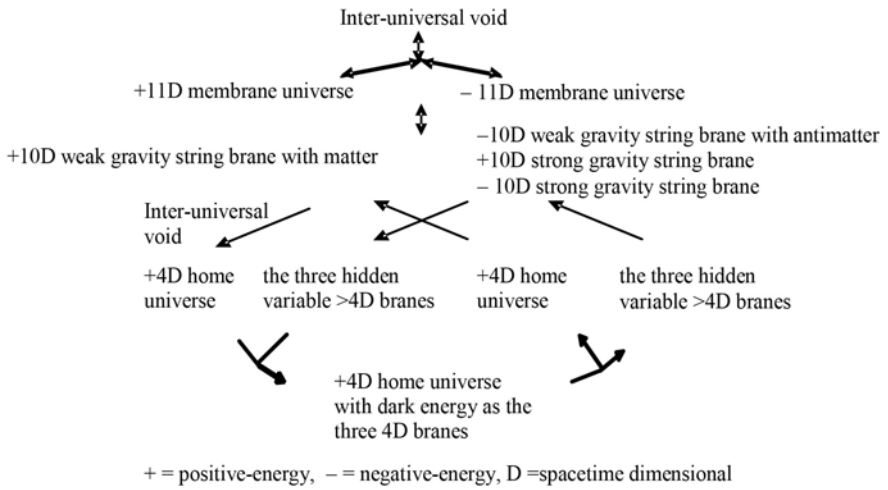

Figure 6. The reversible cyclic universe.

where c is the speed of light and n are constants. The increase of speed of light is continuous.

In this paper, the speed of light is invariant in a constant space-time dimension number, and the speed of light varies with varying space-time dimension number from 4 to 11 as follows.

$$c_{\mathrm{D}} = c/\alpha^{\mathrm{D}-4}, \tag{13}$$

where c is the observed speed of light in the 4D space-time, c_{D} is the quantized varying speed of light in space-time dimension number, D, from 4 to 10, and α is the fine structure constant for electromagnetism. The speed of light increases with the increasing space-time dimension number D. Since the speed of light for >4D particle is greater than the speed of light for 4D particle, the observation of >4D particles by 4D particles violates casualty. Thus, >4D particles are hidden particles with respect to 4D particles. Particles with different space-time dimensions are transparent and oblivious to one another, and separate from one another if possible.

As described previously [19] [20], the particle oscillation between 10D and 10D through 4D involves mass dimension (denoted as d) to represent the mass. In the initial condition for the oscillation, D + d =14 where D and d are between 4 and 10. For an example, a dimension has a dual spacetime-mass dimension numbers of 10D4d or 4D10d. The transformations for oscillating dimension number between 10D and 4D consist of the varying speed of light dimensional (VSLD) transformation for spacetime dimension D and the varying supersymmetry dimensional (VSD) transformation for mass dimension d. For the VSLD transformation for D, $E = M_0c^2$ modified by Equation (13) is expressed as

$$E = M_0c_{\mathrm{D}}^2 = M_0 \cdot \left(c^2/\alpha^{2(\mathrm{D}-4)}\right), \tag{14}$$

$$M_{0,\mathrm{D,d}} = M_{0,\mathrm{D}-n,\mathrm{d}+n}\alpha^{2n}, \tag{15}$$

$$E_{\mathrm{vacuum,D}} = E - M_{0,\mathrm{D}}c^2, \tag{16}$$

$$\mathrm{D,d} \xrightarrow{\text{VSLD transformation}} (\mathrm{D} \mp n), (\mathrm{d} \pm n) \tag{17}$$

where c_{D} is the quantized varying speed of light in space-time dimension number, D, from 4 to 10, c is the observed speed of light in the 4D space-time, α is the fine structure constant for electromagnetism, E is energy, M_0 is rest mass, D is the space-time dimension number from 4 to 10, d is the mass dimension number from 4 to 10, n is an integer, and E_{vacuum} = vacuum energy. From Equation (14), 10D has the lowest rest mass, and 4D has the highest rest mass. According to the calculation from Equation (15), the rest mass of 4D is $1/\alpha^{12} \approx 137^{12}$ times of the mass of 10D. From Equation (16), 10D has the highest vacuum energy, while 4D particle has zero vacuum energy. A particle with 10D is transformed to a particle with 4D from Equation (17) through the VSLD transformation. Spacetime dimension number decreases with decreasing speed of light, decreasing vacuum energy, and increasing rest mass. The 4D and the 10D have zero and the highest vacuum energies, respectively.

In the normal supersymmetry transformation, the repeated application of the fermion-boson supersymmetry transformation carries over a boson (or fermion) from one point to the same boson (or fermion) at another point at the same mass, resulting in translation without changing mass. Under the varying supersymmetry dimensional (VSD) transformation, the repeated application of the fermion-boson supersymmetry transformation carries over a boson from one point to the boson at another point at different mass dimension number at different mass, resulting in translation and fractionalization or condensation. The repeated VSD transformation carries over a boson B_d into a fermion F_d and a fermion F_d to a boson B_{d-1}, which can be expressed as follows.

$$M_{d,F} = M_{d,B}\alpha_{d,B}, \tag{18}$$

$$M_{d-1,B} = M_{d,F}\alpha_{d,F}, \tag{19}$$

where $M_{d,B}$ and $M_{d,F}$ are the masses for a boson and a fermion, respectively, d is the mass dimension number, and $\alpha_{d,B}$ or $\alpha_{d,F}$ is the fine structure constant that is the ratio between the masses of a boson and its fermionic partner. where $M_{d,B}$ and $M_{d,F}$ are the masses for a boson and a fermion, respectively, d is the mass dimension number, and $\alpha_{d,B}$ or $\alpha_{d,F}$ is the fine structure constant that is the ratio between the masses of a boson and its fermionic partner. Assuming α's are the same, it can be expressed as

$$M_{d,B} = M_{d+1,B}\alpha_{d+1}^2. \tag{20}$$

The varying supersymmetry transformation involves the translation and fractionalization from d to d − 1 or condensation from d to d + 1 at the same D. The translation and fractionalization-condensation account for the cosmic expansion-contraction for the oscillating universes.

The transformation during the oscillation between 10D particle and 4D particle involves the stepwise two-step transformation consisting of the VSLD transformation and the VSD transformation. The VSLD transformation involves the transformation of spacetime dimension, D whose mass increases with decreasing D for the decrease in vacuum energy. The VSD transformation involves the transformation of the mass dimension number, d whose mass decreases with decreasing d for the fractionalization of particle. The oscillating dimension number transformation between 10D4d and 10D4d through 4D4d involves both the VSLD transformation and the VSD transformation as the stepwise two-step transformation as follows.

stepwise two-step varying transformation

$$\begin{aligned} &(1)\quad \mathrm{D,d} \xleftrightarrow{\text{VSLD transformation}} (\mathrm{D}\mp 1),(\mathrm{d}\pm 1) \\ &(2)\quad \mathrm{D,d} \xleftrightarrow{\text{VSD transformation}} \mathrm{D},(\mathrm{d}\pm 1) \end{aligned} \tag{21}$$

The repetitive stepwise two-step dimension number oscillation between 10D4d and 10D4d through 4D4d as follows.

$$\begin{aligned} &10\mathrm{D4d} \to 9\mathrm{D5d} \to 9\mathrm{D4d} \to 8\mathrm{D5d} \to 8\mathrm{D4d} \to 7\mathrm{D5d} \to 7\mathrm{D4d} \to 6\mathrm{D5d} \\ &\to 6\mathrm{D4d} \to 5\mathrm{D5d} \to 5\mathrm{D4d} \to 4\mathrm{D5d} \to 4\mathrm{D4d} \to 5\mathrm{D4d} \to 5\mathrm{D5d} \to 6\mathrm{D4d} \\ &\to 6\mathrm{D5d} \to 7\mathrm{D4d} \to 7\mathrm{D5d} \to 8\mathrm{D4d} \to 8\mathrm{D5d} \to 9\mathrm{D4d} \to 9\mathrm{D5d} \to 10\mathrm{D4d} \end{aligned} \tag{22}$$

As described previously [19] [20], the oscillation between 10D and 4D results in the reversible cyclic fractionalization-contraction for the reversible cyclic expansion-contraction of the universe.

4.2. The Home Universe

To form the home universe where we inhabit, the 10D positive-energy weak-gravity string brane with attachment space absorbed the zero-energy 4D inter-universal void with 4D detachment space, resulting in the home universe which contains the Higgs space with both attachment space for rest mass and detachment space for kinetic energy. The home universe resulted from the transformation from a 10D spacetime brane into a 4D spacetime universe by transforming 6D connected exterior space into 6D discrete interior rishon space. The other three 10D string branes did not absorb detachment space. From 10^{-36} seconds after the entrance of detachment space to the time between 10^{-33} and 10^{-32} seconds after the entrance of detachment space, four important events occurred to transform the 10D positive-energy weak-gravity string brane into the 4D home universe where we inhabit. The four events are cosmic inflation derived from the transformation from 10D4d to 4D10d, the rishon space formation by transforming 6D connected exterior space into 6D discrete interior rishon space, the Higgs space formation by the combination of attachment space and detachment space, and the Extend Standard Model from the periodic table of elementary particles based on the seven mass dimensions.

4.2.1. Cosmic Inflation

Cosmic inflation is derived the transformation from 10D4d to 4D10d immediately. Calculated from Equation (15), the rest mass of 4D10d is $M_{0,10} = M_{0,4} / \alpha^{2(10-4)?} \approx 137^{12}$ times of the rest mass of 10D4d, resulting in cosmic inflation as the exponential expansion of space from the high vacuum energy 10D4d to the zero vacuum energy 4D10d as follows.

$$\begin{array}{l}\underline{\text{inflation}} \\ \text{10D4d spacetime} + \text{1D interval space for gravity} \xrightarrow{\text{quick VSLD transformation}} \\ \text{4D10d spacetime} + \text{1D interval space for gravity}\end{array} \tag{23}$$

4.2.2. The Rishon Space Formation

The home universe resulted from the transformation from a 10D spacetime brane into a 4D spacetime universe by transforming 6D connected exterior space into 6D discrete interior rishon space as follows.

$$\begin{array}{l}\text{10D connected exterior spacetime for string} \xrightarrow{\text{from 10D to 4D}} \\ \text{4D connected exterior spacetime} + \text{6D discrete interior rishon} \\ \text{space}(\text{TTTVVV}) \text{for e-}\nu \text{ or 4D connected exterior spacetime} \\ \text{+6D discrete interior rishon space}(\text{TTVTVV}) \text{for u-}\bar{\text{d}} \longrightarrow \\ \text{TTT for e and VVV for } \nu \text{ or TTV for u and TVV for } \bar{\text{d}} \\ \text{in 4D connected exterior spacetime}\end{array} \tag{24}$$

The rishon space formation produces the discrete space in addition to connected space. All elementary particles are in discrete space in addition to connected space, while gravity in the interval space continues to be in connected exterior space without discrete interior space for flavor, charge, isospin, and color.

4.2.3. The Higgs Space Formation

As discussed in Section 3, the space structures as the mixed Higgs spaces as the combinations of n units of attachment space (denoted as 1 from the positive-energy weak-gravity string brane) and n units of detachment space (denoted as 0 from the inter-universal void) consist of binary partition space, $(1)_n(0)_n$, as the space of wave-particle duality, binary miscible space, $(1+0)_n$, as the space of relativity, and binary lattice space, $(1\ 0)_n$, as the space of virtual gauge boson in quantum field theory. Section 3 describes binary partition space and binary miscible space, and binary lattice space is described as follows.

Binary lattice space is derived from the slicing of mass dimension. Bounias and Krasnoholovets [30] propose that the reduction of dimension can be done by slicing dimension, such as slicing 3 space dimension object (block) into infinite units of 2 space dimension objects (sheets). Cosmic inflation involves the transformation from 10D4d with high vacuum energy into 4D10d with zero vacuum energy at once. 4D10d particle was sliced into six different particles: 4D9d, 4D8d, 4D7d, 4D6d,4D5d, and 4D4d equally by mass. Baryonic matter is 4D4d which is the lowest spacetime-mass dimension from Equation (22), while dark matter consisted of the other five types of particles (4D9d, 4D8d, 4D7d, 4D6d, and 4D5d) as follows.

$$\begin{aligned}&\text{10D4d} \xrightarrow{\text{cosmic inflation}} \text{4D10d} \xrightarrow{\text{the slicing}} \\ &\text{baryonic matter}\left(\text{4D4d}\right)+\text{dark matter}\left(\text{4D5d, 4D6d, 4D7d, 4D8d, 4D9d}\right)\end{aligned} \tag{25}$$

As a result, the mass ratio of dark matter to baryonic matter is 5 to 1 in excellent agreement with the observed 4.98 to 1 derived from the observed 4.56% and 22.7% for baryonic matter and dark matter, respectively [19] [31].

The 10d (mass dimension) particle in attachment space denoted as 1 was sliced by detachment space denoted as 0. For example, the slicing of 10d particle into 4d particle is as follows.

$$\begin{aligned}&1_{10} \xrightarrow{\text{slicing}} 1_4 \quad \sum_{\text{d}=5}^{10}\left(0_4\ 1_4\right)_{n,\text{d}} \\ &\text{10d particle} \quad \text{4d core particle} \quad \text{binary lattice space}\end{aligned} \tag{26}$$

where 1_{10} is 10d particle, 1_4 is 4d particle, d is the mass dimension number of the dimension to be sliced, n as the number of slices for each dimension, and $(0_4\,1_4)_n$ is binary lattice space with repetitive units of alternative 4d attachment space and 4d detachment space. For 4d particle starting from 10d particle, the mass dimension number of the dimension to be sliced is from d = 5 to d = 10. Each mass dimension is sliced into infinite quantized units (n = ∞) of binary lattice space, $(0_4,\ 1_4)_\infty$. For 4d particle, the 4d core particle is surrounded by 6 types (from d = 5 to d = 10) of infinite quantized units of binary lattice space. Such in-

finite quantized units of binary lattice space represent the infinite units (n = ∞) of separate energy virtual orbitals (probabilities) for virtual particles in a gauge force field. There are six gauge fields from d = 5 to d =10. The three force fields, electromagnetism, the strong force, and the weak force are represented by d = 5, 6, and 7, respectively. For dark matter, d =5 for electromagnetism is not sliced, so dark matter does not have electromagnetism at d = 5, resulting in the darkness due to the absence of photon from electromagnetism.

The Higgs space produces the Higgs mechanism and the space structures. Quantum mechanics is derived from the Higgs space, so the simultaneous occurrence of cosmic inflation and quantum mechanism produced cosmic quantum fluctuation in the home universe.

4.2.4. The Extend Standard Model

The Extend Standard Model includes leptons, quarks, gauge bosons, gravity, dark matter, and dark energy.

The Seven Mass Dimensions

The masses in the Extend Standard Model are based on the seven mass dimensions. Cosmic inflation produced 4D10d spacetime and 1D interval space for gravity which were transformed into 4D4d spacetime as the lowest spacetime-mass dimension from Equation (22) + 1D interval space for gravity + 6 mass dimensions for non-gravity + 1mass dimension for gravity. The combination results in 4D4d spacetime + 1D interval space for gravity + 7 mass dimensions as Equation (27) and in Figure 7.

$$\begin{aligned}&10\text{D4d}+1\text{D interval space for gravity}\xrightarrow{\text{cosmic inflation}}\\&4\text{D10d spacetime}+1\text{D interval space for gravity}\longrightarrow 4\text{D4d spacetime}\\&+1\text{D interval space for gravity}+6\text{ mass dimensions for non-gravity}\\&+1\text{ mass dimension for gravity}\xrightarrow{\text{combinasion}}4\text{D4d spacetime}\\&+1\text{D interval space for gravity}+7\text{ mass dimensions}\end{aligned}\tag{27}$$

The seven mass dimensions are arranged as F_5 B_5 F_6 B_6 F_7 B_7 F_8 B_8 F_9 B_9 F_{10} B_{10} F_{11} B_{11}, where F_d and B_d are mass dimensional fermion and mass dimensional boson, respectively. Under the varying supersymmetry dimensional (VSD) transformation, the mass of mass dimensional fermion and the mass of mass dimensional boson are related to each other with three simple formulas as follows.

$$M_{\mathrm{d,B}} = M_{\mathrm{d,F}} / \alpha_{\mathrm{d}} \tag{28}$$

$$M_{\mathrm{d+1,F}} = M_{\mathrm{d,}B} / \alpha_{\mathrm{d+1}} \tag{29}$$

$$M_{\mathrm{d+1,B}} = M_{\mathrm{d,B}} / \alpha_{\mathrm{d+1}}^2 , \tag{30}$$

where d is the mass dimension number, F is fermion, and B is boson. Each dimension has its own α_d, and all α_d's except α_7 (α_w) of the seventh dimension (weak interaction) are equal to α, the fine structure constant of electromagnetism.

For baryonic matter, with electromagnetism at d = 5, electron appears in addition to neutrino. Without electromagnetism at d = 5, dark matter does not

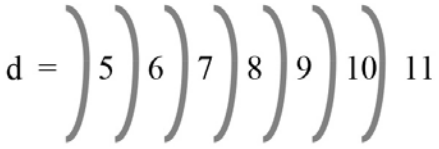

Figure 7. The 7 mass dimensions.

have charge particle. For baryonic matter, to represent the mixed rishon space (TTV-TVV) for charge u-$\bar{d}$ quarks, the additional seven mass dimensions as the "auxiliary mass dimensions" (a's) to represent quarks and unstable leptons in addition to the seven "principal mass dimensions" (d's) to represent neutrino-electron and gauge bosons as in Figure 8.

The Periodic Table of Elementary Particles

The periodic table of elementary particles [21] [22] is based on the seven principal mass dimensions (d's) for stable baryonic matter leptons (electron and neutrinos), gauge bosons (all forces), gravity, and dark matter (five sterile dark matter neutrinos) and the seven auxiliary mass dimensions (a's) for unstable leptons (muon and tau) and quarks (d, u, s, c, b, and t) as in Figure 8 and Table 3.

In the periodic table of elementary particles, the five dark matter particles are derived from Equation (24). Without electromagnetism at d = 5, dark matter does not have charge particle, and has to be neutrinos. Initially derived from Equation (25) and the symmetry between dark matter and baryonic matter, there were five dark matter massive right-handed neutrinos and one baryonic matter massive left-handed neutrino. Through the reverse Higgs mechanism as Equation (6), the left-handed neutrino becomes massless, while the right-handed neutrinos as sterile dark matter neutrinos remain massive. The reverse Higgs boson was observed [21]. All neutrinos and electron as well as gauge bosons are in the principal mass dimensions. All quarks and unstable leptons are in the auxiliary mass dimensions. The three generations of baryonic matter lepton-quark is the maximum generations allowed for the seven principal dimensions and the seven auxiliary dimensions.

Gauge Bosons

In the periodic table of elementary particles, the given observed masses are the mass of electron for F_6 and the mass of Z boson for B_7. From Equations (28) and (30), $\alpha_w = \alpha_7 = \alpha$ of week interaction = $\left(M_{B_6}/M_{B_7}\right)^{1/2}$ = $\left(M_{F_6}/\alpha/M_{B_7}\right)^{1/2}$ = $\left(M_e/\alpha/M_Z\right)^{1/2}$ = 0.02771. Therefore, the masses of gauge bosons are as in Table 4.

The lowest energy gauge boson (B_5) at d = 5 is the Coulomb field for electromagnetism. The second gauge lowest boson (B_6) at d = 6 is basic gluon (g* = 70 MeV ≈ one half of pion) is the strong force as the nuclear force in the pion theory [32] where pions mediate the strong interaction at long enough distances (longer than the nucleon radius) or low enough energies. B_6 is denoted as basic gluon, g*. At short enough distances (shorter than the nucleon radius) or high

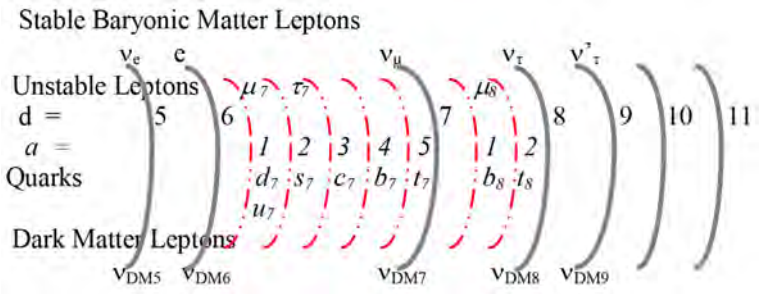

Figure 8. The seven principal mass dimensions (solid lines) denoted by the principal mass dimension number d and the seven auxiliary mass dimensions (dash-dotted lines) denoted by the auxiliary mass dimension number *a*.

Table 3. The periodic table of elementary particles for baryonic matter and dark matter d = principal mass dimension number, a = auxiliary mass dimension number, DM = dark matter, BM = baryonic matter.

d	a = 0	a = 0	1	2	1	2	3	4	5	a = 0
	Stable Baryonic Matter Leptons	Dark Matter Leptons	Unstable Leptons		Quarks					Bosons
5	ν_e	ν_{DM5}								B_5 = A electromagnetism
6	e	ν_{DM6}								B_6 = g* strong (basic gluon)
7	ν_μ	ν_{DM7}	μ_7	τ_7	d_7/u_7	s_7	c_7	b_7	t_7	$B_7 = Z_L^0$ left-handed BM weak
8	ν_τ	ν_{DM8}	μ_8 (absent)		b_8 (absent)	t_8				$B_8 = Z_R^0$ right-handed DM weak
9	ν'_τ (high-mass ν_τ)	ν_{DM9}								B_9 = BM-DM separation
10										B_{10} = matter-antimatter separation B_{10} = home universe-dark energy separation
11	gravitino									B_{11} = gravity (interval space)

Table 4. The masses of the principal mass dimensions (gauge bosons).

B_d	M_d	GeV (calculated)	Gauge boson	Interaction
B_5	$M_e a$	3.7×10^{-6}	A = photon	Electromagnetic
B_6	M_e / a	7×10^{-2} (70.02 MeV)	g* = basic gluon	Strong
B_7	$M_Z = M_{B_6}/\alpha_w^2$	91.1876 (given)	Z_L	weak (left) for baryonic matter
B_8	$M_7/a^2 = M_Z/\alpha^2$	1.71×10^6	Z_R	weak (right) for dark matter
B_9	$M_8/a^2 = M_Z/\alpha^4$	3.22×10^{10}		baryonic matter-dark matter separation
B_{10}	$M_9/a^2 = M_Z/\alpha^6$	6.04×10^{14}		matter-antimatter separation home universe-dark energy separation
B_{11}	$M_{10}/a^2 = M_Z/\alpha^8$	1.13×10^{19}	G	Gravity (interval space)

enough energies, gluons emerge to confine fractional charge quarks. Fractional charge quarks are confined by gluons in QCD (quantum chromodynamics). No isolated fractional charge quark is allowed, and only collective integer charge quark composites are allowed. In general, collective fractional charges are confined by the short-distance confinement force field where the sum of the collec-

tive fractional charges is integer [33]. As a result, fractional charges are confined and collective. The confinement force field includes gluons for collective fractional charge quarks in hadrons and the magnetic flux quanta for collective fractional charge quasiparticles in the fractional quantum Hall effect (FQHE) [34] [35] [36].

The third lowest boson (B_7) at d = 7 is Z_L for the left-handed weak interaction among leptons and quarks. Spontaneous symmetry breaking produces massive weak bosons, massless photon and the Higgs boson as Equation (5). Massive weak bosons produce short-distance interaction. B_8 at d = 8 is Z_R for the right-handed weak interaction among dark matter neutrinos as dark matter neutrino oscillation. The symmetry between Z_R and Z_L provides the neutrino oscillation for both baryonic matter neutrinos [37] and dark matter neutrinos.

At B_9, baryonic matter and dark matter are separated. Above B_9, there is no baryonic matter and dark matter before the slicing as in Equation (25). B_9 as the gauge boson represents the weak short-distance repulsive Yukawa force [38] between baryonic matter and dark matter. Long-distance attractive gravity among all particles in a random mixture of dark matter particles and baryonic matter particles overcomes the weak short-distance repulsive force between dark matter particles and baryonic matter particles. However, a large amount of homogeneous dark matter particles repulses a large amount of homogeneous baryonic matter particles in the short-distance interfacial region between a large amount of homogeneous dark matter particles and a large amount of homogeneous baryonic matter particles. This repulsive force is same as the Yukawa force for baryonic matter [39] [40] in the Moffat's Modified Gravity (MOG) theory, and explains the evolution of galaxy [41]. This repulsive force prevents the catch and the direct detection of dark matter particles on earth with a large amount of homogeneous baryonic matter particles.

B_{10} at d = 10 is for the matter-antimatter separation. At B_{10}, matter is in our home universe as the positive energy 10D string brane, while antimatter is in the negative energy 10D string brane. Above B_{10}, there is no string brane as in **Figure 6**. As in **Figure 6**, B_{10} at d = 10 is also for the home universe-dark energy separation. Above B_{10}, there is no separation between the home universe and the three string branes. B_{10} as the gauge boson represents the repulsive force between matter in the home universe and antimatter in the negative-energy weak gravity brane and between the home universe and dark energy in the three branes.

B_{11} is for gravity in the interval space. F_{11} (8.275×10^{16} GeV) relates to spin 3/2 gravitino, while B_{11} (1.134×10^{19} GeV) relates to spin 2 graviton. In supersymmetry, gravitino and graviton mediate the supersymmetry between fermion and boson in space dimension and gravitation. There are 11 space dimensions in the 11 spacetime dimensional membrane. As a result, the supersymmetry involves 11 $F_{11} + B_{11}$, which is equal to 1.225×10^{19} GeV in excellent agreement with the Planck mass (1.221×10^{19} GeV) derived from observed gravity as $(\hbar c/G)^{1/2}$ where c is the speed of light, G is the gravitational constant, and ħ is the reduced Planck

constant. Electromagnetism and gravity are long-distances forces, and all other forces are short-distance.

Leptons and Quarks

The lepton mass formula and the quark mass formula are derived from the incorporation of basic gluon ($g^* = B_6 = 70$ MeV) to electron. The incorporation of basic gluon as flux quanta follows the the composite fermion theory for the FQHE (fractional quantum Hall effect) [42] [43]. In the composite fermion model for FQHE, the formation of composite fermion is through the attachment of an even number of magnetic flux quanta to electron, while the formation of composite boson is through the attachment of an odd number of magnetic flux quanta to electron. In the same way, the formation of composite fermion is through the attachment of an even number of basic gluons to electron, while the formation of composite boson is through the attachment of an odd number of basic gluons to electron. The formation of composite boson is equal to the formation of composite di-leptons, so the formation of composite lepton is through the attachment of one half of an odd number of basic gluons to electron. As a result, the muon (μ) mass formula is as follows.

$$M_{\mu_7} = M_e + 3M_{g^*}/2 = M_e + 3M_e/2\alpha = 105.5488 \text{ MeV}, \tag{31}$$

which is in excellent agreement with the observed 105.6584 MeV [44] for the mass of muon. The masses of leptons follow the Barut lepton mass formula [45] as follows.

$$M_{\text{lepton}} = M_e + \frac{3M_e}{2\alpha}\sum_{a=0}^{n} a^4, \tag{32}$$

where $a = 0$, 1, and 2 are for e, μ_7, and τ_7, respectively. The calculated mass of τ_7 is 1786.2 MeV in good agreement with the observed mass as 1776.82 MeV. According to Barut, the second term, $\sum_{a=0}^{n} a^4$ of the mass formula is for the Bohr-Sommerfeld quantization for a charge-dipole interaction in a circular orbit. The more precise calculated mass of τ for the tau lepton mass formula is as follows.

$$\begin{aligned} M_\tau &= M_e + \left(\frac{3M_e}{2\alpha} - M_e\right)\sum 2^4 \\ &= M_e + \left(17\frac{3M_e}{2\alpha} - 17M_e\right) \\ &= 1777.47 \text{ MeV} \end{aligned} \tag{33}$$

which is in excellent agreement with observed 1776.82 MeV, and means that during this dipole-interaction in a circular orbit for τ, an electron with total mass of $17M_e$ is lost. $17M_e$ is shown as the observed 17 MeV for $34M_e$ in the light boson ($17e\bar{e}$) [46] [47].

Quark has fractional charge (±1/3 or ±2/3), 3-color gluons (red, green, and blue) for $3g^*$, and both the principal mass dimensions and axillary mass dimensions, so similar to Equation (31), d and u in the principal mass dimension involves e/3 or 2e/3 and $3g^*$ as follows.

principal mass dimensional oribital at d = 6

$$\begin{aligned} M_{\text{principal } q} &= \frac{1 \text{ or } 2M_e}{3} + \frac{3\left(3M_{\text{g}^*}\right)}{2} \\ &= \frac{1 \text{ or } 2M_e}{3} + \frac{3\left(3M_{\text{B}_6}\right)}{2} \\ &= \frac{1 \text{ or } 2M_e}{3} + \frac{9M_e}{2\alpha} \end{aligned} \tag{34}$$

For quarks in the auxiliary mass dimensions, 3-color basic gluons (3g*) become 3-color auxiliary basic gluons ($3g^*_{a7}$) at d = 7. Based on Equation (29), auxiliary basic gluon is derived from muon as follows.

$$M_{\text{g}^*_{a7}} = M_{\mu 7}\alpha_w \tag{35}$$

Similar to Equation (31), the masses of quarks in the auxiliary mass dimension are as follows.

auxiliary mass dimensional orbital at d = 7

$$M_{\text{auxiliary } q_7} = \frac{3\left(3M_{g^*_{a7}}\right)}{2}\sum_{a=1}^{n} a^4 = \frac{9M_{\mu 7}\alpha_w}{2}\sum_{a=1}^{n} a^4 \tag{36}$$

The quark mass formula at d = 7 is the combination of Equations (34) and (36) as follows.

$$M_{q_7} = \frac{1 \text{ or } 2M_e}{3} + \frac{9M_e}{2\alpha} + \frac{9M_{\mu 7}\alpha_w}{2}\sum_{a=1}^{n} a^4 \tag{37}$$

where a = 1, 2, 3, 4, and 5 for u_7/d_7, s_7, c_7, b_7, and t_7, respectively.

The quark mass at a = 5 for the auxiliary mass dimension at d = 7 is the maximum mass below the mass of B_7, so the next auxiliary mass dimension has to start from B_7. There are b and t at d = 8, so it is necessary to have μ_8 for the masses of b and t. Like μ_7 in Equation (31), the mass of μ_8 is as follows.

$$\begin{aligned} M_{\mu_8^0} &= 2M_e + 3M_{\text{g}^*_7}/2 \\ &= 2M_e + 3M_{\text{B7}}/2 \\ &= 2M_e + 3M_{\text{Z}^0}/2 \\ &= 136.78 \text{ GeV} \end{aligned} \tag{38}$$

Since at d = 7, there are 3-color basic gluons, at d = 8, 3-*color* basic gluons are not needed, and only one basic gluon (g^*_7) at d = 7 is used. Similar to Equations (34) and (36), the quark mass formulas for the principal and auxiliary mass dimensions are as follows.

principal mass dimensional orbital at d = 7

$$M_{\text{principal quark}} = 3M_{g^*_7}/2 = 3M_{B_7}/2 = 3M_Z/2 \tag{39}$$

auxiliary mass dimensional orbital at d = 8

$$M_{\text{auxiliary quark}} = \frac{3\left(M_{g^*_{a8}}\right)}{2}\sum_{a'=1}^{n'} a'^4 = \frac{3\mu_8^0\alpha}{2}\sum_{a'=1}^{n'} a'^4 \tag{40}$$

The quark mass formula at d = 8 is the combination of Equations (37) and (39) as follows.

$$M_{q8} = \frac{3M_Z}{2} + \frac{3M_{\mu_8^0}\alpha}{2}\sum_{a'=1}^{n'} a'^4 \tag{41}$$

where $a' = 1$ and 2 for b_8 and t_8, respectively.

Combining Equations (37) and (41), the quark mass formula is as follows.

$$M_{\text{quark}} = \frac{1 \text{ or } 2M_e}{3} + \frac{9M_e}{2\alpha} + \frac{9M_{\mu_7}\alpha_w}{2}\sum_{a=1}^{n} a^4 + \frac{3M_Z}{2} + \frac{3M_{\mu_8^0}\alpha}{2}\sum_{a'=1}^{n'} a'^4 \tag{42}$$

where $a = 1$, 2, 3, 4, and 5 for d/u. s, c, b, and t, respectively, and $a' = 1$ and 2 for b and t respectively. The calculated masses for d, u, s, c, b, and t are 328.4 MeV, 328.6 MeV, 539 MeV, 1605.3 MeV, 4974.6 MeV, and 175.4 GeV, respectively. In the standard model, there are three generations of leptons. Extra-muon μ_8 is outside of the three generations of leptons in the standard model, so μ_8 is absent as shown in **Table 2**. As shown in **Table 2**, to be symmetrical to the absent μ_8, b_8 quark is also absent. The calculated mass of top quark is 175.4 GeV in good agreement with the observed 172.4 GeV [44]. The calculated masses are comparable to the quark masses proposed by De Rujula, Georgi, and Glashow [48], Griffiths [49], and El Naschie [50].

The periodic table of elementary particles calculates accurately the particle masses of all leptons, quarks, gauge bosons, the Higgs boson, and the cosmic rays by using only five known constants: the number (seven) of the extra spatial dimensions in the observed four-dimensional spacetime from the eleven-dimensional membrane, the mass of electron, the masses of Z and W bosons, and the fine structure constant [21] [22] [51]. The calculated masses are in excellent agreements with the observed masses. For example, the calculated masses of muon, top quark, and the Higgs boson are 105.55 MeV, 175.4 GeV, and 126 GeV, respectively, in excellent agreements with the observed 105.65 MeV, 172.4 GeV, and 126 GeV, respectively. The calculated masses of hadrons based on the periodic table of elementary particles are in excellent agreement with the observed masses of hadrons [22]. For examples, the calculated masses of proton, neutron, pion ($\pi^{\pm}$), and pion (π^0) are 938.261, 939.425, 139.540, and 134.982 MeV in excellent agreement with the observed 938.272, 939.565, 139.570, and 134.977 MeV, respectively with 0.0006%, 0.01%, 0.02%, and 0.004%, respectively for the difference between the calculated and observed mass.

4.3. The Three Branes

The other three 10D string branes (negative energy weak-gravity brane, positive energy strong-gravity brane, and negative energy strong-gravity brane) did not absorb detachment space, but to synchronize the expansion of the positive-energy string brane (home universe), the other three 10D string branes undergo the oscillation between 10D and 4D.

4.3.1. The Hidden Three Branes from 10D to 5D

The three branes undergo the transformation from 10D to 5D.

$$\begin{aligned} &10\text{D4d} \to 9\text{D5d} \to 9\text{D4d} \to 8\text{D5d} \to 8\text{D4d} \to 7\text{D5d} \\ &\to 7\text{D4d} \to 6\text{D5d} \to 6\text{D4d} \to 5\text{D5d} \to 5\text{D4d} \end{aligned} \tag{43}$$

From Equation (21), under the VSLD transformation and the VSD transformation, the three branes expand through the increasing rest mass and the translation-fractionalization from 10D4d to 5D4d. To the 4D home universe, the three branes from 10D to 5D are hidden, because as Equation (13), particles with different space-time dimensions and different speeds of light are transparent and oblivious to one another to avoid the violation of causality due to differences in the speed of light. During this time, the home 4D universe expands normally.

4.3.2. The Three Branes as Dark Energy

When all three branes and the home universe become 4D, the three branes become dark energy as a part of the home universe.

$$4\text{D5d} \to 4\text{D4d} \tag{44}$$

The result is the accelerating expansion. Since the three branes have no detachment space to produce kinetic energy, dark energy is inert as the inert cosmological constant. According to the theoretical calculation based on the algebras cosmology, dark energy started in 4.47 billion years ago [19] in agreement with the observed 4.71 ± 0.98 billion years ago [52]. The maximum dark energy is 75% for the three out of the four regions as the spacetime of three branes becomes completely 4D.

4.3.3. The Three Hidden Branes from 5D to 10D

The three branes from 5D to 10D again become the hidden branes.

$$\begin{aligned} &5\text{D4d} \to 5\text{D5d} \to 6\text{D4d} \to 6\text{D5d} \to 7\text{D4d} \to 7\text{D5d} \\ &\to 8\text{D4d} \to 8\text{D5d} \to 9\text{D4d} \to 9\text{D5d} \to 10\text{D4d} \end{aligned} \tag{45}$$

They contract by the decreasing rest mass and the translation-condensation. The home universe contracts through gravity. Through symmetry, all four universes contract synchronically and equally.

4.3.4. The Three 10D Branes and the Original 4D Home Universe

Eventually, the three branes return to the original 10D three branes. The 4D home universe reaches cosmic deflation to lose all detachment space to become 10D4d. The four universes return to the step 3.

$$\begin{aligned} &\text{In the home universe} \\ &\text{4D home universe} \xrightarrow{\text{cosmic deflation}} \text{positive energy 10D4d weak gravity brane} \\ &\text{In the three branes} \\ &\text{9D5d branes} \longrightarrow \text{the 10D4d branes} \end{aligned} \tag{46}$$

The four branes can undergo another cycle of the home universe and the three branes or can reverse to the 11D membrane-antimembrane dual universes, and ultimately, to the zero-energy inter-universal void as shown in **Figure 6**.

5. Summary

In summary, the cyclic universe cosmology involves the split of the membrane

11D (11 dimensional) spacetime into the 1D eleventh dimension orbifold interval space to form gravity, the 6D discrete interior rishon space (TTT-VVV for positron-neutrino or TTV-TVV for u-$\bar{d}$ quarks) to form the Standard Model, the 3D Higgs space (attachment space to attach matter or detachment space to detach matter) to form the Higgs or reverse Higgs field, and 1D Einstein time to be shared by all spaces. The 1D eleventh dimension interval space was the space between the weak-gravity string brane and the strong-gravity string brane which are the progenitors of the home universe and dark energy, respectively.

The 6D discrete interior rishon space consists of the TTT-VVV or TTV-TVV as the discrete trivalent twisted strand braids for the spaces of positron-neutrino or u-$\bar{d}$ quarks, respectively, in the Rishon Space Model with 1/3 charge T and neutral V. The trivalent discrete rishon space is the interior space to determine the properties (flavor, charge, isospin, and color) of leptons and quarks, while the trivalent connected space is the exterior space to determine the momenta and positions of leptons and quarks.

The 3D Higgs space consists of attachment space as the space precursor of the transitional Higgs field and detachment space as the space precursor of the transitional reverse Higgs field. Attachment space that attaches matter to the space related to rest mass, detachment space that detaches matter from the space relates to kinetic energy. The combination of n units of attachment space (denoted as 1) and n units of detachment space (denoted as 0) produces binary partition space, $(1)_n(0)_n$, as the space of wave-particle duality, binary miscible space, $(1+0)_n$, as the space of relativity, and binary lattice space, $(1, 0)_n$, as the space of virtual gauge boson in quantum field theory. A particle with the rishon space is bound to the different Higgs spaces under different conditions. The Higgs space is the interior space to determine the properties (attachment and detachment to matter) of elementary particles, while the exterior space determines the momenta and positions of elementary particles.

Between 4D spacetime and 10D spacetime, dimension number decreases with decreasing speed of light, decreasing vacuum energy, and increasing rest mass. The 4D and the 10D have zero and the highest vacuum energies, respectively. Each spacetime dimension D associates with mass dimension d where D + d = 14.

This paper posits that the origin of the split is from the multiverse cosmology. The multiverse consists of the 4D zero-energy inter-universal void with detachment space and the multiple 11D positive-energy membrane and negative-energy anti-membrane dual universes with 11D attachment space. The total energy of a dual 11D universe is zero. Detachment space in the inter-universal void prevents the collision of the 11D dual universes, while attachment space in a dual universe allows the existence of mass-energy in the space of the dual universe. A dual universe with zero total energy can emerge from the zero-energy inter-universe.

The cyclic universe cosmology (**Figure 6**) in the multiverse starts with the zero-energy inter-universal void and the positive-energy membrane and nega-

tive-energy antimembrane 11D dual universe which is split into four equal 10D string branes, including the 10D positive-energy weak-gravity brane with matter, negative-energy strong-gravity brane, negative-energy weak-gravity brane with antimatter, and positive-energy strong-gravity brane in the 11D bulk. The 1D eleventh dimension interval space is between the strong and the weak-gravity branes as in Randall-Sundrum model.

To form the home universe where we inhabit, the 10D positive-energy weak-gravity brane with attachment space absorbed the zero-energy 4D inter-universal void with detachment space, resulting in the combination of rest mass from attachment space and kinetic energy from detachment space, the formation of the 4D spacetime universe by transforming 6D connected exterior space into 6D discrete interior rishon space to form the extended Standard Model, and cosmic inflation from high vacuum energy (10D) to zero vacuum energy (4D). The other three branes did not absorb the inter-universal void, resulting in the oscillating dimension branes between 10D and 4D stepwise without kinetic energy. The three branes are hidden when $D > 4$, and they are dark energy when $D = 4$. Afterward, when $D > 4$ again for the three branes, the home universe and the three branes start to contract, and eventually return to the original four 10D string branes and then to the original 11D membrane dual universe for the cyclic universe cosmology as in **Figure 6**.

Consequently, the emergences of gravity, the Standard Model, and dark energy as the three different phenomena take three steps. The Step 1 to form gravity involves the emergence of the 1D interval space to form gravity derived from the split of the 11D membrane universe into two branes with 1D interval space in between the two branes. The Step 2 to form the Standard Model involves the 6D rishon space to form the Standard Model derived from the addition of detachment space to the 10D weak-gravity brane to form the home universe consisting of the combination of attachment space and detachment space for the Higgs mechanism and the 4D spacetime with 6D TTTVVV or TTVTVV for the origin of elementary particles. The Step 3 to form dark energy involves the 4D strong-gravity brane to form dark energy derived from the dimensional oscillation between 10D and 4D. The 3-step cosmic evolution from the beginning of the cyclic universe to the present is as **Figure 9**.

All elementary particles for baryonic matter (leptons, quarks, gauge bosons, gravity, and the Higgs boson) and dark matter (sterile neutrinos) can be placed in the periodic table of elementary particles based on the two sets of the seven mass dimensions. The periodic table of elementary particles calculates accurately the particle masses of all leptons, quarks, gauge bosons, the Higgs boson, and the cosmic rays by using only five known constants: the number (seven) of the extra spatial dimensions in the observed four-dimensional spacetime from the eleven-dimensional membrane, the mass of electron, the masses of Z and W bosons, and the fine structure constant. The calculated masses are in excellent agreements with the observed masses. For examples, the calculated masses of muon, top quark, and the Higgs boson are 105.55 MeV, 175.4 GeV, and 126

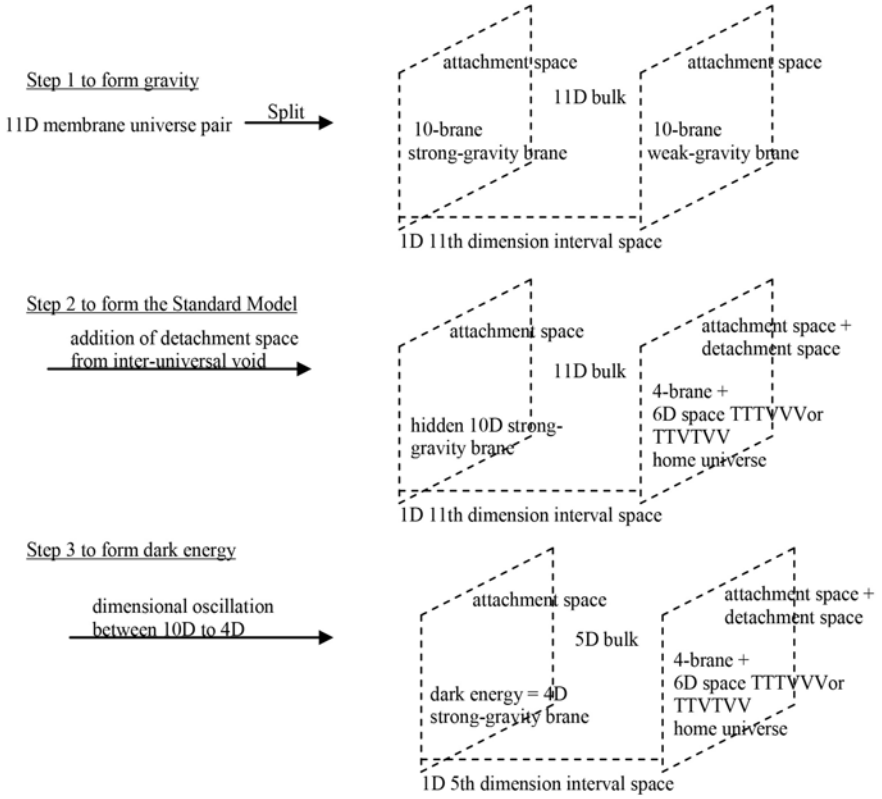

Figure 9. The 3-step cosmic evolution from the beginning to the present. Step1 to form gravity: split the 11D membrane universe into two branes with 1D interval space in between the two branes. Step 2 to form the Standard Model: the addition of detachment space to the 10D weak-gravity brane to form the home universe with the combination of attachment space and detachment space and the 6D rishon space. Step 3 to form dark energy: the conversion of the strong-gravity brane to the 4D dark energy by the dimensional oscillation between 10D and 4D from the strong-gravity brane.

GeV, respectively, in excellent agreements with the observed 105.65 MeV, 172.4 GeV, and 126 GeV, respectively. The calculated masses of hadrons based on the periodic table of elementary particles are in excellent agreement with the observed masses of hadrons. For examples, the calculated masses of proton, neutron, pion ($\pi^{\pm}$), and pion (π^{0}) are 938.261, 939.425, 139.540, and 134.982 MeV in excellent agreement with the observed 938.272, 939.565, 139.570, and 134.977 MeV, respectively with 0.0006%, 0.01%, 0.02%, and 0.004%, respectively for the difference between the calculated and observed mass. In conclusion, the split 11D spacetime, and cyclic universe cosmology, and the periodic table of elementary particles provide the matter-antimatter imbalance and the accurate calculated masses for leptons, quarks, hadrons, gauge bosons, the Higgs boson, gravity, dark matter, and dark energy

Conflicts of Interest

The author declares no conflicts of interest regarding the publication of this paper.

References

[1] Green, M., Schwarz, J. and Witten, E. (2012) Superstring Theory. Vol. 1: Introduction. Cambridge University Press, Cambridge.

[2] Woit, P. (2006) Not Even Wrong: The Failure of String Theory and the Search for Unity in Physical Law. Basic Books, New York.

[3] Randall, L. and Sundrum, R. (1999) *Physical Review Letters*, **83**, 4690-4693. https://doi.org/10.1103/PhysRevLett.83.4690

[4] Randall, L. (2005) Warped Passages: Unraveling the Mysteries of the Universe's Hidden Dimensions. Harper Collins, New York.

[5] Randall, L. and Sundrum, R. (1999) *Physical Review Letters*, **83**, 3370-3373. https://doi.org/10.1103/PhysRevLett.83.3370

[6] Pati, J. and Salam, A. (1974) *Physical Review D*, **10**, 275-289. https://doi.org/10.1103/PhysRevD.10.275

[7] Dugne, J., Fredriksson, S. and Hansson, J. (2002) *Europhysics Letters*, **57**, 188-194. https://doi.org/10.1209/epl/i2002-00337-8

[8] Harari, H. (1979) *Physics Letters B*, **86**, 83-86. https://doi.org/10.1016/0370-2693(79)90626-9

[9] Shupe, M. (1979) *Physics Letters B*, **86**, 87-92. https://doi.org/10.1016/0370-2693(79)90627-0

[10] Harari, H. and Seiberg, N. (1982) *Nuclear Physics B*, **204**, 141-167. https://doi.org/10.1016/0550-3213(82)90426-6

[11] Brodsky, S. and Drell, S. (1980) *Physical Review D*, **22**, 2236-2243. https://doi.org/10.1103/PhysRevD.22.2236

[12] Bilson-Thompson, S. (2005) A Topological Model of Composite Preons.

[13] Bilson-Thompson, S., Hackett, J., Kauffman, L. and Wan, Y. (2012) *Symmetry, Integrability and Geometry: Methods and Applications*, **8**, 14. https://doi.org/10.3842/SIGMA.2012.014

[14] Barut, A. and Chung, D. (1983) *Lettere al Nuovo Cimento*, **38**, 225-226. https://doi.org/10.1007/BF02814632

[15] Weinberg, S. (1989) *Review Modern Physics*, **61**, 1-23. https://doi.org/10.1103/RevModPhys.61.1

[16] Chung, D. (2016) *Journal of Modern Physics*, **7**, 1210-1227. https://doi.org/10.4236/jmp.2016.710110

[17] Hansson, J. (2015) *International Journal of Modern Physics and Applications*, **1**, 12-16.

[18] Jammer, M. (2009) Concepts of Mass in Contemporary Physics and Philosophy. Princeton University Press, Princeton. https://doi.org/10.1515/9781400823789

[19] Chung, D. and Krasnoholovets, V. (2013) *Journal of Modern Physics*, **4**, 77-84. https://doi.org/10.4236/jmp.2013.47A1009

[20] Chung, D. (2018) *Journal of Modern Physics*, **9**, 2257-2273. https://doi.org/10.4236/jmp.2018.913142

[21] Chung, D. (2018) *Journal of Modern Physics*, **9**, 2308-2319. https://doi.org/10.4236/jmp.2018.913146

[22] Chung, D. (2018) *Journal of Modern Physics*, **9**, 2638-2656. https://doi.org/10.4236/jmp.2018.914164

[23] Gorham, P., *et al.* (2016) *Physical Review Letters*, **117**, Article ID: 071101.

[24] Gorham, P., *et al.* (2018) *Physical Review Letters*, **121**, Article ID: 161102.

[25] Gorham, P., *et al.* (2009) *Astroparticle Physics*, **32**, 10-41.

[26] Penrose, R. (2000) Wavefunction Collapse as a Real Gravitational Effect. In: Fokas, A., Grigoryan, A., Kibble, T. and Zegarlinski, B., Eds., *Mathematical Physics*, Imperial College, London, 266-282. https://doi.org/10.1142/9781848160224_0013

[27] Moffat, J. (1993) *International Journal of Modern Physics D*, **2**, 351-359. https://doi.org/10.1142/S0218271893000246

[28] Albrecht, A. and Magueijo (1999) *Physics Review D*, **59**, Article ID: 043516. https://doi.org/10.1103/PhysRevD.59.043516

[29] Barrow, J. (2003) *Physics Letters B*, **564**, 1-7. https://doi.org/10.1016/S0370-2693(03)00573-2

[30] Bounias, M. and Krasnoholovets, V. (2003) *The International Journal of Systems and Cybernetics*, **32**, 1005-1020. https://doi.org/10.1108/03684920310483144

[31] Jarosik, N., *et al.* (2011) *The Astrophysical Journal Supplement Series*, **192**, 14. https://doi.org/10.1088/0067-0049/192/2/14

[32] Fujita, J. and Miyazawa, H. (1957) *Progress of Theoretical Physics*, **17**, 360. https://doi.org/10.1143/PTP.17.360

[33] Chung, D. (2016) *Journal of Modern Physics*, **7**, 1150-1159. https://doi.org/10.4236/jmp.2016.710104

[34] Tsui, D., Stormer, H. and Gossard, A. (1982) *Physical Review Letters*, **48**, 1559-1562. https://doi.org/10.1103/PhysRevLett.48.1559

[35] Stormer, H. (1999) *Reviews of Modern Physics*, **71**, 875-889. https://doi.org/10.1103/RevModPhys.71.875

[36] Laughlin, R. (1983) *Physical Review Letters*, **50**, 1395-1398. https://doi.org/10.1103/PhysRevLett.50.1395

[37] Loureiro, A., *et al.* (2019) *Physical Review Letters*, **123**, Article ID: 081301. https://doi.org/10.1103/PhysRevLett.123.081301

[38] Chung, D. (2015) *Global Journal of Science Frontier Research A*, **15**, 119-125.

[39] Moffat, J. (2006) *Journal of Cosmology and Astroparticle Physics*, **3**, 4. https://doi.org/10.1088/1475-7516/2006/03/004

[40] Moffat, J. (2008) Reinventing Gravity. HarperCollins, New York.

[41] Chung, D. (2014) *International Journal of Astronomy and Astrophysics*, **4**, 374-383. https://doi.org/10.4236/ijaa.2014.42032

[42] Kamilla, R., Wu, X. and, Jain, J. (1996) *Physics Review Letters*, **76**, 1332. https://doi.org/10.1103/PhysRevLett.76.1332

[43] Jain, J. (2007) Composite Fermions. Cambridge University Press, New York.

[44] Particle Data Group (2018) *Physical Review D*, **98**, Article ID: 030001. https://doi.org/10.1103/PhysRevD.98.030001

[45] Barut, A. (1979) *Physical Review Letters*, **42**, 1251. https://doi.org/10.1103/PhysRevLett.42.1251

[46] Krasznahorkay, A., *et al.* (2016) *Physical Review Letters*, **116**, Article ID: 042501. https://doi.org/10.1103/PhysRevLett.116.042501

[47] Feng, J., *et al.* (2016) *Physical Review Letters*, **117**, Article ID: 071803. https://doi.org/10.1103/PhysRevLett.117.071803

[48] De Rujula, A., Georgi, H. and Glashow, S. (1975) *Physics Review D*, **12**, 147-162. https://doi.org/10.1103/PhysRevD.12.147

[49] Griffiths, D. (2008) Introduction to Elementary Particles. Wiley-VCH, Weinheim.

[50] El Naschie, M. (2002) *Chaos, Solitons and Fractals*, **14**, 369-376. https://doi.org/10.1016/S0960-0779(02)00022-X

[51] Chung, D. (2016) *Journal of Modern Physics*, **7**, 1591-1606. https://doi.org/10.4236/jmp.2016.712144

[52] Riess, A.G., *et al.* (2004) *Astrophysical Journal*, **607**, 665-687. https://doi.org/10.1086/383612

Journal of Modern Physics, 2019, 10, 1342-1352
https://www.scirp.org/journal/jmp
ISSN Online: 2153-120X
ISSN Print: 2153-1196

Microscale Crystalline Rare-Earth Doped Resonators for Strain-Coupled Optomechanics

Jean-François Motte[1], Nicolas Galland[1], Jérôme Debray[1], Alban Ferrier[2,3], Philippe Goldner[2], Nemenja Lučić[4], Shuo Zhang[4], Bess Fang[4], Yann Le Coq[4], Signe Seidelin[1,5]

[1]Université Grenoble Alpes, CNRS, Grenoble INP and Institut Néel, Grenoble, France
[2]PSL Research University, Chimie Paris Tech, CNRS, Institut de Recherche de Chimie Paris, Paris, France
[3]Sorbonne Universités, UPMC Université Paris 06, Paris, France
[4]LNE-SYRTE, Observatoire de Paris, Université PSL, CNRS, Sorbonne Université, Paris, France
[5]Institut Universitaire de France, Paris, France
Email: signe.seidelin@neel.cnrs.fr

How to cite this paper: Motte, J.-F., Galland, N., Debray, J., Ferrier, A., Goldner, P., Lučić, N., Zhang, S., Fang, B., Le Coq, Y. and Seidelin, S. (2019) Microscale Crystalline Rare-Earth Doped Resonators for Strain-Coupled Optomechanics. *Journal of Modern Physics*, **10**, 1342-1352.
https://doi.org/10.4236/jmp.2019.1011088

Received: August 2, 2019
Accepted: October 9, 2019
Published: October 12, 2019

Copyright © 2019 by author(s) and Scientific Research Publishing Inc.
This work is licensed under the Creative Commons Attribution International License (CC BY 4.0).
http://creativecommons.org/licenses/by/4.0/
Open Access

Abstract

Rare-earth ion doped crystals for hybrid quantum technologies are an area of growing interest in the solid-state physics community. We have earlier theoretically proposed a hybrid scheme of a mechanical resonator which is fabricated out of a rare-earth doped mono-crystalline structure. The rare-earth ion dopants have absorption energies which are sensitive to crystal strain, and it is thus possible to couple the ions to the bending motion of the crystal cantilever. This type of resonator can be useful for either investigating the laws of quantum physics with material objects or for applications such as sensitive force-sensors. Here, we present the design and fabrication method based on focused-ion-beam etching techniques which we have successfully employed in order to create such microscale resonators, as well as the design of the environment which will allow studying the quantum behavior of the resonators.

Keywords

Rare-Earth Doped Crystals, Mechanical Resonators, Optomechanics, Quantum Physics, Strain-Coupling, Spectral Hole Burning, Focused-Ion-Beam Etching Techniques

1. Introduction

The study of mechanical resonators coupled to light belongs to the field of optomechanics [1], which emerged experimentally about a decade ago, when several groups started to investigate the techniques required to actively cool a macroscopic mechanical oscillator down to its quantum ground state. The combi-

nation of active and traditional cryogenic cooling techniques was intensively pursued and allowed in 2011 for the very first time to place a mechanical system in its quantum ground state [2] [3]. One way to study the resonators in or close to the quantum ground state, is to couple it to a two-level system, and interact with the resonator via this system. One particularly interesting way to achieve this is to use "strain-coupling", first demonstrated in 2014 with a semi-conductor nanowire [4]. In such a resonator, the vibrations, which can be induced deliberately by means of a piezo actuator or result from the Brownian motion due to a finite temperature (or even from the zero-point energy position fluctuations), generate a mechanical strain, as illustrated in **Figure 1**. This strain influences the electronic properties of the impurity, as a consequence of the modification of the electronic orbital distributions, and thus the energy levels of the impurities. The oscillations of the crystal are therefore mapped onto the energy levels of the impurity, which in turn gives rise to a change in the optical frequency of the photons absorbed and emitted. The corresponding strain mediated coupling strength can be higher, and is potentially more stable, than what can be achieved with any realistic external forces (such as magnetic gradient forces [5]). What is particularly appealing about these integrated hybrid mechanical systems is that some of them may approach or even enter the strong coupling regime [6]. In this regime, the hybrid coupling strength exceeds the decoherence rates of both the mechanical resonator and the impurity (which, according to context, is the decoherence rate of either an electronic transition or a transition between spin states).

This strain-coupling can also be exploited in a rare-earth ion doped crystal resonator, which is particularly interesting due to the exceptional coherence properties of the rare-earth ion dopants. We suggested a theoretical protocol for

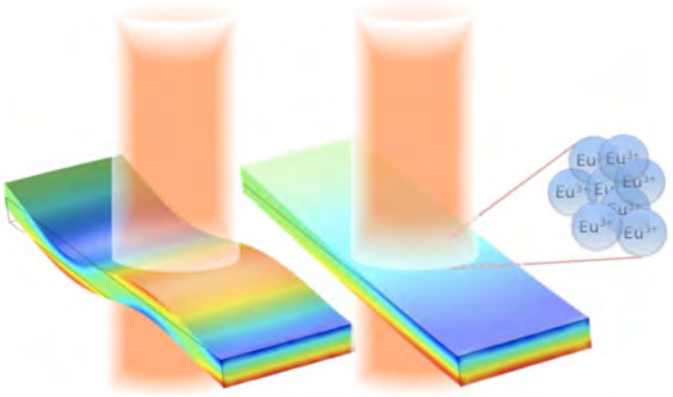

Figure 1. When a mechanical resonator vibrates, the strain inside the material is periodically modulated. In this example, the color range from blue (compression) over green (non-strained) to red (extension) of the material is obtained from a COMSOL simulation. The anchoring point (not shown) of the resonators is in foreground of the drawing (toward the reader). To the right, the resonator oscillates in the first excited mode whereas to the left, a higher order excited mode is shown.

creating and operating such a strain-coupled system [7]and for cooling the resonator down to the near the quantum groundstate [8]. In the following, we will discuss how to design the physical system allowing performing such experiments, with particular attention given to the fabrication of the microscale resonators.

2. Preliminary Theoretical Considerations

In order to develop a resonator design based on Eu^{3+} doped Y_2SiO_5 for studying strain-coupled optomechanics, several challenges must be faced. First, the atomic structure makes it very challenging to observe single ions [9] due to the narrow absorption linewidth, weak oscillator strength, and the fact that there are often no closed transitions [10]. We therefore decided to investigate the possibility of using not single ions, but spectral holes imprinted in the structure to which couple the mechanical motion. This is indeed possible, but the fact that an ensemble of ions is involved, adds an inhomogeneous broadening of the lineshape (and not just a linear shift) due to the strain arising from vibrations [7]. In other words, the spectral hole broadens under applied strain. In order to overcome this challenge, our protocol is based on a dispersive coupling between the edge of a spectral hole and a detuned laser. More precisely, when the resonator vibrates, the slope of the edge of the spectral hole will oscillate periodically. The coupling can be read-out by observing a phase shift of a laser traversing the resonator. The details of the coupling mechanism are given in Ref. [7], including a protocol for "functionalizing" the spectral hole in order to enhance the coupling.

Parameters Obtained from Simulations

One of the practical consequences of coupling to an ensemble of ions is that laser needs to interact with a large number of ions, making a micrometre scale resonator more suitable than a nanoscale one, at least for the initial experiments during which the detection efficiency has not yet been fully optimized. For the first prototypes, based on the simulations, we therefore opted for the following parameters: a single-clamped cantilever with the dimensions $100 \times 10 \times 10\ \mu m^3$ interacting with a laser beam traversing the cantilever near its fixed end (anchoring point) for maximum strain. The cantilever which consists of Y_2SiO_5 (which has a Young Modulus of 135 GP) with an effective mass of 1.1×10^{-11} kg, and of which the first excited mechanical mode vibrates at 890 kHz (value obtained from COMSOL simulations). The cantilever contains a 0.1% doping of Eu^{3+} ions, with a $^7F_0 \rightarrow {}^5D_0$ transition centered at 580 nm and potentially with a linewidth as low as $\Gamma = 2\pi \times 122$ Hz (at T = 1.4 K and 10 mT magnetic field [10]). For our simulations, we used a power of 1 mW and a hole width of 6 MHz. In this configuration, the static displacement of the tip of the resonator due to the light field amounts to 0.4 pm and the corresponding phase shift of the laser (the carrier) equals 0.2 mrad. This shift is easily observable as, for the 1 mW laser power, the shot noise limited phase resolution is 0.45 microradian within the allowed detection time, before "hole-overburning" becomes

non-negligible (approximately 16 ms for the 122 Hz linewidth). For comparison, a direct reflection of a 1 mW laser on the resonator (creating a force on the resonator due to the momentum delivered by the photons) would give rise to a much smaller static displacement (20 fm), justifying the efficiency of this dispersive approach.

Calculations performed in Ref. [7] also showed that the amplitude of the Brownian motion at 3 K is 0.2 pm, and the spectral sidebands of the detection laser contain an integrated phase of 0.11 mrad due to this thermal excitation. For an integration time equal to the inverse of the thermal line width (25 microseconds), the shot-noise limited phase-resolution is 14 microradian. The thermally excited sidebands are therefore readily observed, even within such short integration time. Moreover, by increasing the integration time up to the maximum before over-burning, it is possible to observe and measure accurately the detailed shape and size of the sidebands. Zero-point motion of the resonator, averaged over the measurement, induces a small excess integrated phase of 0.4 microradian in the sidebands. As this value is close to the phase resolution achieved within the maximum integration time before hole-over burning, the shot noise limited resolution is therefore sufficient to observe the effect of the zero-point motion of the mechanical resonator. By using either dilution fridge or an active laser cooling mechanism (or a combination of these), the temperature can be lowered near a point where the thermal excitation does not hide the effect of zero point fluctuations. For example, at 30 mK, the zero-point fluctuation induces approximately 10^{-3} relative excess integrated phase over the effect of Brownian fluctuations alone. Such a deviation seems measurable, provided sufficient knowledge of the relevant parameters (temperature, Q factor,...). Several measurements at different temperatures may also be used to estimate the various relevant parameters with the necessary accuracy. Note that the resolution can be further increased by repeating the full hole imprinting and measurement sequence several times, or use optical repumpers to preserve the spectral hole [11]. As the current setup is based on a 3 Kelvin cryostat, the zero-point motion measurement is not immediately feasible, but we have here included the numbers as this is one of the next major modifications.

A potentially perturbing effect arises due to fluctuations of the laser power. As the static displacement corresponding to 1 mW of laser power is approximately 0.4 pm, this laser power must be stable to within 10^{-4} to ensure a perturbation much smaller than the zero point fluctuations (approx. 1 fm), a power stability requirement well within reach of standard stabilization techniques. In addition, the laser frequency must also be carefully controlled. The zero-point motion induces a frequency shift of the ions closest to the edge of the resonator of approximately 37 Hz. The probe laser must therefore have a frequency stability substantially better than that, which is well within reach of nowadays commercially available ultra-high finesse Fabry-Perot cavity stabilized lasers (which typically have sub-Hz frequency stability). Note that probing the Brownian motion

alone at 3 K exhibits a much less stringent frequency stability requirement at the sub-kHz level, and this will be one of the first measurements we plan to perform using the resonators. In order to anticipate the zero-point motion measurement, a new commercial ultrastable cavity (Stable Lasers) has recently been integrated in the setup, see Section 4 below.

3. Microfabrication of Resonators

In this section, we will discuss the fabrication of the resonators, of which the design is based on the above considerations. The bulk crystals are grown at the Paris Institute for Chemical Research (Institut de Recherche de Chimie Paris), and the microfabrication of the resonators in a cleanroom facility in Grenoble (Nanofab Institut NEEL).

3.1. Growing of the Bulk Crystals

A single Y_2SiO_5 crystal of 0.1 percent at Eu^{3+} (Eu:YSO) was grown using a homemade RF induction Czochralski apparatus using Ir crucible to contain the melt and ZrO_2 and Al_2O_3 as refractory materials. The growth of the single crystal was performed under flowed nitrogen introduced as a protective atmosphere. During the growth the shape of the crystal is controlled with a feedback loop on the RF generator power by monitoring the weight of the crystal. The crystal was pulled at 0.5 mm/h from the melt in the [010] direction, which minimizes the defects due to the anisotropy of the expansion coefficients. The resulting one-inch diameter single crystal is transparent, colorless with a regular shape. The crystal is then oriented by the Laue method with an accuracy of ±2 degrees. Finally, the samples were polished with a Logitech PM5. More details on the fabrication of the bulk crystals can be found in Ref. [12].

3.2. Fabrication of Microresonators

The bulk crystal samples have dimensions of the order of millimeters. In order to reach quantum regimes, resonators with micro- and nanoscale dimensions are required. These designs can be realized by subsequently using Focused Ion Beam (FIB) techniques to shape the crystal. Etching a Y_2SiO_5 crystal using FIB techniques is challenging, as the crystal is an oxide and thus not conducting, leading to rather low etching rates. The literature on the subject is sparse, and a major effort has been required in order to calibrate the procedure and achieve a good etching efficiency. We will in the following outline the essential steps and parameters.

We use a FIB-SEM system (*Zeiss NVision*) with a gallium liquid ion source. Due to the absence of conductivity of the Y_2SiO_5 it is necessary to first deposit a thin (100 - 150 nm) metal layer (aluminium) on the crystal prior to etching the structures. This layer prevents the charges from building up, which otherwise would cause the ion-beam to be deviated from the desired target. Due to the hardness of the crystal, a rather high voltage is required to etch the structures,

and we operate the gallium ion source at 30 kV (maximum voltage). At this voltage amorphizing of the material can happen, but due to the nature and hardness of the crystal, this turns out not to be an issue for our samples. The current used is approximately 6 nA. We obtain an etching rate of the order of 1 μm^3/nA/s.

Once the calibration completed, we turn to the fabrication of the resonators. The major challenge is to etch deep enough into the material in order to detach the resonator from below (we wish to obtain a free-standing resonator, only attached to the crystal at one anchoring point). This requires a large angle of the incoming gallium ion beam, and the ability to remove a large amount of material. As the etching rate is slow, and the extent of orientation of the sample relative to the ion beam is limited, this way of proceeding turns out not to be ideal.

Figure 2(a) shows an example of a resonator of which the contour lines have been easily etched, but illustrates the difficulty of liberating the resonator from below. In addition to the difficulty of removing material and obtaining the right angle for the gallium ion beam, etching deep trenches are also problematic due to the fact that the metal layer (deposited for removal of accumulated charges) becomes spatially further and further separated from the part of the structure to be etched. By modifying the angle of the gallium ion beam, we managed to liberate most of the resonator from the substrate (see **Figure 2(b)**), but the exerted force of the gallium beam and built-up residual charges distort the shape of the resonator, and when proceeding to liberate the resonator near its anchoring point, it breaks off, as illustrated in **Figure 2(c)**.

A solution which circumvents the need for etching below the resonator, consists in creating the resonator on the edge of a corner the crystal, and this is the technique that has turned out to be the most successful, as it requires the minimal etching of material. Moreover, by turning the crystal 90 degrees the ion-beam can be perpendicular to the crystal at all times. This has been carried out on the crystal shown in **Figure 3(a)**. We have etched a part of the bulk crystal at an angle of 45 degrees below the resonator. By coating this surface with aluminum, we have realized a mirror which allows a laser beam to be reflected onto it and pass through the resonator alone, without interacting with the bulk material of the crystal. We have chosen to position the mirror below the part of the resonator which is nearest the anchoring point in order to maximize the material strain, for an optimum coupling.

An alternative option consists in polishing the edge of the crystal down to obtain a very thin layer prior to applying the FIB. As shown in the example in **Figure 3(b)**, the crystal has been polished to an angle of 3.2 (±0.1) degrees (measured with a DEKTAK profilometer and a calibrated microscope). This allows one to create the resonator by applying the FIB perpendicular to the surface of the crystal along a single direction. This has the advantage of allowing the laser beam to pass directly through the resonator in a straight line, without having to integrate a mirror to deviate the beam to avoid the bulk part of the crystal. Moreover, it also represents the advantage of not having to use the FIB on the top and bottom surface of the resonator, and thus conserve the initially polished

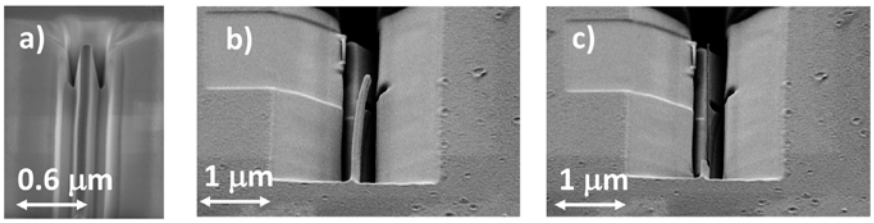

Figure 2. In (a) we show the resonator etched on the sides, but not liberated from below. In (b) and (c) we have increased the angle of the gallium ion beam, which allows to etch below the structure. In (c) the resonator breaks during an attempt to liberate it from below. In all 3 images, the voltage used for SEM imaging is 2.00 kV.

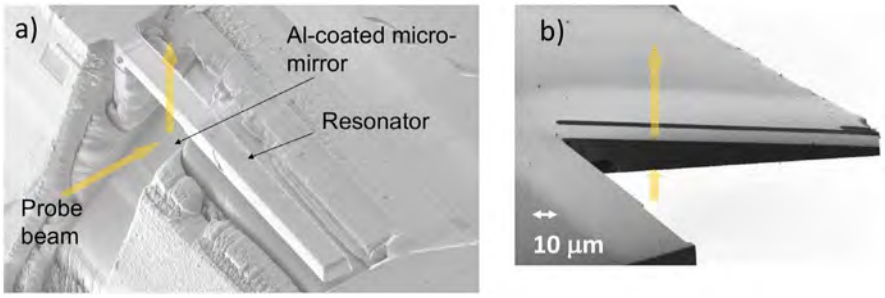

Figure 3. In (a) we show the SEM image of the resonator etched on the corner of the crystal. A mirror at an angle of 45 degrees is integrated in order to make the laser beam traverse only the resonator and thus avoiding the bulk part of the crystal. In (b) the edge of the crystal have been polished so thin that the resonator is formed by a single vertical cut with the FIB. The scale indicated in (b) applies to both images.

surfaces. In that way, we also avoid surface effects of the FIB due a non-desired implementation of the gallium ions, although this has been shown not to represent major degradation of the coherence properties of other species of rare-earth ions in the YSO matrix [13]. If however, the triangular shape of the resonator turns out to be a limiting factor (as it increases the resonator's stiffness) it is also possible to reshape it into a rectangular form using the FIB, by removing a much smaller amount of material than when starting out from the bulk crystal.

In both resonators, the crystal has been oriented such that the laser beam is parallel to the crystal b-axis (corresponding the [010] growth axis of the crystal) which optimizes the absorption of the Eu^{3+} ions for the crystal site 1 (there exists 2 non-equivalent crystal site for the ions). The polarization of the laser beam is roughly along the D1 direction, but is fine-tuned manually by maximizing the absorption of the europium ions [14].

4. Optics Environment

The optical system which will be used to probe the europium ions inside the resonators is based on an extended cavity diode laser at 1160 nm (Toptica DLPro), delivering 65 mW. It is coupled and frequency doubled in PPLN waveguides with free space outputs to reach 580 nm, corresponding to the wavelength of

absorption of the $^7F_0$-$^5D_0$ transition in Eu^{3+}:Y_2SiO_5. The laser at 1160 nm is frequency locked by the Pound-Drever-Hall method to a commercial reference cavity (Stable Laser Systems). Both the diode laser current and a piezo actuator acting on the external cavity length are used for feedback, with a bandwidth around 500 kHz. After the optical frequency doublers, approximately 10 mW of 580 nm light is obtained. Details on the laser system can be found in Ref. [15].

Optics Mount for Studying the Resonator

We present our setup for focusing a laser beam onto the micrometric resonator, taking into account the constraints of the cryogenic environment. Our cryostat (OptiDry200 from MyCryoFirm) has a fairly large (approximately 35 cm in external diameter) vacuum chamber, with a hermetically sealed inner vacuum chamber to allow for the possibility of cold buffer gas at around 4 K. Together with a thermal shield at 50 K, there are in total three view ports (fused silica of varying thickness between 4 to 10 mm) in series between the outer wall and the sample holder where the resonator will be installed. In order to minimize aberrations, it is preferable to propagate a collimated laser beam through these windows and focus down to a spot of <5 μm (RMS spot size) near the resonator, the width of which is 10 μm. The beam after passing through the resonator will thus be highly diverging, and will be collimated again in the cryostat before exiting and reaching the detection optics. In addition, an afocal telescope of unit magnification (Thorlabs LA1131A, f = 50 mm) is placed before the cryostat to allow for potential fine adjustment of the collimation.

We simulate using OSLO (ray tracing software from Lambda Research Corporation) the RMS spot size of a Gaussian beam ($1/e^2$ radius of 2.75 mm) and its ensquared energy within a square of 10 μm × 10 μm at the position of the resonator. We also consider a defocus of ±5 μm to account for the thickness of the resonator). In an ideal situation, *i.e.* the resonator (10 μm × 10 μm in cross section) is placed exactly at the focal point of lenses C, Thorlabs asphere C280TMD-A, f = 18.4 mm, the RMS spot size of the laser beam remains below 2 μm, to be compared with a diffraction limited Airy radius 2.9 μm. The total ensquared energy is more than 93% for distance of ±5 μm from the focal point. In other words, there will be little stray light elsewhere that may contribute to a background noise.

A first optomechanical mount has been realised for the resonator (which is depicted in **Figure 3(a)**), containing the lenses C and D. The geometry of this resonator requires an additional mirror (Thorlabs prism MRA05-E02) at 45˚ to deflect the outgoing laser beam in order to use the view ports in a straight through configuration. For this purpose, the optical axes of the focusing (C) and collimating (D) lenses are displaced. Besides the focal position of the lenses, there is no adjustment available once the resonator is fixed. We modify our simulation to investigate the effect of 1) a possible defocus (from longitudinal positioning and thermal contraction of the mount during the cooling cycle), and 2) a transverse displacement (mainly due to finite positioning accuracy).

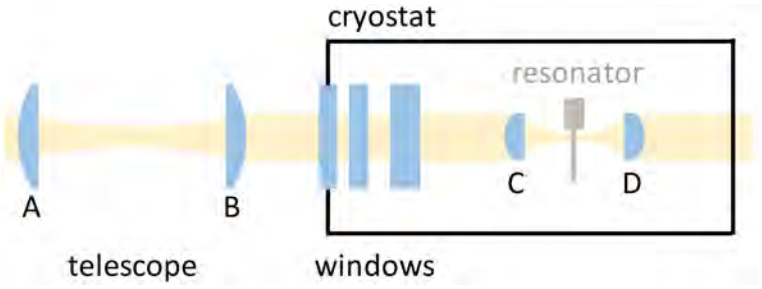

Figure 4. A schematic of the optical set up: an afocal telescope (lenses A and B) of unit magnification, the 3 windows of the cryostat, the focusing lens (lens C), the resonator, and the collimating lens (lens D). Lens B is allowed to move in the following simulations to compensate for any possible defocus. Note that the detailed structure of the cryostat, the exit view ports, and the detection optics are not represented in this figure.

Given that the integrated fractional thermal contraction of copper from room temperature down to 4 K is about 3×10^{-3}, a lens-resonator distance (longitudinal) on the order of 20 mm would vary about 60 microns. We verify that the afocal telescope can conveniently accommodate a defocus of ±100 μm on axis. Typically, a defocus of 10 μm requires to adjust the position of lens B by about hundreds of microns, easily achievable with a manual translation stage possessing a 5 mm course. After compensation, the RMS spot size remains below 2 μm and the ensquared energy is above 90%.

We also consider a transverse positioning error of ±50 μm, both at the best focus and with a defocus of ±100 μm but compensated by repositioning lens B as described in the previous paragraph. In the worst case, i.e. at the maximal transverse positioning error and defocus = −100 μm, the RMS spot size remains about 2 μm and the ensquared energy is above 80%.

The planned optical setup (see **Figure 4**) is therefore simple, robust and promising for our future experiments, as it can focus most of the light down to a size compatible with the microresonator and is able to accommodate ±100 μm of longitudinal position error and ±50 μm of transverse position error. It will require a pre-alignment at room temperature and pressure prior to its installation in the cryostat. We are confident that the thermal effects of the cooling cycle should not prevent us from obtaining the desired signal from the resonator.

5. Conclusion and Outlook

In this article, we have motivated why rare-earth doped materials in shapes of resonators might hold promise for quantum optomechanics experiments. We have provided a description, including the most essential physical parameters, allowing one to successfully fabricate such resonators. We have also briefly described the experimental environment including optics and cryogenic setup which meet the requirements for studying the resonators near the quantum regime. We are currently able to observe the desired spectral features in bulk crystals, with a signal to noise level sufficiently high to potentially be able to observe

similar signals in the microresonators, which constitutes our next step. Once this achieved, by exciting the resonator with a piezo drive, it should be straightforward to observe the strain-coupling between resonator and europium ions in the classical regime, before proceeding to apply the cooling protocol described in Ref. [8] allowing reaching the quantum ground state.

Acknowledgements

YLC acknowledges support from the Ville de Paris Emergence Program and from the LABEX Cluster of Excellence FIRST-TF (ANR-10-LABX-48-01), within the Program "investissements d'Avenir" operated by the French National Research Agency (ANR). The project has also received funding from the European Union' Horizon 2020 research and innovation program under grant agreement No 712721 (NanOQTech).

Conflicts of Interest

The authors declare no conflicts of interest regarding the publication of this paper.

References

[1] Aspelmeyer, M., Meystre, P. and Schwab, K. (2012) *Quantum Optomechanics*, *Physics Today*, **65**, 29. https://doi.org/10.1063/PT.3.1640

[2] Chan, J., Mayer Alegre, T.P., Safavi-Naeini, A.H., Hill, J.T., Krause, A., Grblacher, S., Aspelmeyer, M. and Painter, O. (2011) *Nature*, **478**, 89. https://doi.org/10.1038/nature10461

[3] Teufel, J.D., Donner, T., Li, D., Harlow, J.H., Allman, M.S., Cicak, K., Sirois, A.J., Whittaker, J.D., Lehnert, K.W. and Simmonds, R.W. (2011) *Nature*, **475**, 359-363. https://doi.org/10.1038/nature10261

[4] Yeo, I., de Assis, P.L., Gloppe, A., Dupont-Ferrier, E., Verlot, P., Malik, N.S., Dupuy, E., Claudon, J., Grard, J.M., Auffives, A., Nogues, G., Seidelin, S., Poizat, J.-P., Arcizet, O. and Richard, M. (2014) *Nature Nanotechnology*, **9**, 106. https://doi.org/10.1038/nnano.2013.274

[5] Arcizet, O., Jacques, V., Siria, A., Poncharal, P., Vincent, P. and Seidelin, S. (2011) *Nature Physics*, **7**, 879-883. https://doi.org/10.1038/nphys2070

[6] Dalibard, J., Raimond, J.M. and Justin, J.Z. (1992) Fundamental Systems in Quantum Optics. Chap. Cavity Quantum Electrodynamics, les Houches session LIII. Elsevier Science Publishers, Amsterdam.

[7] Mø lmer, K., Le Coq, Y. and Seidelin, S. (2016) *Physical Review A*, **94**, Article ID: 053804. https://doi.org/10.1103/PhysRevA.94.053804

[8] Seidelin, S., Le Coq, Y. and Mø lmer, K. (2019) *Physical Review A*, **100**, Article ID: 013828. https://doi.org/10.1103/PhysRevA.100.013828

[9] Casabone, B., Benedikter, J., Hmmer, T., Oehl, F., de O. Lima, K., Hansch, T.W., Ferrier, A., Goldner, P., de Riedmatten, H. and Hunger, D. (2018) *New Journal of Physics*, **20**, Article ID: 095006. https://doi.org/10.1088/1367-2630/aadf68

[10] Equall, R.W., Sun, Y., Cone, R.L. and Macfarlane, R.M. (1994) *Physical Review Letters*, **72**, 2179-2182. https://doi.org/10.1103/PhysRevLett.72.2179

[11] Cook, S., Rosenband, T. and Leibrandt, D.R. (2015) *Physical Review Letters*, **114**, Article ID: 253902. https://doi.org/10.1103/PhysRevLett.114.253902

[12] Ferrier, A., Tumino, B. and Goldner, P. (2016) *Journal of Luminescence*, **170**, 406-410. https://doi.org/10.1016/j.jlumin.2015.07.026

[13] Zhong, T., Kindem, J.M., Miyazono, E. and Faraon, A. (2015) *Nature Communications*, **6**, 8206. https://doi.org/10.1038/ncomms9206

[14] Traum, C., Inacio, P.L., Félix, C., Segonds, P., Peña, A., Debray, J., Boulanger, B., Petit, Y., Rytz, D., Montemezzani, G., Goldner, P. and Ferrier, A. (2014) *Optical Materials Express*, **4**, 57-62. https://doi.org/10.1364/OME.4.000057

[15] Gobron, O., Jung, K., Galland, N., Predehl, K., Le Targat, R., Ferrier, A., Goldner, P., Seidelin, S. and Le Coq, Y. (2017) *Optics Express*, **25**, 15539-15548. https://doi.org/10.1364/OE.25.015539

Journal of Modern Physics, 2019, 10, 1353-1363
https://www.scirp.org/journal/jmp
ISSN Online: 2153-120X
ISSN Print: 2153-1196

Simulation of an Antimatter Beam Core Engine for Space Travel

Matthew Dubiel, Ryan J. Hooper

Department of Physics, Lewis University, Romeoville, Illinois, USA
Email: matthewdubiel@lewisu.edu

How to cite this paper: Dubiel, M. and Hooper, R.J. (2019) Simulation of an Antimatter Beam Core Engine for Space Travel. *Journal of Modern Physics*, **10**, 1353-1363.
https://doi.org/10.4236/jmp.2019.1011089

Received: September 2, 2019
Accepted: October 13, 2019
Published: October 16, 2019

Copyright © 2019 by author(s) and Scientific Research Publishing Inc.
This work is licensed under the Creative Commons Attribution International License (CC BY 4.0).
http://creativecommons.org/licenses/by/4.0/
Open Access

Abstract

An exciting prospect is the use of antimatter as a fuel source due to its ability to convert mass energy to kinetic energy. Upon annihilation of antimatter with matter, tremendous amounts of energy are carried away by charged and neutral particles. By redirecting the charged particles through an exhaust using a non-uniform magnetic field, an impulse can be generated capable of supplying thrust to an engine. Using the Geant 4 simulation toolkit developed by CERN, we simulate this process using a beam core engine design. By analyzing charged pions that result from antiproton-proton annihilation, we optimize the engine parameters and derive a specific impulse for antiproton fuel as used in the beam core configuration. A specific impulse of $(2.49 \pm 0.08) \times 10^6$ s was determined. This value is significantly higher than specific impulses of current chemical rocket fuels which range from 240 - 400 s.

Keywords

Antimatter, Antiproton Annihilation, Space Travel, Geant4

1. Introduction

Ever since its proposed existence in 1922, antimatter has held a fascinating place in both the sciences and science fiction. Antimatter's potential to liberate massive amounts of energy has made it an interesting prospect as a fuel source for interstellar travel. One proposed method for utilizing antimatter as a fuel source is the antimatter beam core engine. The beam core design generates a thrust by redirecting charged particles from an antiproton-proton annihilation through an exhaust using a magnetic field. According to Newtons third law, the change in momentum of the particles being pushed towards the exhaust will generate an

equal impulse on the magnetic field in the opposite direction which will in turn be imparted on the entire engine and any vessel connected to the engine.

Antimatter has the remarkable ability to convert rest mass to kinetic energy through annihilation events. For an antiproton-proton annihilation event, Frisbee states that approximately 64% of the rest mass in the annihilation is converted to kinetic energy. The remaining 36% of the rest mass constitutes the mass of the daughter particles [1]. However, since we generate thrust from the momentum of particles moving through an exhaust, the annihilation allows full utilization of the mass energy as the mass contributes to the particles momentum and, therefore, the thrust produced.

In order to quantitatively analyze the effectiveness of antimatter as a fuel source, it is useful to calculate the specific impulse, a common measurement used in rocket science for comparative analyses of fuel sources. The specific impulse, given in units of seconds, is a measure of the amount of impulse generated by a certain weight of fuel where a higher specific impulse corresponds to more impulse generated by a lesser mass of fuel. Basic rocket physics dictates that in order to maximize the amount of velocity gained by a rocket, the mass of the rocket must be as low as possible. For this reason, a fuel with high specific impulse is important as more thrust can be produced with a lesser amount of fuel mass.

Keane and Zhang first utilized a modern version of Geant to simulate and optimize the antimatter beam core engine design in 2012 [2]. The simulation built by Keane and Zhang provided a rudimentary construction of the basic beamed core design for an antimatter engine. The research presented here aims to expand upon the work done by Keane and Zhang by refining elements of the analyses and making greater use of Geant's extensive capabilities. Keane and Zhang optimized based on pion efficiencies and cited pion exhaust velocities from a previous publication in order to determine a maximum effective exhaust velocity which they defined as the efficiency times the average pion velocity. As opposed to Keane and Zhang's simulation, our simulation tracks velocities for each particle within the simulation which allows us to calculate an average pion velocity within the simulation at both the exhaust and the pions point of production at the annihilation. Furthermore, we track vector momenta for all particles and refine the optimization to not only consider the efficiency at which pions reach the exhaust, but also the magnitude of each pions momentum in the desired direction of thrust. Ultimately, we calculate a value for specific impulse of the antimatter as a comparative measure to other fuel sources.

In subsequent sections we will discuss the general design of the engine as well as the simulation construction. Optimization plots for each parameter are shown as well as relevant kinematic data for the final optimized state. From this data, an argument is made for the effectiveness of an antimatter powered engine compared to traditional and other theoretical propulsion techniques as well as a comparison to the previous simulation done by Keane and Zhang.

2. The Simulation

The simulation is built using Geant 4.10.03 [3] with FTFP_BERT physics list which allows for the simulation of magnetic fields and hadronic interactions among other processes. Geant is a Monte Carlo based toolkit developed and maintained by CERN that simulates the passage of particles through matter. One of the focuses of our approach is to simulate realistic structures and materials necessary to construct such an engine.

Within the simulation, the engine is designed so a solenoid forms the outer cylindircal shell of the engine and produces a non uniform magnetic field that becomes weaker closer to the exhaust. Solenoids can produce non uniform magnetic fields in various ways; for example, by varying the radius which would give the solenoid a conical shape or by maintaining a cylindrical shape but varying the number of turns per length or current that flows through the solenoid. For this simuation, the latter option is chosen in order to give the particles the most room to propagate through the magnetic field and be redirected. The solenoid is placed in a Cartesian coordinate system so that the radius of the solenoid extends in the x and y directions while the length of the solenoid runs along the z-axis. Furthermore, the solenoid is given realistic material properties within the simulation in order to interact with particles that may come in contact with or pass through the solenoid and potentially produce additional annihilations. The solenoid is given a 10 cm thickness as well as niobium-titanium alloy material, a common material used in the particle physics industry to produce solenoids with strong magnetic fields [4].

The non-uniform magnetic field model produced by the solenoid follows [2], where the field has both radial and axial components given by $B_z(z) = B_{\max}(1 - gz)$ and $B_r(r) = \frac{1}{2} B_{\max} r$, where g is a gradient parameter that determines how quickly the field strength varies along the z-axis. For this study, we construct the gradient term to produce a linear decline in the magnetic field from the forward-end to the exhaust.

Within the solenoid, a liquid hydrogen target is positioned along the z-axis, which corresponds to the longitudal axis of the solenoid. The liquid hydrogen is encased in 1 mm thick stainless steel, grade 301, in order to simulate a realistic scenario in which the incoming antiproton beam would need to pass through a container to reach the liquid hydrogen target. At the forward end of the engine, an antiproton ($\bar{p}$) beam is simulated with a gaussian width of $\sigma_x = \sigma_y = 1$ mm. Additionally, four stainless steel rods of radius 10.0 mm are modeled to act as supports for the liquid hydrogen target container as well as an aluminum beam pipe that runs from the forward end to the center of the solenoid. The structure of the engine, as well as a typical annihilation event, can be seen in **Figure 1**. In the figure, blue and red tracks represent charged particles, as made evident by the redirection of the particle paths by the magnetic field, whereas green tracks correspond with neutral particle, as can be seen by the straight, undeflected paths since the neutral particles are not affected by the magnetic field.

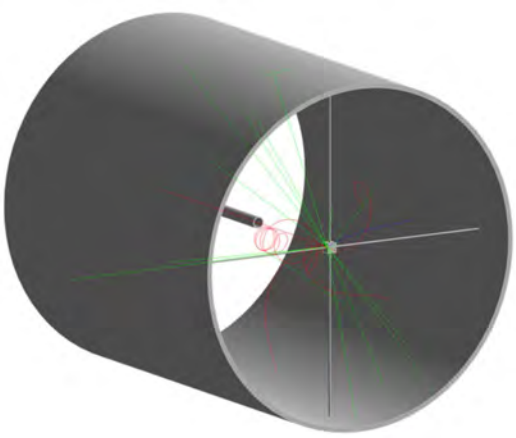

Figure 1. An isometric view of the basic core design.

The simulation allows for control over several parameters which are used for optimization as given by Table 1. These are the same parameters explored by Keane and Zhang for engine optimization though the ranges for optimization differ slightly. We scan these parameters with the updated analysis structure and engine geometry in an attempt to reproduce the results of Keane and Zhang's simulation. The optimization is performed by varying a single parameter using the ranges and step sizes given by Table 1 while all other parameters are held constant. For each parameter set, 100,000 events are generated where an event corresponds to an antiproton fired at the liquid hydrogen target. Data is gathered on a particle by particle basis and is analyzed in an ntuple structure within ROOT [5]. Once each parameter is optimized, an additional 100,000 events are generated with each parameter set to its optimized value.

3. Results

The simulation produces a myriad of various daughter particles as shown in Figure 2. The most abundant particles are gammas and charged leptons. Since gammas are electrically neutral, they cannot be redirected by the magnetic field and therefore make a negligible contribution to the impulse imparted to the engine. These gammas do pose a significant concern in terms of radiation which can be solved with significant radiation shielding, though extensive consideration of gamma radiation is beyond the scope of this paper. Additionally, charged leptons prove to be very inefficient in being redirected through the exhaust as only ≈ 8% of charged leptons produced make it to the exhaust. The next most abundant particles are charged pions which have a significant number of particles reaching the exhaust compared to the number produced. For this reason, this analysis focuses on charged pions as these particles are the most abundant particles found at the exhaust.

We define the engine efficiency for each particle type by the ratio of the number of particles reaching the exhaust plane to the number created by the $\bar{p}$ annihilation, $\epsilon = \frac{\#\text{exhaust}}{\#\text{production}}$. As seen in Figure 3 there is a significant

Table 1. Summary of parameters explored for engine optimization.

Parameter	Max Value	Min Value	Step Size
$\bar{p}$ KE	30 MeV	1 MeV	1 MeV
B_{max}	20 T	0 T	0.5 T
B_{min}	0 T	1 T	0.1 T
Solenoid Length	5 m	1 m	0.25 m
Solenoid Radius	2.5 m	0.5 m	0.25 m
Target Position (percentage of total length)	95%	50%	5%

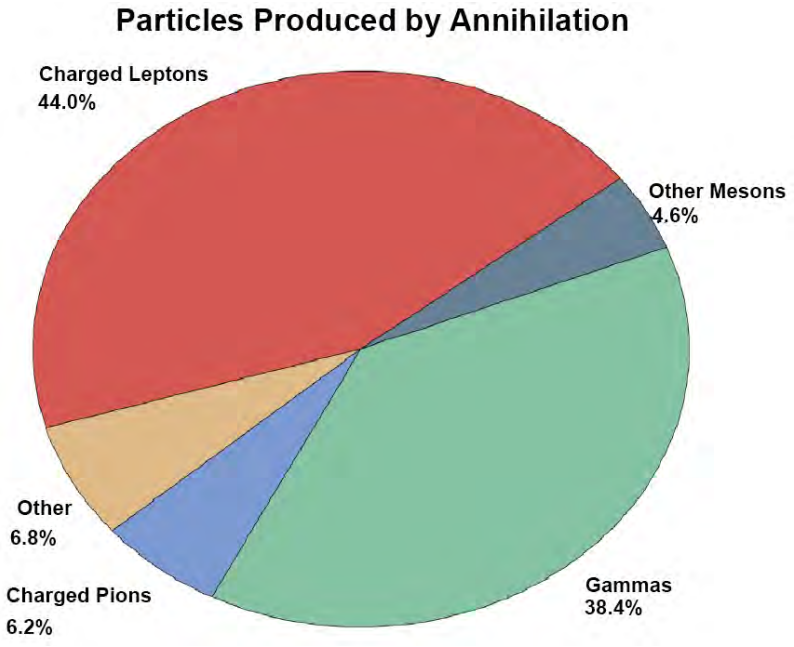

Figure 2. Shows the breakdown of the type of particles produced by the annihilation.

efficiency dependence on charged pion speed. After seeing this dependence, questions are raised as to what the proper efficiency number should be, specifically [2] quotes an efficiency of nearly 80%, however this appears to be the efficiency for the most probable $\pi^{\pm}$ speed, not an average, which is indicated by their nomenclature. Therefore, we quote two efficiencies, an average calculated from $\langle\epsilon\rangle = \epsilon\left(\langle\beta\rangle\right)$ and ϵ_{max} found at the most probable pion speed (≈ 0.95c). We define most probable pion speed as the speed at which most pions are travelling at the point of production.

We calculate the impulse from the standard definition of $\boldsymbol{I} = \Delta\boldsymbol{p}$. Specifically we calculate the z-component of the impulse on a particle per particle per event basis, therefore, for the ith particle in an event, the z-component of the impulse is given by, $I_{z,i} = p_{z,i}^{exhaust} - p_{z,i}^{prod.}$. It is the z-component of the impulse that supplies forward momentum to the engine as the exhaust is aligned along the z axis. This is evident in **Figure 4** as a clear shift in the z-component of the momentum can be seen from production to exhaust whereas the x and y components

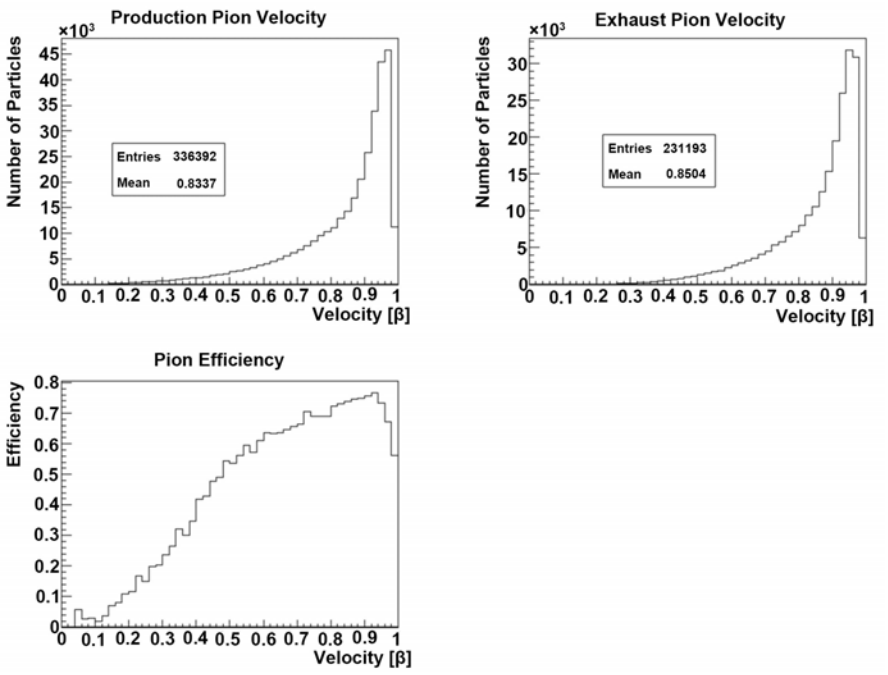

Figure 3. Figure shows the speed distributions for charged pions at production and at the exhaust plane as well as their efficiency as a function of their production speed, $\epsilon(\beta)$.

average close to zero indicating a negligible change in momentum in the x and y directions, as expected.

In calculating the impulse imparted on the engine we can calculate a specific impulse for the antiproton-proton annihilation, thus giving a value which we can compare to other fuel sources. Specific impulse is determined by the equation equation $I_{sp} = \frac{I_z}{mg}$ where I_z is the effective impulse, and m is the mass of the reactants, a proton and $\overline{p}$.

Our optimization is based on the product of average impulse and average efficiency, $I_z \cdot \epsilon$, generated by 100,000 events per parameter setting as previously shown in Table 1. The parameter is optimized when $I_z \cdot \epsilon$ is maximized indicating that the optimal balance of impulse and particles carrying the momentum through the exhaust has been achieved. Final optimized values of the parameters are given by Table 2. Furthermore, the variances in ϵ, I_z, and $I_z \cdot \epsilon$ for each parameter can be seen in Figures 5-10.

In its optimized state, the engine produces an impulse of 182.6 ± 0.5 MeV/c per event for charged pions which corresponds to (9.78 ± 0.03) × 10^{-20} Ns in SI units and a specific impulse of (2.49 ± 0.08) × 10^6 s. This specific impulse is much greater than those of current chemical processes which range from 240 to 400 s [6] and theoretical nuclear processes on the order of 3000 s [7]. These values suggest that for every kilogram of antiprotons and protons, approximately 1 million kilograms of chemical fuel would be needed to produce an equivalent amount of thrust.

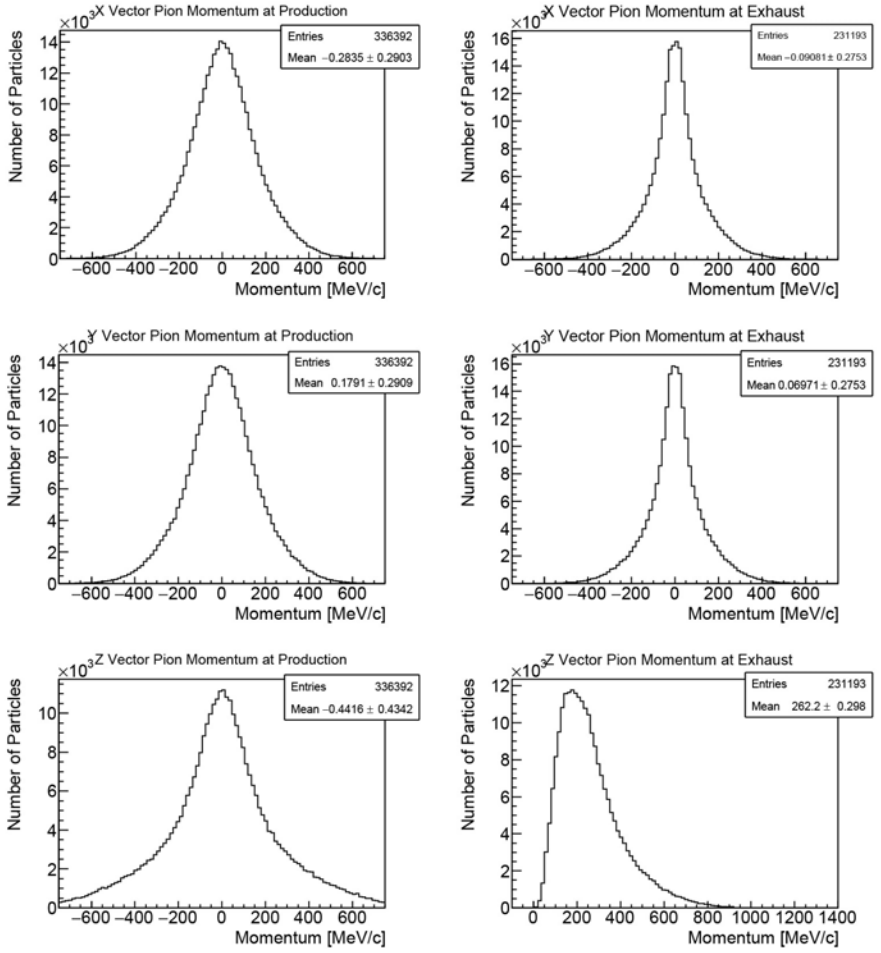

Figure 4. Figure shows the components of charged pion momentum at production and at the exhaust plane.

Table 2. Value of optimized engine parameters.

Parameter	Optimized Value
$\bar{p}$ KE	23 MeV
B_{max}	18.0 T
B_{min}	0.5 T
Solenoid Length	2.25 m
Solenoid Radius	2.25 m
Target Position (percentage of total length)	85 %

4. Conclusions

This simulation has shown that antimatter has exceedingly great potential as a fuel source for interstellar travel. The high specific impulse of $(2.49 \pm 0.08) \times 10^6$ s calculated in this simulation is orders of magnitude larger than that of current chemical rocket fuels which are usually between 240 - 400 s, as well as theoretical nuclear propulsion systems that are estimated to achieve upwards of 3000 s.

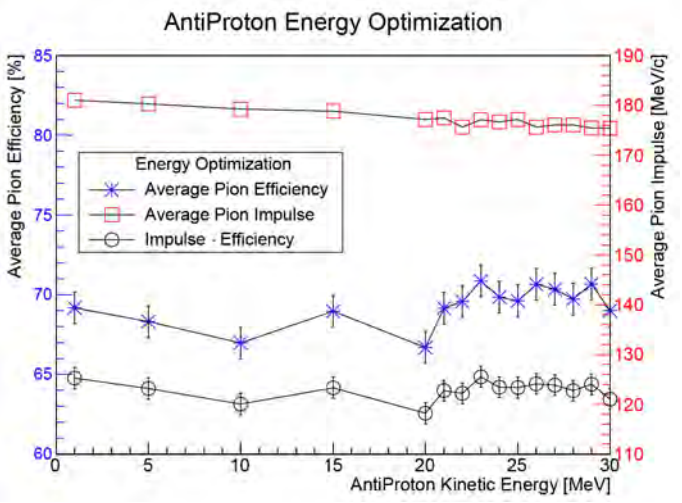

Figure 5. Figure shows the optimization for the kinetic energy of the incoming antiproton.

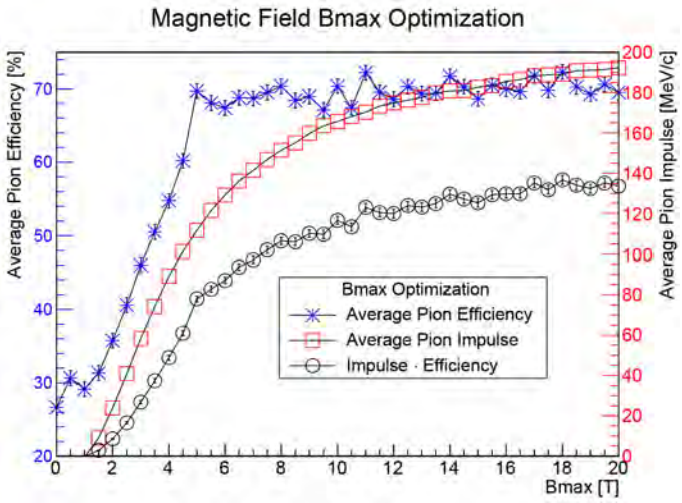

Figure 6. Figure shows the optimization of the Bmax parameter.

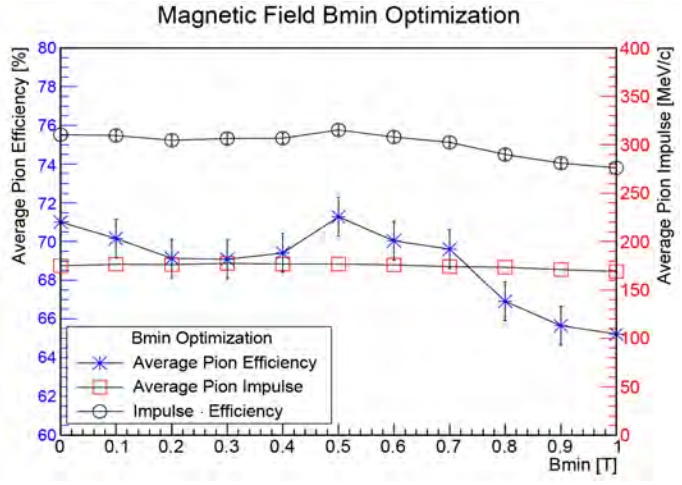

Figure 7. Figure shows the optimization of the Bmin parameter.

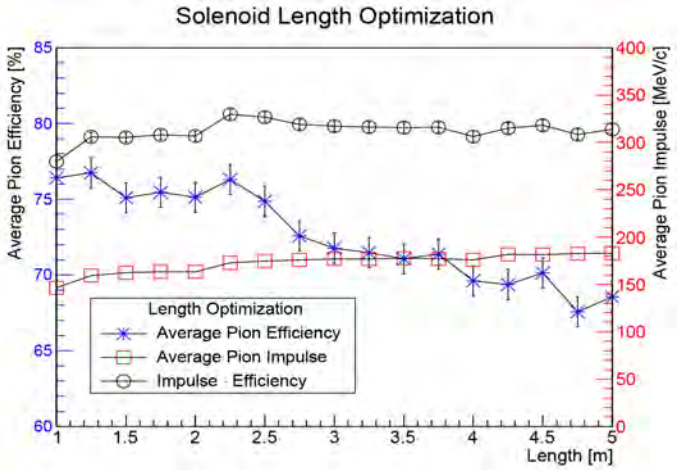

Figure 8. Figure shows the optimization of the solenoid length parameter.

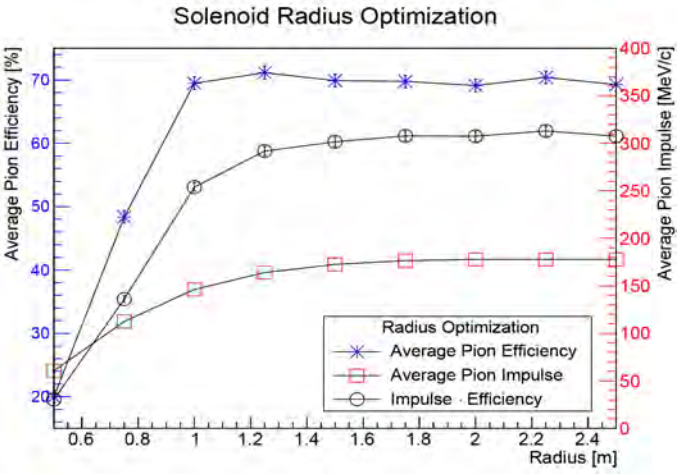

Figure 9. Figure shows the optimization of the solenoid radius parameter.

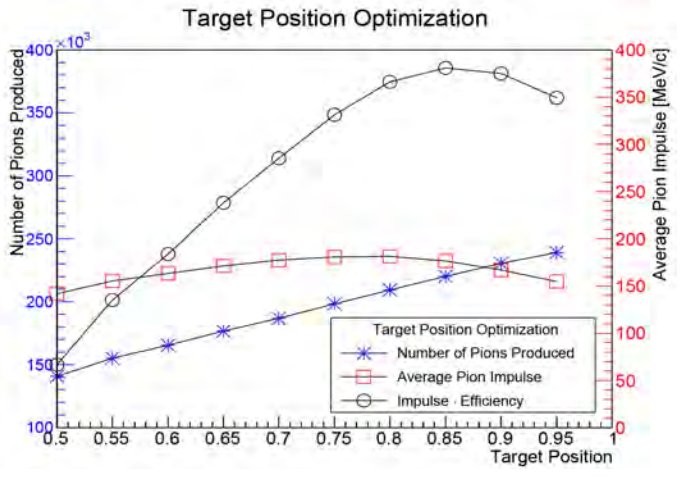

Figure 10. Figure shows the optimization of the liquid hydrogen target position parameter. Target position is given as a ratio of the total length of the solenoid.

Specific impulse as calculated here, however, merely indicates a maximum potential performance as the actual performance of the engine is limited by the rate at which fuel can be supplied to the reaction point.

The difficulty in utilizing antimatter in an engine as proposed here lies in the ability to produce enough antiprotons to fuel a spaceship. With current state of the art beam densities at 10^7 antiprotons/s [8], the engine would only produce a thrust of 9.78×10^{-13} N. When this thrust is applied to a 500 ton spacecraft, the resulting acceleration would be equal to 2.16×10^{-18} m/s^2. At this rate it would take 4.41×10^{20} years to reach half the speed of light. If the beam density was increased to 10^{28} antiprotons/s, the spacecraft would reach half the speed of light in just 1.6 days. Current proton beam densities produced for experiments conducted at Fermilab can supply protons to a target at a rate as high as 9.6×10^{13} protons/s [9]. If enough antiprotons were produced to create comparable $\overline{p}$ beams, it would still take an extraordinarily long time to reach half the speed of light at 4.59×10^{11} years. Chemical rockets, however, can supply fuel to the reaction point at much higher rates, allowing for more reactions in a given period of time which results in a higher thrust. As a result, these rockets compensate for a lower specific impulse by a high mass flow rate whereas antimatter fuel is heavily restricted by the low rate at which antiprotons are supplied to the reaction point despite a high specific impulse.

Obviously, in order to construct a practical antimatter engine there is a need for much denser $\overline{p}$ beams, but in order to produce denser beams $\overline{p}$ production rates need to be improved. Frisbee offers a positive outlook on the increase in antimatter production stating that in 45 years, $\overline{p}$ production increased on the order of 10^6 [1] and that it is not unreasonable to believe that a similar increase in magnitude of production may occur in the following 45 years. Furthermore, the addition of multiple beams within a single engine would increase the rate at which antiprotons are delivered to the target; however, $10\overline{p}$ beams would be needed just to increase the beam density by one order of magnitude.

Other issues in utilizing an antimatter fueled engine come from the naturally dangerous nature of antimatter due to its annihilation upon contact with ordinary matter. For this reason, use of an antimatter engine may only be feasible in outer space where an absence of atmosphere will allow antiprotons to propagate through the engine without being annihilated before reaching the desired annihilation point. The reaction of antimatter with matter also makes storing antiprotons difficult. Although storage of antiprotons has been achieved for long periods of time through magnetic suspension within a vacuum, there are greater challenges in being able to store enough antiprotons needed to fuel a space ship in a safe manner. Considering these factors, it is very unlikely that antimatter will ever completely replace chemical fuels but rather be used in conjunction with chemical rocket for deep space missions in the distant future.

In this simulation, we have also determined an average pion velocity of $0.85c$, a slightly higher value than the value of $0.81c$ cited by Keane and Zhang [2]. Whereas Keane and Zhang optimized based on pion efficiency in order to

maximize the effective exhaust velocity, we have optimized efficiency and impulse in order to maximize the impulse imparted on the engine. We feel this is a more effective approach to optimizing the antimatter engine as impulse is responsible for the thrust and acceleration of the engine whereas effective exhaust velocity is more useful in determining the maximum achievable velocity of the engine. As we have discussed previously, the difficulty in utilizing an antimatter engine lies in the ability to achieve a large enough acceleration to make a practical antimatter engine.

Acknowledgements

Matthew Dubiel is grateful to have received a scholarship through the STEM Connections Program at Lewis University, which is supported in part by NSF S-STEM Award #1458353, and to have had the opportunity to participate in this research as a STEM Connections Scholar. Any opinions, findings, and conclusions or recommendations expressed in this material are those of the authors and do not necessarily reflect the views of the National Science Foundation. The authors would also like to thank the Lewis University Summer Undergraduate Research Experience (S.U.R.E.) for funding this work during one summer.

Conflicts of Interest

The authors declare no conflicts of interest regarding the publication of this paper.

References

[1] Frisbee, R.H. (2003) How to Build an Antimatter Rocket for Interstellar Missions-Systems Level Considerations in Designing Advanced Propulsion Technology Vehicles. Impact of Interstellar Vehicle Acceleration and Cruise Velocity on Total Mission Mass and Trip Time. 39*th AIAAIASMEJSAWASEE Joint Propulsion Conference and Exhibit*, Huntsville Alabama, 20-23 July 2003. https://doi.org/10.2514/6.2003-4676

[2] Keane, R.L. and Zhang, W.M. (2011) *Journal of Propulsion and Power*, **27**, 1153-1156.

[3] Allison, J., *et al.* (2016) *Nuclear Instruments and Methods in Physics Research A*, **835**, 186-225.

[4] Ostojic, R., *et al.* (2014) *IEEE Transactions on Applied Superconductivity*, **24**, 1-4.

[5] Antcheva, I., et al. (2009) *Computer Physics Communications*, **180**, 2499-2512.

[6] Powell, J., Maise, G. and Paniagua, J. (2004) *Aerospace America*, **42**, 36-38.

[7] Borowski, S.K., e*t al.* (2010) Nuclear Thermal Propulsion (NTPS). Wiley Online Library.

[8] FLAIR—Facility for Low-Energy Antiproton and Heavy Ion Research. https://www.fair-center.eu/public/experiment-program/appa-physics/flair.html

[9] Bartoszek, L., *et al.* (2015) Mu2e Technical Design Report, FERMILAB-TM-2594.

Journal of Modern Physics, 2019, 10, 1364-1373
https://www.scirp.org/journal/jmp
ISSN Online: 2153-120X
ISSN Print: 2153-1196

Wave Harmonization in Hierarchic Quasicrystals by the Analytic Metric

Antony J. Bourdillon

UHRL, San Jose, CA, USA
Email: bourdillona@sbcglobal.net

How to cite this paper: Bourdillon, A.J. (2019) Wave Harmonization in Hierarchic Quasicrystals by the Analytic Metric. *Journal of Modern Physics*, **10**, 1364-1373.
https://doi.org/10.4236/jmp.2019.1011090

Received: September 10, 2019
Accepted: October 18, 2019
Published: October 21, 2019

Copyright © 2019 by author(s) and Scientific Research Publishing Inc.
This work is licensed under the Creative Commons Attribution International License (CC BY 4.0).
http://creativecommons.org/licenses/by/4.0/
Open Access

Abstract

Thirty seven years after the discovery of quasicrystals, their diffraction is completely described by harmonization between the sine wave probe with hierarchic translational symmetry in a structure that is often called quasiperiodic. The diffraction occurs in geometric series that is a special case of the Fibonacci sequence. Its members are irrational. When substitution is made for the golden section τ by the semi-integral value 1.5, a coherent set of rational numbers maps the sequence. Then the square of corresponding ratios is a metric that harmonizes the sine wave probe with the hierarchic structure, and the quasi-Bragg angle adjusts accordingly. From this fact follows a consistent description of structure, diffraction and measurement.

Keywords

Quasicrystal, Icosahedra, Hierarchic, Harmonization, Metric, Geometric Series

1. Introduction

"Physical" theories degenerate easily to common myth when the basic norms of physical practice are ignored. These include not only verification by exclusion of falsifiable hypotheses, but also rigorous implementation of the formal and informal logic that has been endorsed by scientists for over two millennia [1] [2]. Self-styled quasicrystallographers claim (e.g. [3] p. 82) that the diffraction observed in quasicrystals is Bragg diffraction. The claim might have either a weak or a strong meaning, though they evidently mean it in the strong sense. The weak sense is that the diffraction is due to a 3-dimensional scatterer rather than a 2-dimensional grating. When a reflection grating is rotated by a small angle α, the diffracted beam rotates specularly by 2α; whereas the diffraction from a 3-D crystal switches sharply on and off as it rocks about the Bragg condition. In this strong sense, diffraction is described by Bragg's law: at wavelength λ, light is re-

flected from regular interplanar spacings of width d at the Bragg angle θ (the complement to the angle of incidence) which is constrained such that $n\lambda = 2d\sin(\theta)$, where n represents the diffraction order. This law describes diffraction in crystals. Quasicrystals provided a new and unique type of diffraction.

2. Quasicrystal Diffraction

2.1. Diffractive Order *n*

In crystals, the order is positive integral: $n = 0,1,2,3\cdots$; whereas in the quasicrystal; the order is represented in powers of the golden section τ^m, where $\tau = (1 + 5^{1/2})/2$ and m is positive or negative, $m = -\infty,-1,0,1,2,3\cdots$ corresponding to $n = 0,1/\tau,1,\tau,\tau^2,\tau^3\cdots$. The quasi-Bragg law is a new law in physics: $\tau^m\lambda = 2d'\sin(\theta')$, where the apostrophes indicate compromise superpositions of many Bragg values. The geometric series is a special case of the Fibonacci sequence: in the former case, the ratio between successive terms is constant; in the latter case the ratio oscillates about τ. Such oscillations are not observed in the quasicrystal diffraction pattern.

2.2. Quasiperiodicity

The discovery of Shechtman *et al.* [4] was entitled "a metallic phase with long range order an no translational symmetry". Imaging showed multiple interplanar spacings irregularly jumbled. Bragg's specific d_{hkl} for an indexed beam (hkl) is therefore neither unique in the quasicrystal nor periodic, so the wonder that has to be explained is how the diffraction due to such a structure can be sharp. In the following discussion, we show precisely how that occurs and how the model is verified by measurement. Meanwhile neither n nor d obey Bragg's law.

2.3. The Quasi-Bragg Angle

Since d is not unique, the Bragg angle is not defined and does not obey Bragg's law either. However, we will show how the quasi-Bragg angle θ' is calculated, and it is certainly not the Bragg angle. There is no Bragg diffraction.

2.4. What Do We Know?

Given the composition Al_6Mn, we know that *Al* has the atomic number 13 and Mn 25. The scattering power for electrons used in transmission electron microscopy is four times greater for the transition metal. In phase-contrast optimum defocus [5] Mn is readily specified and located [3] [6] [7]. The image demonstrates a hierarchic icosahedral structure that is four tiers deep and apparently expansive indefinitely. Every atom is specified, located and measured for size.

The unit cell is edge sharing. This results in the 13 atom unit cell having the stoichiometry Al_6Mn (**Figure 1**). It is extremely dense owing to the precise ratio of the central Mn atom to outer Al atoms. All diatomic quasicrystals share the same ratio.

Knowing the structure, we can simulate the diffraction pattern; but it is necessary first to correct indexation.

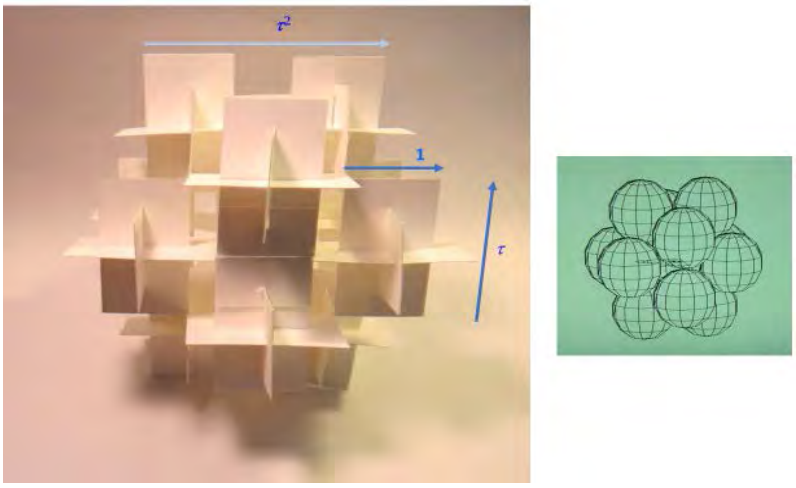

Figure 1. Dense, icosahedral, unit cell (right) and dimensions of the logarithmically periodic structure (left) with stretching factor τ^2. This is the ratio of the edge of the icosahedral cluster to the edge of the unit cell.

2.5. Indexation

The stereogram of principal axes of the icosahedral structure is 3-dimensional, in geometric series, simple, and complete [8] [9]. So also are the principal diffraction planes that are normal to the axes. Following William of Ockham, dimensions should not be multiplied without necessity. Inventing dimensions does not solve physical problems[1]. All of the beams in the original data [4] have been indexed on this basis ([6] and refs.) and their quasi-structure factors (QSFs) calculated [3] [6] [7] and summarized as follows.

2.6. Quasi-Structure Factors (QSFs)

The sites of atoms and cell centers in icosahedral clusters are known [7] [9] [10], including sites in higher order p of supercluster, where indices multiply by τ^{2P}:

$$\begin{aligned} \text{Unit cell}\left(r_u\right):\ \text{Mn} &\quad (0,0,0) \\ \text{Al} &\quad 1/2\left(\pm\tau,0,\pm1\right),1/2\left(0,\pm1,\pm\tau\right),1/2\left(\pm1,\pm\tau,0\right) \end{aligned} \tag{1}$$

and

$$\text{Cell or cluster centers}\left(r_{cc}\right)\quad 1/2\left(\pm\tau^2,0,\pm\tau\right),1/2\left(0,\pm\tau,\pm\tau^2\right),1/2\left(\pm\tau,\pm\tau^2,0\right), \tag{2}$$

The QSF formula is adapted from classical crystallography with two differences:

$$F_{hkl}=\sum_{i=1}^{\text{all atoms}} f_i \cos\left(2\pi.c_s\left(\overline{h_{hkl}}\cdot\overline{r_i}\right)\right) \tag{3}$$

Firstly, because the diffraction is sharp in spite of multiple interplanar spacings d, a coherence factor c_s is inserted. Its value will be derived analytically below. Initially the factor is used as a scanned variable (**Figure 2**) to illustrate the

[1]Crystallographers know that the hexagonal close packed structure is sometimes indexed with four digits; sometimes with three. Equally they know that the structure is 3-dimensional R^3—in this it is like the quasicrystal.

variance of quasi-Bragg diffraction from Bragg diffraction in crystals.

Secondly, because the unit cells are not periodic as in crystals, the summation is made over all atoms in the quasicrystal; not just the unit cell. The summation is taken in two steps: over the unit cell and cluster, and iteratively over the superclusters in hierarchic order p. Write the vector from the origin to each atom in a cluster $\overline{r_{cl}}$ as the sum of a unit cell vector $\overline{r_u}$, with a vector to the cell centers in the cluster $\overline{r_{cc}} : \overline{r_{cl}} = \overline{r_{cc}} + \overline{r_u}$. Then since

$$\sum_{i}^{\text{Ncluster}} \exp\left(\overline{h_{hkl}} \cdot \overline{r_{cl}}\right) = \sum_{i}^{12} \exp\left(\overline{h_{hkl}} \cdot \overline{r_{cc}}\right) \times \sum_{i}^{13} \exp\left(\overline{h_{hkl}} \cdot \overline{r_u}\right) \tag{4}$$

with corresponding summations over unit cell sites and cell centers, and knowing that $N_{cluster} = N_{cc} \cdot N_u$, the QSF for the cluster may be calculated:

$$F_{hkl}^{cluster} = \sum_{i=1}^{12} \cos\left(2\pi \cdot c_s \left(\overline{h_{hkl}} \cdot \overline{r_{cc}}\right)\right) \cdot F_{hkl}^{cell} \tag{5}$$

and repeating iteratively over superclusters by using the known stretching factor τ^{2p}:

$$F_{hkl}^{p} = \sum_{i=1}^{\text{all atoms}} \cos\left(2\pi \cdot c_s \left(\overline{h_{hkl}} \cdot \tau^{2p} \overline{r_{cc}}\right)\right) \cdot F_{hkl}^{p-1} \tag{6}$$

The example in the figure is for the simple geometric series, but all beams in the original data [4] have been calculated to match. All structure factors, *i.e.* at the Bragg condition $c_s = 1$, are zero. In the quasicrystal there is no Bragg diffraction: all beams peak at the quasi-Bragg condition $c_s = 0.894$. As we shall see, this value is the result of harmonization of the incident, sine wave probe with the aperiodic, hierarchic structure.

2.7. Quasi-Bloch Waves

In crystals, Bloch waves [11] [12] can be observed as lattice images observed, for example, in the two beam Bragg condition. The waves occur as interference between incident and reflected waves. Two are simulated as the red trace for the quasicrystal (**Figure 3** with $c_s = 0.894$), for comparison with the blue, anharmonic, (100), pseudo-Bragg condition, $c_s = 1$.

The quasi-Bloch wave harmonizes with the hierarchic structure; the pseudo-Bragg wave does not diffract.

2.8. Principal Planes

The golden triad contains three orthogonal golden rectangles. There are three principal planes, one for each dimension of the golden triad (**Figure 4**). The triad scales within the hierarchy for each order of unit cell, cluster and supercluster. The listing of interplanar spacings illustrates the origin of the geometric series in the quasicrystal diffraction pattern.

For each order of cluster, golden triads mark principal planes that locate subcluster centers at corners. These centers operate as principal scatterers for the hierarchic structure. The diffraction occurs by reflection between hierarchic

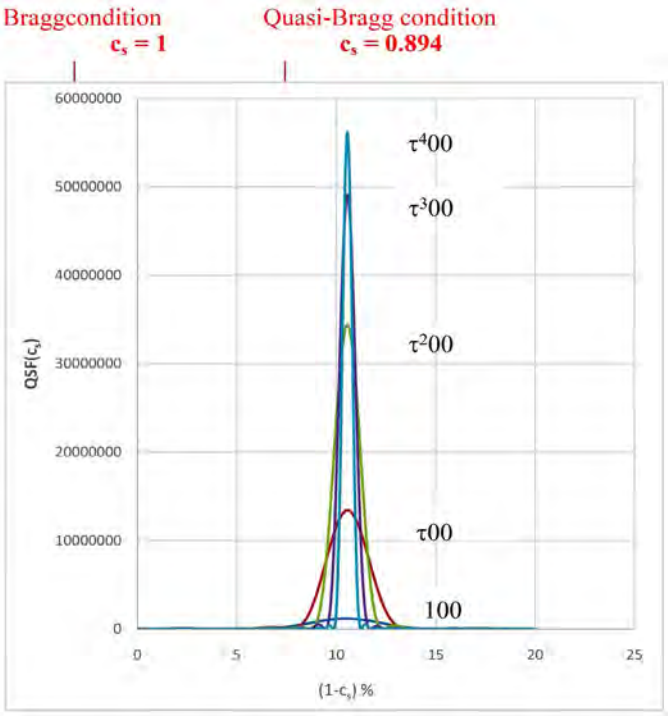

Figure 2. A selection of QSF displays obtained by scanning c_s. Indexed lines are shown for an i-Al_6Mn supercluster order 2 (~10^4 atoms). The lines peak consistently when c_s = 0.894 [6] with similar intensities (FWHM). By contrast QSFs for the Bragg condition (c_s = 1 and $n = 0,1,2,3\cdots$) are unregulated, with more or less random QSF structures, spread out and very weak. All structure factors at the Bragg condition are ~zero. There is no Bragg diffraction.

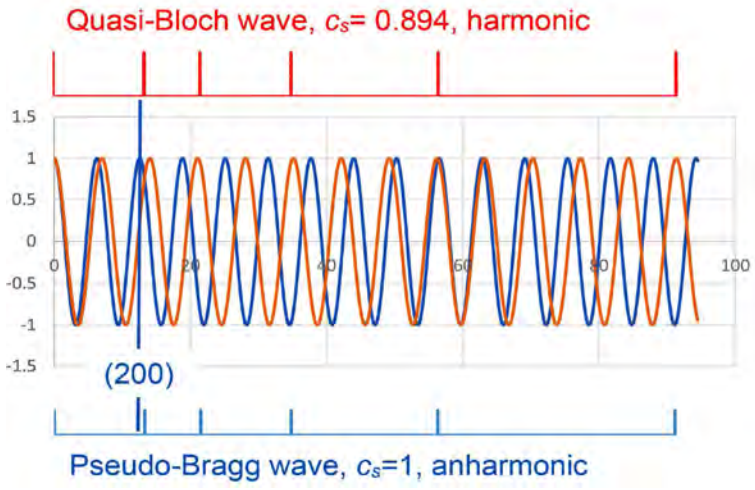

Figure 3. Plotted across principal planes (red upper grid) in geometric series in the hierarchic structure, are a red quasi-Bloch wave (c_s = 0.894) and a blue pseudo-Bragg wave (c_s = 1). The former is harmonic consistent with coherent diffraction; the latter is anharmonic and does not diffract. The metric harmonizes the quasi-Bloch wave with the hierarchic structure. The long vertical blue would mark the Bragg (200) line if it were allowed. Notice that a contraction in d, dilates a Bloch wave; so does c_s in $d' = d \cdot c_s$ in the quasicrystal.

centers of unit cells, clusters and superclusters. Each reflection is weighted by parallel reflections from the bodies of respective sub-clusters or sub-superclusters. That is why, in Figure 2, the line widths narrow with increasing power on the index, consistent with increasing numbers of scattering atoms. The diffraction consists in coherent scattering from hierarchic bodies of the same order.

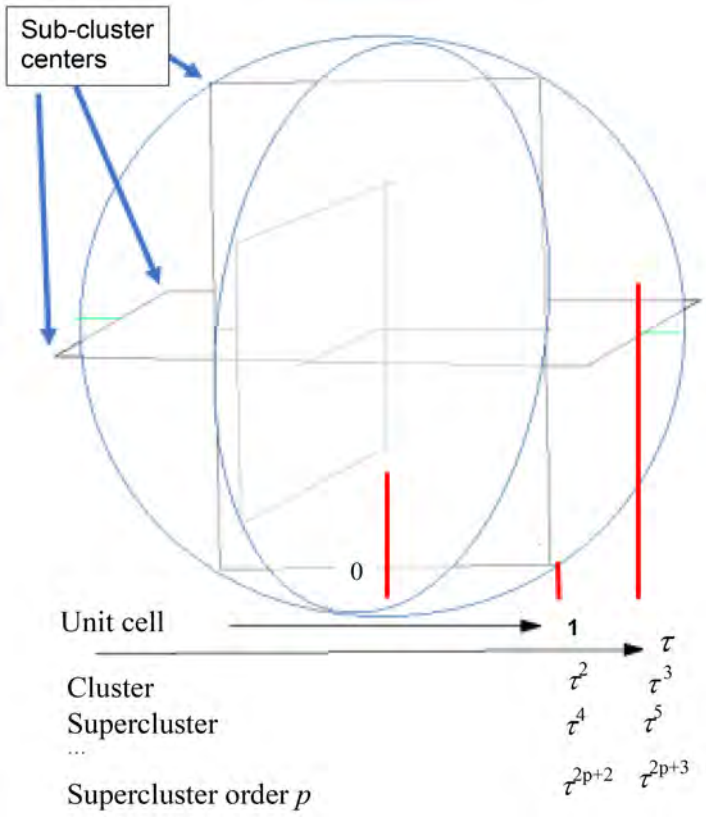

Figure 4. Principal atomic planes are located by red lines. The golden triad scales to represent hierarchic orders of: unit cell, cluster and superclusters. Notice the interplanar spacings in geometric series $0,1,\tau,\tau^2,\tau^3\cdots$ that correspond to diffraction pattern series. Coherent diffraction occurs by scattering of corresponding sub-cluster bodies centered on the corners of the golden rectangles.

2.9. Analytic Derivation for the Metric

The principal planes determine the coherence factor and metric (Table 1). The planes lie in geometric series. This series is irrational but a rational approximation may be constructed by the substitution of the rational fraction 3/2 for τ as shown in the table. It is obvious that atoms located on the half-integral set of "coherent values" (column 7) could diffract coherently according to Bragg's law if such a structure could be constructed. It follows that, owing to the systemically derived value for the ratio r, atoms located on the "real" geometric-series lattice will likewise diffract coherently, but with the metric displacement $c_s \sim 0.894$, as in Figure 2. This fact is confirmed by the numerical QSF calculations. Coherent

Table 1. The metric is derived approximately from principal planes (bold column 10 with underlines) as follows: Bold column 6 shows irrational real values for the geometric series and Fibonacci equivalents on the same row; coherent values are rationalized by substitution for τ in the Fibonacci equivalent (columns 1-2) by the fraction 3/2 (as in the formula on the 3rd row). The harmony in the hierarchic scattering by the incident sine wave results in coherent diffraction. The square of the ratio of Rational value/Real value, on principal planes, is close to the numerical value for c_s given by QSF simulations from various supercluster orders (underlined in column 10). Column 10 is otherwise semi-empirical.

Geometric series								Irrational	Rational	Ratio	r^2	c_s	QSF
a		b						value	approx.	r		estimates	supercluster
									a+b*1.5	rat/irr		$1-2*(1-r)$	(order)
0				=	0	=		**0**	0	0	0	**0**	
1				=	1	=		**1**	1	1	1	**1**	
			t	=	t	=		**1.61803**	1.5	0.927	0.859	**0.854**	
1	+		t	=	t^2	=		**2.61803**	2.5	0.955	0.912	**0.91**	
1	+	2	t	=	t^3	=		**4.23607**	4	0.944	0.891	**0.888**	
2	+	3	t	=	t^4	=		**6.8541**	6.5	0.948	0.899	**0.896**	
3	+	5	t	=	t^5	=		**11.0902**	10.5	0.947	0.897	**0.894**	
5	+	8	t	=	t^6	=		**17.9443**	17	0.947	0.897	**0.894**	
8	+	13	t	=	t^7	=		**29.0344**	27.5	0.947	0.897	**0.894**	
13	+	21	t	=	t^8	=		**46.9787**	44.5	0.947	0.897	**0.894**	sc(2)
21	+	34	t	=	t^9	=		**76.0132**	72	0.947	0.897	**0.894**	
34	+	55	t	=	t^{10}	=		**122.992**	116.5	0.947	0.897	**0.894**	sc(3)
55	+	89	t	=	t^{11}	=		**199.005**	188.5	0.947	0.897	**0.894**	
89	+	144	t	=	t^{12}	=		**321.997**	305	0.947	0.897	**0.894**	
144	+	233	t	=	t^{13}	=		**521.002**	493.5	0.947	0.897	**0.894**	
233	+	377	t	=	t^{14}	=		**842.999**	798.5	0.947	0.897	**0.894**	
377	+	610	t	=	t^{15}	=		**1364**	1292	0.947	0.897	**0.894**	
610	+	987	t	=	t^{16}	=		**2207**	2090.5	0.947	0.897	**0.894**	sc(6)

r^*r^+: ($\because$ Intensities α QSF^2) here calculated for principal planes only; #: values simulared QSFs including ALL planess, and these match estimates; and elementary estimates: $c_s = 1/(1 + (t - 1.5))$ and $c_s = 1/(1-(t^2 - 2.5))$.

diffraction occurs by the QSF selection of $d' = d \cdot c_s$ and consequently of $\theta' = q/c_s$ under the quasi-Bragg law. Consistent with the measured value for the lattice parameter to be discussed below, the metric c_s is the ratio of corresponding terms: (coherent value)^2/(real value)^2. The square on the ratio is due to wave mechanics, where the intensities of the beams are—for centrosymmetric structures—squares of corresponding amplitudes.

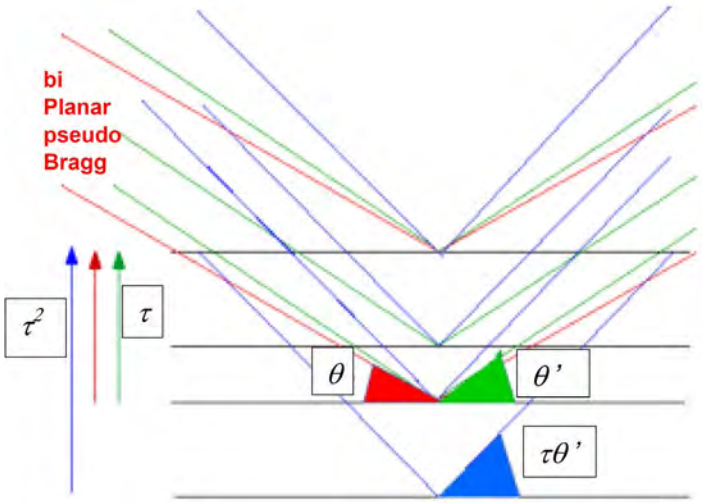

Figure 5. Models for biplanar Bragg diffraction (red rays) compared with multiplanar quasi-Bragg diffraction (green rays for first order; blue for second order), where all atoms scatter. Notice the multiplanar quasi-Bragg angle θ' is larger than the corresponding biplanar pseudo-Bragg angle θ.

2.10. The Model for Quasicrystal Diffraction

All atoms scatter. Whereas the uniqueness of d and its periodicity forces Bragg diffraction in crystals to reflect as *biplanes*; quasiperiodicity forces *multiplanar* reflections in hierarchic quasicrystals (Figure 5). Their superposition is described by the QSFs.

On the well-known model, the path difference between two reflections from adjacent Bragg planes is equal to the wavelength of the light, with $c_s = 1$. QSFs imitate the corresponding interference of the quasi-Bragg rays from multiple planes at the quasi-Bragg condition (*i.e.* when $c_s = 0.894$). Notice that the filled green quasi-Bragg angle is larger than the corresponding filled red Bragg angle.

In Bragg diffraction, when d contracts θ dilates; in quasi-Bragg diffraction, when c_s (and d') contract, θ' dilates. The dilatation is enforced by a constructive interference requirement for harmonic reflections. Actually, the better model for quasicrystal diffraction is shown in Figure 4: the diffraction consists in coherent scattering from sub-cluster centers rather than Bragg biplanes.

3. Summary

The correlating roles of quasi-structure factors and quasi-Bragg law are summarized in Table 2, where they are compared with Bragg diffraction in crystals. The QSF simulates the metric, the compromise interplanar spacing and indexation. With these parameters, the quasi-Bragg law measures the compromise quasi-Bragg angle. The summary shows how the measured lattice parameter is corrected for metric and indexation. The result is consistent in both structure and diffraction: they are measured, and verified.

From these measurements the reciprocal lattice can be derived [3] [6] [13]. The original data show two superposed lattices owing to subgroups in the

Table 2. Comparison of parameters used to describe Bragg diffraction with parameters for quasi-Bragg diffraction in hierarchic structures. The quasi-structure factor is used to calculate the metric c_s, the lattice parameter a and the compromise inter planar spacing d'. The quasi-Bragg Law is used to calculate the compromise quasi-Bragg angle $q'_{hkl} = q_{hkl}/c'_s$. The lattice parameter, that previously has been measured under Bragg assumptions, is corrected for c_s and indexation. The measurement is verified by consistency between atomic size, diffraction, and structure.

Comparison of Bragg parameters in crystals, with quasi-Bragg parameters in quasicrystals		
Bragg	**Quasi-Bragg**	**Comment**
$n = 2d\sin(q)/\lambda$	$\tau^m = 2d'\sin(\theta')/\lambda$	Harmonic laws Give us $\theta' = \theta/c_s$
$F_{hkl} = \sum f_i \cos(2\pi h_{hkl}\cdot r_i)$	$F'_{hkl} = \sum f_i \cos(2\pi c_s(h_{hkl}\cdot r_i))$ including iteration	Structure factors Give c_s, a and $d' = d\cdot c_s$
$d = a/h$	$d' = ac_s h$	$\theta' = \theta/c_s$
	$a = 0.205\tau c_s$ nm [1]	Measured lattice parameter $a \approx$ **Diameter of *Al***
	$a^* = 2p/a$	**Measured and verified**

n: Bragg order; m: Quasi-Bragg order; d: Bragg interplanar spacing; θ: Bragg angle; λ: wavelength; τ: golden section; prime: quasi-Bragg compromise; F: Structure factors; f_i: atomic scattering factor for atom i; c_s: metric; r_i: atom position; h_{hkl}: plane normal for indices h, k, l; a: lattice parameter (cubic) ~ *Al* diameter; reciprocal: lattice vector $a^* = 2\pi/a$.

icosahedral point group symmetry. The dual lattice is also consistent with the analysis. Moreover, the hierarchic translational symmetry is the obvious reason for the "long range order" [4] in what are typically called "quasiperiodic solids".

Moreover, the QSF simulations, when combined with harmonic analysis, demonstrate that the diffraction occurs on a scale that is a contraction of the irrational hierarchic scale of the structure. In consequence, all structural measurements that are derived from the diffraction pattern, are subject to the measured metric.

In particular, the fact that the lattice parameter was previously tentatively measured by wrongly assuming Bragg's law [14] [15], now has a corrected value (**Table 2**) equal to both the diameter of the Al atom and the width of the unit cell. This is necessary verification for the consistent theory.

4. Conclusion

The analytic metric completes the union of structure with diffraction. The hierarchic structure transforms the plane incident wave into geometric space. It is time to append the context. In comparatively recent times Senechal wrote for the American Mathematical Society a paper titled, "What is a quasicrystal?" The paper began, "The short answer is no one is sure" [16]. This was not true; the analytic metric shows why. The long path has been delayed by stray paths and some of them can be listed. Dimensions should not be multiplied without necessity—they do not solve physical problems. Mathematical axioms are chosen; physical hypotheses require verification (or more strictly falsification). While

theorems must be consistent with chosen axioms; consistency is not required in physical hypotheses because they are equal as "logically true" until one is "falsified" (referee preference is no ground for refusing publication). Categories have been erroneously applied. For example, the sub-editor of *Acta Crystallographica* wrote that you don't measure the lattice parameter, "You just have to choose 'd_h'" ([3] p. 82). This is like saying, "You don't measure the speed of light; you choose it," or, "You don't calculate the speed of light; you choose it." He continued by writing, "Bragg's equation cannot be applied if we do not know how to handle the term d_h." He chose an untested law that never applies. It is not normal to comment on necessities of physical practice, nor on formal and informal logic; but 37 years are a long delay.

Conflicts of Interest

The author declares no conflicts of interest regarding the publication of this paper.

References

[1] Popper, K.R. (1959) The Logic of Scientific Discovery. Basic Books, Inc., New York. https://doi.org/10.1063/1.3060577

[2] Popper, K.R. (1982) Quantum Theory and the Schism in Physics.

[3] Bourdillon, A.J. (2012) Metric, Myth and Quasicrystals. UHRL, San Jose.

[4] Shechtman, D., Blech, I., Gratias, D. and Cahn, J.W. (1984) *Physical Review Letters*, **53**, 1951-1953. https://doi.org/10.1103/PhysRevLett.53.1951

[5] Bursill, L.A. and Peng, J.L. (1985) *Nature*, **316**, 50-51. https://doi.org/10.1038/316050a0

[6] Bourdillon, A.J. (2019) *Journal of Modern Physics*, **10**, 624-634. https://doi.org/10.4236/jmp.2019.106044

[7] Bourdillon, A.J. (2009) Quasicrystals and Quasi Drivers. UHRL, San Jose.

[8] Bourdillon, A.J. (2013) *Micron*, **51**, 21-25. https://doi.org/10.1016/j.micron.2013.06.004

[9] Bourdillon, A.J. (2016) *Journal of Modern Physics*, **7**, 43-50. https://doi.org/10.4236/jmp.2016.71005

[10] Bourdillon, A.J. (2016) *Journal of Modern Physics*, **7**, 1558-1567. https://doi.org/10.4236/jmp.2016.712142

[11] Bourdillon, A.J. (2011) Logarithmically Periodic Solids. Nova Science, New York.

[12] Hirsch, P., Howie, A., Nicholson, R.B., Pashley, D.W. and Whelan, M.J. (1977) Electron Microscopy of Thin Crystals. Krieger, New York.

[13] Bourdillon, A.J. (2019) The Analytic Metric in Quasicrystals, and the Reciprocal Lattice. https://www.youtube.com/watch?v=v011ZAUimq4

[14] Bourdillon, A.J. (1987) *Philosophical Magazine Letters*, **55**, 21-26. https://doi.org/10.1080/09500838708210435

[15] Tsai, A.P. (2008) *Science and Technology of Advanced Materials*, **9**, 1-20.

[16] Senechal, M. (2006) *Notices to the American Mathematical Society*, **3**, 886-887.

Journal of Modern Physics, 2019, 10, 1374-1393
https://www.scirp.org/journal/jmp
ISSN Online: 2153-120X
ISSN Print: 2153-1196

A Formulation of Spin Dynamics Using Schrödinger Equation

Vu B. Ho

Advanced Study, 9 Adela Court, Mulgrave, Australia
Email: vubho@bigpond.net.au

How to cite this paper: Ho, V.B. (2019) A Formulation of Spin Dynamics Using Schrödinger Equation. *Journal of Modern Physics*, **10**, 1374-1393.
https://doi.org/10.4236/jmp.2019.1011091

Received: July 30, 2019
Accepted: October 20, 2019
Published: October 23, 2019

Copyright © 2019 by author(s) and Scientific Research Publishing Inc.
This work is licensed under the Creative Commons Attribution International License (CC BY 4.0).
http://creativecommons.org/licenses/by/4.0/
Open Access

Abstract

In quantum mechanics, there is a profound distinction between orbital angular momentum and spin angular momentum in which the former can be associated with the motion of a physical object in space but the latter cannot. The difference leads to a radical deviation in the formulation of their corresponding dynamics in which an orbital angular momentum can be described by using a coordinate system but a spin angular momentum cannot. In this work, we show that it is possible to treat spin angular momentum in the same manner as orbital angular momentum by formulating spin dynamics using Schrödinger equation in an intrinsic coordinate system. As an illustration, we apply the formulation to the dynamics of a hydrogen atom and show that the intrinsic spin angular momentum of the electron can take half-integral values and, in particular, the intrinsic mass of the electron can take negative values. We also consider a further extension by generalising the formulation so that it can be used to describe other intrinsic dynamics that may associate with a quantum particle, for example, when a hydrogen atom radiates a photon, the photon associated with the electron may also possess an intrinsic dynamics that can be described by an intrinsic wave equation that has a similar form to that for the electron.

Keywords

Spin Angular Momentum, Spin Dynamics, Orbital Angular Momentum, Schrödinger Equation, Half-Integer Values, Intrinsic Coordinate Systems, Negative Mass

1. Introduction

In quantum physics, together with the wave-particle duality, spin angular momentum of an elementary particle is a novel dynamical feature that makes

quantum mechanics stand out and be distinguished from those that are established in classical mechanics, such as the familiar orbital angular momentum. We will show in Section 2 that the profound distinction between orbital angular momentum and spin angular momentum is that the former can be associated with the motion of a physical object in space but the latter can only be formulated in terms operators that are used to formulate the mathematical background for quantum physics. The difference leads to a radical deviation in the formulation of their corresponding dynamics in which an orbital angular momentum can be described by using a coordinate system but a spin angular momentum cannot. In this work, we show that it is possible to treat spin angular momentum in the same manner as orbital angular momentum by representing a formulation of spin dynamics using Schrödinger equation in an intrinsic coordinate system. As an illustration, we will apply the formulation that is established in Section 4 to the dynamics of a hydrogen atom and show that the intrinsic spin angular momentum of the electron can take half-integral values when the dynamics is described by Schrödinger equation in two-dimensional space. However, in order to show that such space can in fact exist, we show in Section 3 a formulation of two-dimensional dynamics of a quantum particle using Dirac equation. In Section 5, we will generalise the formulation so that it can be used to describe other intrinsic dynamics that may associate with a quantum particle, and as an another illustration, we will consider the physical process in which when a hydrogen atom radiates a photon, the photon associated with the electron may also possess an intrinsic dynamics that can be described by an intrinsic wave equation that has a similar form to the wave equation that describes the dynamics of the electron.

2. Dynamical Nature of Spin Angular Momentum in Quantum Mechanics

In quantum mechanics, despite the fact that spin angular momentum has been shown to play an almost identical role to orbital angular momentum, especially in relation to interaction with magnetic fields, spin has distinctive properties that make it profoundly different from the normal orbital angular momentum. And, probably, the most prominent feature that establishes the seemingly true quantum character of spin is that it cannot be described in terms of the classical dynamics because there is no such classical analogue. Since the main topic that we will discuss in this work involves the concepts of both orbital and spin angular momentum in quantum mechanics and accordingly the application of Schrödinger equation to formulate spin dynamics therefore we now show more details how these two concepts have been introduced and formulated in quantum mechanics. Besides the fundamental concepts, the general results obtained in this section will also be implemented to different applications in later sections of this work. In classical mechanics, the orbital angular momentum $\boldsymbol{L}$ of a particle is defined as $\boldsymbol{L}=\boldsymbol{r}\times\boldsymbol{p}$, where $\boldsymbol{r}$ and $\boldsymbol{p}$ are the position and momentum of the

particle, respectively. In quantum mechanics, however, the orbital angular momentum is interpreted as an operator in which the momentum is defined via a differential operator in the form $\boldsymbol{p} = -i\hbar\nabla$, hence the orbital angular momentum can be rewritten as $\boldsymbol{L} = -i\hbar(\boldsymbol{r}\times\nabla)$. The Cartesian components of the orbital angular momentum are obtained as $L_x = -i\hbar(y\partial/\partial z - z\partial/\partial y)$, $L_y = -i\hbar(z\partial/\partial x - x\partial/\partial z)$, $L_z = -i\hbar(x\partial/\partial y - y\partial/\partial x)$. Even though they do not mutually commute, therefore they cannot be assigned definite values simultaneously, the Cartesian components of the orbital angular momentum commute with the operator $\boldsymbol{L}^2$ and this allows a construction of simultaneous eigenfunctions for $\boldsymbol{L}^2$ and one of the Cartesian components of the orbital angular momentum $\boldsymbol{L}$ [1]. Similarly, the spin angular momentum can be introduced into quantum mechanics as an operator with the same mathematical formulation as the orbital angular momentum, except for the fact that the spin angular momentum does not have a comparable object in classical physics therefore it cannot be depicted as spinning around an axis or associated with some form of motion in space. Since spin angular momentum is considered as a truly quantum mechanical intrinsic property associated with most of elementary particles, it has been suggested that spin must possess some form of intrinsic physical property that is needed to be explained, and one possibility for its explanation is to use a non-local hidden variable theory [2]. The most distinctive property that makes spin different from the normal orbital angular momentum is that spin quantum numbers can take half-integral values. It is also believed that the internal degrees of freedom associated with the spin angular momentum cannot be described mathematically in terms of a wavefunction. In order to incorporate the spin angular momentum of a quantum particle into quantum mechanics, Dirac developed a relativistic wave equation that admits solutions in the form of multiple-component wavefunctions as $\gamma^\mu\partial_\mu\psi = -im\psi$. Dirac equation is a system of complex linear first order partial differential equations [3]. Even though Dirac equation has been regarded as a quantum wave equation that is used to describe spinor fields of half-integral values, we have shown that in fact Dirac equation, as well as Maxwell field equations of the electromagnetic field, can be derived from a system of linear first order partial differential equations therefore Dirac equation can be used to describe classical fields when it is rewritten as a system of real equations. In fact, we have also shown that many fundamental potential forms that involve weak and strong interactions can be deduced from Dirac equation [4]. To avoid confusion, in this work whenever we mention Maxwell or Dirac equation we mean a Maxwell-like or Dirac-like equation that can be derived from a system of linear first order partial differential equations.

Now, contrary to the belief that the spin angular momentum cannot be described mathematically in terms of a wavefunction, we will show in Section 4 that spin angular momentum with half-integral values can be formulated similar to the case of orbital angular momentum by simply using Schrödinger equation in quantum mechanics. Since the following method and results will be used in

later sections therefore we need to give a brief account how the Schrödinger equation is applied to the hydrogen atom. Normally Schrödinger equation is written as a single wave equation with respect to a particular coordinate system that describes a spinless particle with no intrinsic properties, except for their charge and mass. The time-independent Schrödinger wave equation for a point-like particle of mass m and charge q moving in a potential $V(\boldsymbol{r})$ in three-dimensional Euclidean space R^3 is given as follows

$$-\frac{\hbar^2}{2\mu}\nabla^2\psi(\boldsymbol{r})+V(\boldsymbol{r})\psi(\boldsymbol{r})=E\psi(\boldsymbol{r}) \tag{1}$$

where μ is the reduced mass in the centre of mass coordinate system [5]. In the three-dimensional continuum, if the potential $V(\boldsymbol{r})$ is spherically symmetric, then Equation (1) can be written in the spherical polar coordinates (r,θ,ϕ) as [6]

$$-\frac{\hbar^2}{2\mu}\left(\frac{1}{r^2}\frac{\partial}{\partial r}\left(r^2\frac{\partial}{\partial r}\right)-\frac{\boldsymbol{L}^2}{r^2}\right)\psi(\boldsymbol{r})+V(\boldsymbol{r})\psi(\boldsymbol{r})=E\psi(\boldsymbol{r}) \tag{2}$$

where the orbital angular momentum operator $\boldsymbol{L}^2$ is given by

$$\boldsymbol{L}^2=-\hbar^2\left(\frac{1}{\sin\theta}\frac{\partial}{\partial\theta}\left(\sin\theta\frac{\partial}{\partial\theta}\right)+\frac{1}{\sin^2\theta}\frac{\partial^2}{\partial^2\phi}\right) \tag{3}$$

Solutions to Equation (2) can be found using the separable form $\psi_{El}(\boldsymbol{r})=R_{El}(r)Y_{lm}(\theta,\phi)$ where R_{El} is radial function and Y_{lm} is spherical harmonic. Then the wave equation given in Equation (2) is reduced to the following system of equations

$$\boldsymbol{L}^2Y_{lm}(\theta,\phi)=l(l+1)\hbar^2Y_{lm}(\theta,\phi) \tag{4}$$

$$\left(-\frac{\hbar^2}{2\mu}\left(\frac{\mathrm{d}^2}{\mathrm{d}r^2}+\frac{2}{r}\frac{\mathrm{d}}{\mathrm{d}r}\right)+\frac{l(l+1)\hbar^2}{2Dr^2}+V(r)\right)R_{El}(r)=ER_{El}(r) \tag{5}$$

In the case of the hydrogen atom for which $V(r)=Zq^2/4\pi\varepsilon_0 r$, solutions to Equations (4) and (5) can be obtained, respectively, as follows

$$Y_{lm}(\theta,\phi)=(-1)^m\left(\frac{(2l+1)(l-m)}{4\pi(l+m)!}\right)^{\frac{1}{2}}P_l^m(\cos\theta)\mathrm{e}^{im\phi} \tag{6}$$

$$R_{nl}(r)=-C\mathrm{e}^{-\rho/2}\rho^l L_{n+l}^{2l+1}(\rho) \tag{7}$$

where $P_l^m(\cos\theta)$ is Legendre functions, $\rho=\left(-8DE/\hbar^2\right)^{1/2}r$, $L_{n+l}^{2l+1}(\rho)$ is the associated Laguerre polynomial. The bound state energy spectrum is also found as

$$E_n=-\frac{\mu}{2\hbar^2}\left(\frac{Zq^2}{4\pi\varepsilon_0}\right)^2\frac{1}{n^2} \tag{8}$$

According to the present formulation of quantum mechanics, the energy difference between the two levels of the energy spectrum equals the energy of the photon that is emitted or absorbed by a hydrogen atom, and the radiating

process is due to an instantaneous quantum transition of the corresponding electron that interacts with the photon. We will show in Section 5 that the process of radiation of photons may also be accompanied by an intrinsic dynamics similar to the process of spin dynamics that we will discuss in Section 4. However, we will also show that such spin dynamics can be observable only if the photon has an inertial mass.

As being shown in Section 4, the most important feature that relates to our discussion on the formulation of spin dynamics by using Schrödinger equation is the quantisation of an orbital angular momentum in a two-dimensional Euclidean space. In spherical coordinates (r,θ,ϕ), simultaneously to the equation given in Equation (4), the operator L_z and its corresponding normalised eigenfunctions $\Phi(\phi)$ can be found as follows

$$L_z = -i\hbar\frac{\partial}{\partial\phi},\ \Phi_m(\phi) = \frac{1}{\sqrt{2\pi}}\mathrm{e}^{im\phi} \tag{9}$$

where $m = -l, -l+1, \cdots, l-1, l$ with the quantum numbers l are integers. As a consequence, the quantum number m can only take integer values. However, there are many physical phenomena that involve the magnetic moment of a quantum particle cannot be explained using the quantisation of orbital angular momentum with integer values. For example, in order to interpret the Stern-Gerlach experiment the quantum number m must be assumed to take half-integral values, and this is inconsistent with other experimental results that can be explained by assuming integral values for the orbital angular momentum. Therefore, the spin angular momentum operator $\boldsymbol{S}$ was introduced similar to Equation (4) for the orbital angular momentum as $S^2\chi_{sm_s} = s(s+1)\hbar^2\chi_{sm_s}$, in which the spin angular momentum s takes half-integral values. However, unlike the orbital angular momentum, the spin angular momentum has no direct relationship with the coordinates that define the coordinate system for mathematical investigations.

3. Formulating Two-Dimensional Dynamics Using Dirac Equation

In this section we show that the spin dynamics of a quantum particle may also have a classical character by recalling our work on the fluid state of Dirac quantum particles that Dirac equation can in fact be derived from a general system of linear first order partial differential equations, and from Dirac equation we can obtain a physical structure for quantum particles that can be endowed with a spin angular momentum that takes half-integral values [7]. As a general remark, it should be mentioned here that normally in formulating physical theories in classical physics we either apply purely mathematical equations into physical problems or formulate mathematical equations according to dynamical laws established from experiments. It may be said that this mutual relationship between mathematics and physics was initiated by Newton's work on classical mechanics when he himself invented the mathematics of differential calculus to describe the

dynamics of natural laws in his three books on the mathematical principles of natural philosophy [8]. It has been known that Maxwell field equations of the electromagnetic field were derived mainly from experimental laws. On the other hand, it can be said that essentially Dirac derived his relativistic equation to describe the dynamics of quantum particles from an established physical law which is a consequence of Einstein's theory of special relativity [9]. In general, a common method in mathematical physics is to apply the same differential equation, such as Laplace or Poisson's equation, into different physical systems, and by following this method we have shown in our works on formulating Maxwell and Dirac equations that both Maxwell and Dirac equations can be derived from an established system of mathematical equations instead of experimental laws or established physical theories [10] [11]. The established system of mathematical equations in our formulation is a general system of linear first order partial differential equations given as follows

$$\sum_{i=1}^{n}\sum_{j=1}^{n} a_{ij}^{r}\frac{\partial \psi_i}{\partial x_j} = k_1\sum_{l=1}^{n} b_l^r \psi_l + k_2 c^r, \quad r = 1,2,\cdots,n \tag{10}$$

The system of equations given in Equation (10) can be rewritten in a matrix form as

$$\left(\sum_{i=1}^{n} A_i \frac{\partial}{\partial x_i}\right)\psi = k_1\sigma\psi + k_2 J \tag{11}$$

where $\psi = \left(\psi_1,\psi_2,\cdots,\psi_n\right)^{\mathrm{T}}$, $\partial\psi/\partial x_i = \left(\partial\psi_1/\partial x_i, \partial\psi_2/\partial x_i,\cdots,\partial\psi_n/\partial x_i\right)^{\mathrm{T}}$, A_i, σ and J are matrices representing the quantities a_{ij}^k, b_l^r and c^r, and k_1 and k_2 are undetermined constants. Now, if we apply the operator $\sum_{i=1}^{n} A_i\,\partial/\partial x_i$ on the left on both sides of Equation (11) then we obtain

$$\left(\sum_{i=1}^{n} A_i \frac{\partial}{\partial x_i}\right)\left(\sum_{j=1}^{n} A_j \frac{\partial}{\partial x_j}\right)\psi = \left(\sum_{i=1}^{n} A_i \frac{\partial}{\partial x_i}\right)\left(k_1\sigma\psi + k_2 J\right) \tag{12}$$

If we assume further that the coefficients a_{ij}^k and b_l^r are constants and $A_i\sigma = \sigma A_i$, then Equation (12) can be rewritten in the following form

$$\left(\sum_{i=1}^{n} {A_i}^2 \frac{\partial^2}{\partial x_i^2} + \sum_{i=1}^{n}\sum_{j>i}^{n}\left(A_iA_j + A_jA_i\right)\frac{\partial^2}{\partial x_i\partial x_j}\right)\psi = k_1^2\sigma^2\psi + k_1k_2\sigma J + k_2\sum_{i=1}^{n} A_i\frac{\partial J}{\partial x_i} \tag{13}$$

In order for the above systems of partial differential equations to be used to describe physical phenomena, the matrices A_i must be determined. It is observed that in order to obtain Maxwell and Dirac equations the matrices A_i must take a form so that Equation (13) reduces to the following equation

$$\left(\sum_{i=1}^{n} {A_i}^2 \frac{\partial^2}{\partial x_i^2}\right)\psi = k_1^2\sigma^2\psi + k_1k_2\sigma J + k_2\sum_{i=1}^{n} A_i\frac{\partial J}{\partial x_i} \tag{14}$$

To obtain an equation similar to Dirac equation for free quantum particles, we identify the matrices A_i with the gamma matrices γ_i given as

$$\gamma_1 = \begin{pmatrix} 1 & 0 & 0 & 0 \\ 0 & 1 & 0 & 0 \\ 0 & 0 & -1 & 0 \\ 0 & 0 & 0 & -1 \end{pmatrix},\ \gamma_2 = \begin{pmatrix} 0 & 0 & 0 & 1 \\ 0 & 0 & 1 & 0 \\ 0 & -1 & 0 & 0 \\ -1 & 0 & 0 & 0 \end{pmatrix}$$
$$\gamma_3 = \begin{pmatrix} 0 & 0 & 0 & -i \\ 0 & 0 & i & 0 \\ 0 & i & 0 & 0 \\ -i & 0 & 0 & 0 \end{pmatrix},\ \gamma_4 = \begin{pmatrix} 0 & 0 & 1 & 0 \\ 0 & 0 & 0 & -1 \\ -1 & 0 & 0 & 0 \\ 0 & 1 & 0 & 0 \end{pmatrix} \tag{15}$$

If we set $k_1\sigma = -im$ and $k_2 J = 0$ then Equation (11) reduces to Dirac equation [12]

$$\left(i\gamma^\mu \partial_\mu - m\right)\psi = 0 \tag{16}$$

For references and to show that Maxwell field equations of the electromagnetic field can also be derived from a system of linear first order partial differential equations, in the appendix we give a detailed formulation of Maxwell field equations with specified forms of the matrices A_i. Now, by expanding Equation (16) using Equation (15), we obtain

$$-\frac{\partial \psi_1}{\partial t} - im\psi_1 = \left(\frac{\partial}{\partial x} - i\frac{\partial}{\partial y}\right)\psi_4 + \frac{\partial \psi_3}{\partial z} \tag{17}$$

$$-\frac{\partial \psi_2}{\partial t} - im\psi_2 = \left(\frac{\partial}{\partial x} + i\frac{\partial}{\partial y}\right)\psi_3 - \frac{\partial \psi_4}{\partial z} \tag{18}$$

$$\frac{\partial \psi_3}{\partial t} - im\psi_3 = \left(-\frac{\partial}{\partial x} + i\frac{\partial}{\partial y}\right)\psi_2 - \frac{\partial \psi_1}{\partial z} \tag{19}$$

$$\frac{\partial \psi_4}{\partial t} - im\psi_4 = \left(-\frac{\partial}{\partial x} - i\frac{\partial}{\partial y}\right)\psi_1 + \frac{\partial \psi_2}{\partial z} \tag{20}$$

From the form of the field equations given in Equations (17-20), we may interpret that the change of the field (ψ_1, ψ_2) with respect to time generates the field (ψ_3, ψ_4), similar to the case of Maxwell field equations in which the change of the electric field generates the magnetic field. With this observation it may be suggested that, like the Maxwell electromagnetic field, which is composed of two essentially different physical fields, the Dirac field of massive particles may also be viewed as being composed of two different physical fields, namely the field (ψ_1, ψ_2) and the field (ψ_3, ψ_4). The similarity between Maxwell field equations and Dirac field equations can be carried further by showing that it is possible to reformulate Dirac equation as a system of real equations. When we formulate Maxwell field equations from a system of linear first order partial differential equations we rewrite the original Maxwell field equations from a vector form to a system of first order partial differential equations by equating the corresponding terms of the vectorial equations. Now, since, in principle, a complex quantity is equivalent to a vector quantity therefore in order to form a system of real equations from Dirac complex field equations we equate the real parts with the real parts and the imaginary parts with the imaginary

parts. In this case Dirac equation given in Equations (17-20) can be rewritten as a system of real equations as follows

$$-\frac{\partial \psi_1}{\partial t}=\frac{\partial \psi_4}{\partial x}+\frac{\partial \psi_3}{\partial z},\ -\frac{\partial \psi_2}{\partial t}=\frac{\partial \psi_3}{\partial x}-\frac{\partial \psi_4}{\partial z} \tag{21}$$

$$-\frac{\partial \psi_3}{\partial t}=\frac{\partial \psi_2}{\partial x}+\frac{\partial \psi_1}{\partial z},\ -\frac{\partial \psi_4}{\partial t}=\frac{\partial \psi_1}{\partial x}-\frac{\partial \psi_2}{\partial z} \tag{22}$$

$$\frac{\partial \psi_4}{\partial y}=m\psi_1,\ \frac{\partial \psi_3}{\partial y}=-m\psi_2,\ \frac{\partial \psi_2}{\partial y}=-m\psi_3,\ \frac{\partial \psi_1}{\partial y}=m\psi_4 \tag{23}$$

If the wavefunction $\psi=\left(\psi_1,\psi_2,\psi_3,\psi_4\right)^{\mathrm{T}}$ satisfies Dirac field equations given in Equations (21-23) then we can derive the following system of equations for all components

$$\frac{\partial^2 \psi_i}{\partial^2 y}-m^2\psi_i=0 \tag{24}$$

$$\frac{\partial^2 \psi_i}{\partial t^2}-\frac{\partial^2 \psi_i}{\partial x^2}-\frac{\partial^2 \psi_i}{\partial z^2}=0 \tag{25}$$

Solutions to Equation (24) are

$$\psi_i=c_{1i}\left(x,z\right)\mathrm{e}^{my}+c_{2i}\left(x,z\right)\mathrm{e}^{-my} \tag{26}$$

where c_{1i} and c_{2i} are undetermined functions of $\left(x,z\right)$. The solutions given in Equation (26) give a distribution of a physical quantity along the *y*-axis. On the other hand, Equation (25) can be used to describe the dynamics, for example, of a vibrating membrane in the $\left(x,z\right)$-plane. If the membrane is a circular membrane of radius *a* then the domain *D* is given as $D=\left\{x^2+z^2<a^2\right\}$. In the polar coordinates given in terms of the Cartesian coordinates $\left(x,y\right)$ as $x=r\cos\theta$, $z=r\sin\theta$, the two-dimensional wave equation given in Equation (25) becomes

$$\frac{1}{c^2}\frac{\partial^2 \psi}{\partial t^2}-\frac{\partial^2 \psi}{\partial r^2}-\frac{1}{r}\frac{\partial \psi}{\partial r}-\frac{1}{r^2}\frac{\partial^2 \psi}{\partial \theta^2}=0 \tag{27}$$

The general solution to Equation (27) for the vibrating circular membrane with the condition $\psi=0$ on the boundary of *D* can be found as [13]

$$\begin{aligned}\psi\left(r,\theta,t\right)&=\sum_{m=1}^{\infty}J_0\left(\sqrt{\lambda_{0m}}r\right)\left(C_{0m}\cos\sqrt{\lambda_{0m}}ct+D_{0m}\sin\sqrt{\lambda_{0m}}ct\right)\\&+\sum_{m,n=1}^{\infty}J_n\left(\sqrt{\lambda_{nm}}r\right)\left(A_{nm}\cos n\theta+B_{nm}\sin n\theta\right)\left(\left(C_{nm}\cos\sqrt{\lambda_{nm}}ct+D_{nm}\sin\sqrt{\lambda_{nm}}ct\right)\right)\end{aligned} \tag{28}$$

where $J_n\left(\sqrt{\lambda_{nm}}r\right)$ is the Bessel function of order *n* and the quantities A_{nm}, B_{nm}, C_{nm} and D_{nm} can be specified by the initial and boundary conditions. It is also observed that at each moment of time the vibrating membrane appears as a 2D differentiable manifold which is a geometric object whose geometric structure can be constructed using the wavefunction given in Equation (28). Even though elementary particles may have the geometric and topological structures of a 3D differentiable manifold, it is seen from the above descriptions via the Schrödinger wave equation and Dirac equation that they appear as 3D physical

objects embedded in three-dimensional Euclidean space. Interestingly, we have shown that the solution given in Equation (28) can be used to describe a standing wave in a fluid due to the motion of two waves in opposite directions. At its steady state in which the system is time-independent, the system of equations given in Equations (21-22) reduces to the following system of equations

$$\frac{\partial \psi_2}{\partial x}+\frac{\partial \psi_1}{\partial z}=0,\ \frac{\partial \psi_1}{\partial x}-\frac{\partial \psi_2}{\partial z}=0 \tag{29}$$

$$\frac{\partial \psi_4}{\partial x}+\frac{\partial \psi_3}{\partial z}=0,\ \frac{\partial \psi_3}{\partial x}-\frac{\partial \psi_4}{\partial z}=0 \tag{30}$$

In this case Dirac equation for steady states consisting of the field (ψ_1,ψ_2) and the field (ψ_3,ψ_4) satisfies the Cauchy-Riemann equations in the (x,z) -plane. We have shown in our work on the fluid state of Dirac quantum particles that it is possible to consider Dirac quantum particles as physical systems which exist in a two-dimensional fluid state as defined in the classical fluid dynamics. In the next section we will show that when Schrödinger wave equation is applied into the dynamics of a physical system in two-dimensional space the angular momentum associated with the system can take half-integral values which may be identified with the intrinsic spin angular momentum of a quantum particle. The results also show that the spin angular momentum can also be introduced through a coordinate system, similar to that of the orbital angular momentum.

4. Formulating Intrinsic Spin Dynamics Using Schrödinger Equation

As we have discussed in the previous sections that the profound difference between orbital angular momentum and spin angular momentum is that the former can be associated with the motion of a physical object in space but the latter cannot. This difference has led to another profound difference in the formulation of their corresponding dynamics in which an orbital angular momentum can be described by using a coordinate system but a spin angular momentum cannot. In this section we show that it is possible to treat spin angular momentum in the same manner as orbital angular momentum by introducing a coordinate system to describe spin angular momentum. However, it is obvious that the coordinate system that is used to describe a spin angular momentum must be an intrinsic coordinate system which is independent of the coordinate system that is used to describe an orbital angular momentum. Therefore, instead of introducing a spin operator, we introduce a differential operator that depends on an intrinsic coordinate system and can be used to formulate a spin dynamics. Furthermore, since spin angular momentum and orbital angular momentum are similar in nature therefore it is possible to suggest that the spin operator in the intrinsic coordinate system should also have similar form to that of the orbital angular momentum operator formulated in quantum mechanics. From this perspective we now write a Schrödinger wave equation that is used to describe both the orbital and spin dynamics as follows

$$-\frac{\hbar^2}{2\mu}\nabla^2\Psi(\boldsymbol{r},\boldsymbol{r}_s)+V(\boldsymbol{r})\Psi(\boldsymbol{r},\boldsymbol{r}_s)-\frac{\hbar^2}{2\mu_s}\nabla_s^2\Psi(\boldsymbol{r},\boldsymbol{r}_s)+V_s(\boldsymbol{r}_s)\Psi(\boldsymbol{r},\boldsymbol{r}_s) = E\Psi(\boldsymbol{r},\boldsymbol{r}_s) \tag{31}$$

The quantity μ can be identified with a reduced mass. However, since we are treating spin angular momentum as a particular case of angular momentum therefore we retain the Planck constant and the quantity μ_s also retains the dimension of mass. We call the quantity μ_s an intrinsic mass and it could be related to the curvature that determines the differential geometric and topological structure of a quantum particle, as in the case of Bohr model, or charge. On the other hand, while the quantity $V(\boldsymbol{r})$ can be identified with a normal potential, such as Coulomb potential, the quantity $V_s(\boldsymbol{r}_s)$ represents an intrinsic potential that depends on intrinsic physical properties associated with the spin angular momentum of a quantum particle. Since the two dynamics are independent, the wave equation given in Equation (31) is separable and the total wavefunction $\Psi(\boldsymbol{r},\boldsymbol{r}_s)$ can be written as a product of two wavefunctions as $\Psi(\boldsymbol{r},\boldsymbol{r}_s)=\psi(\boldsymbol{r})\chi(\boldsymbol{r}_s)$. Then Equation (31) is separated into two equations as follows

$$-\frac{\hbar^2}{2\mu}\nabla^2\psi(\boldsymbol{r})+V(\boldsymbol{r})\psi(\boldsymbol{r}) = E_0\psi(\boldsymbol{r}) \tag{32}$$

$$-\frac{\hbar^2}{2\mu_s}\nabla_s^2\chi(\boldsymbol{r}_s)+V_s(\boldsymbol{r}_s)\chi(\boldsymbol{r}_s) = E_1\chi(\boldsymbol{r}_s) \tag{33}$$

where $E_0+E_1=E$.

Now, we consider the particular case in which the Schrödinger equation given in Equation (32) describes the dynamics of a hydrogen atom and the Schrödinger equation given in Equation (33) describes the spin dynamics of the electron of the hydrogen atom. In this case the wavefunctions and the corresponding energy spectrum for Equation (32) have been obtained and given in Section 2 therefore we only need to show how half-integral values for the spin angular momentum can be obtained from Equation (33). In fact we have shown in our previous works that elementary particles possess an intrinsic angular momentum that can take half-integral values by considering Schrödinger wave equation in two-dimensional Euclidean space in which a quantum particle can be viewed as a planar system whose configuration space is multiply connected [14] [15] [16]. If we also assume that the potential $V_s(\boldsymbol{r}_s)$ that holds the quantum particle together has the form $V_s(\boldsymbol{r}_s)=A_s/r_s$, where A_s is a physical constant that is needed to be determined, then using the planar polar coordinates in an intrinsic two-dimensional space, the Schrödinger wave equation given in Equation (33) takes the form

$$-\frac{\hbar^2}{2\mu_s}\left[\frac{1}{r}\frac{\partial}{\partial r}\left(r\frac{\partial}{\partial r}\right)+\frac{1}{r^2}\frac{\partial^2}{\partial\phi^2}\right]\chi(r,\phi)-\frac{A_s}{r}\chi(r,\phi) = E_1\chi(r,\phi) \tag{34}$$

For simplicity in Equation (34) we have written r instead of r_s as indicated

in Equation (33). Solutions of the form $\chi(r,\phi)=R(r)\Phi(\phi)$ reduce Equation (34) to two separate equations for the functions $\Phi(\phi)$ and $R(r)$ as follows

$$\frac{\mathrm{d}^2\Phi}{\mathrm{d}\phi^2}+m_s^2\Phi=0 \tag{35}$$

$$\frac{\mathrm{d}^2R}{\mathrm{d}r^2}+\frac{1}{r}\frac{\mathrm{d}R}{\mathrm{d}r}-\frac{m_s^2}{r^2}R+\frac{2\mu_s}{\hbar^2}\left(\frac{A_s}{r}+E_1\right)R=0 \tag{36}$$

where m_s is identified as the intrinsic angular momentum of the quantum particle. Equation (35) has solutions of the form

$$\Phi(\phi)=C\mathrm{e}^{im_s\phi} \tag{37}$$

where C is a constant. Normally, the intrinsic angular momentum m_s must take integral values for the single-valuedness condition to be satisfied. However, if we consider the configuration space of the quantum particle to be multiply connected and the polar coordinates have singularity at the origin then the use of multivalued wavefunctions is allowable. As shown below, in this case, the intrinsic angular momentum m_s can take half-integral values. If we define, for the case $E_1<0$,

$$\rho=\left(\frac{8\mu_s(-E_1)}{\hbar^2}\right)^{1/2}r,\quad \lambda=\left(\frac{A_s\mu_s}{2\hbar^2(-E_1)}\right)^{1/2} \tag{38}$$

then Equation (36) can be re-written in the following form

$$\frac{\mathrm{d}^2R}{\mathrm{d}\rho^2}+\frac{1}{\rho}\frac{\mathrm{d}R}{\mathrm{d}\rho}-\frac{m_s^2}{\rho^2}R+\frac{\lambda}{\rho}R-\frac{1}{4}R=0 \tag{39}$$

If we seek solutions for $R(\rho)$ in the form $R(\rho)=\exp(-\rho/2)\rho^{m_s}S(\rho)$ then we obtain the following differential equation for the function $S(\rho)$

$$\frac{\mathrm{d}^2S}{\mathrm{d}\rho^2}+\left(\frac{2m_s+1}{\rho}-1\right)\frac{\mathrm{d}S}{\mathrm{d}\rho}+\left(\frac{\lambda-m_s-\frac{1}{2}}{\rho}\right)S=0 \tag{40}$$

Equation (40) can be solved by a series expansion of $S(\rho)$ as $S(\rho)=\sum_{n=0}^{\infty}a_{n_s}\rho^{n_s}$ with the coefficients a_n satisfying the recursion relation

$$a_{n_s+1}=\frac{n_s+m_s+\frac{1}{2}-\lambda}{(n_s+1)(n_s+2m_s+1)}a_{n_s} \tag{41}$$

The energy spectrum E_1 obtained from Equation (38) can be written explicitly as follows

$$E_1=-\frac{A_s\mu_s}{2\hbar^2\left(n_s+m_s+\frac{1}{2}\right)^2} \tag{42}$$

Even though it is not possible to specify the actual values of the intrinsic angular momentum m_s, however, if the result given in Equation (42) can also be

applied to the hydrogen-like atom in two-dimensional physical system similar to Bohr model of the hydrogen atom then the intrinsic angular momentum m_s must take half-integral values. For the case of the hydrogen atom then the total energy spectrum can be found as the sum of two energy spectra given in Equations (8) and (42) as

$$E\left(n,n_s,m_s\right)=-\frac{\mu}{2\hbar^2}\left(\frac{Zq^2}{4\pi\varepsilon_0}\right)^2\frac{1}{n^2}-\frac{A_s\mu_s}{2\hbar^2\left(n_s+m_s+\frac{1}{2}\right)^2} \tag{43}$$

It is seen that the total energy spectrum has a fine structure depending on the intrinsic quantum numbers n_s and m_s. Furthermore, the total energy spectrum also depends on the undetermined physical quantities μ_s and A_s that define the intrinsic properties of a quantum particle, which is the electron in this case. Without restriction, the quantity μ_s can take zero, positive or negative values. Then, we can have three different levels of energy as follows

$$\mu_s=0,\quad E\left(n,n_s,m_s\right)=-\frac{\mu}{2\hbar^2}\left(\frac{Zq^2}{4\pi\varepsilon_0}\right)^2\frac{1}{n^2} \tag{44}$$

$$\mu_s>0,\quad n_s=0,\quad m_s=\frac{1}{2},\quad E\left(n,n_s,m_s\right)=-\frac{\mu}{2\hbar^2}\left(\frac{Zq^2}{4\pi\varepsilon_0}\right)^2\frac{1}{n^2}-\frac{A_s\mu_s}{2\hbar^2} \tag{45}$$

$$\mu_s<0,\quad n_s=1,\quad m_s=-\frac{1}{2},\quad E\left(n,n_s,m_s\right)=-\frac{\mu}{2\hbar^2}\left(\frac{Zq^2}{4\pi\varepsilon_0}\right)^2\frac{1}{n^2}+\frac{A_s\left|\mu_s\right|}{2\hbar^2} \tag{46}$$

If we assume the splitting energy is the Zeeman effect caused by the interaction between the magnetic moment associated with the spin of the electron and an external magnetic field B, which results in a magnetic potential energy of $U=\pm g\mu_B B/2$, where g is the electron g-factor and $\mu_B=e\hbar/2m_e$ is the Bohr magneton, then the quantity A_s can be determined by the following identifying relation

$$\frac{A_s\left|\mu_s\right|}{2\hbar^2}=\frac{1}{2}g\mu_B B=\frac{ge\hbar}{4m_e}B \tag{47}$$

As shown in **Figure 1**, the splitting of energy levels due to the intrinsic dynamics is similar to the Zeeman effect with the energy difference of $\Delta U=g\mu_B B$.

Furthermore, if we also identify the intrinsic mass with the inertial mass of the electron, $\left|\mu_s\right|=m_e$, then the quantity A_s can be determined by all known physical quantities as

$$A_s=\frac{ge\hbar^3 B}{2m_e^2} \tag{48}$$

The quantity A_s depends not only on the intrinsic properties associated with the electron but also on the external magnetic field B. This result shows that, unlike the elementary charge, the intrinsic quantity A_s is a dependent property of a quantum particle which changes its magnitude when the particle interacts with

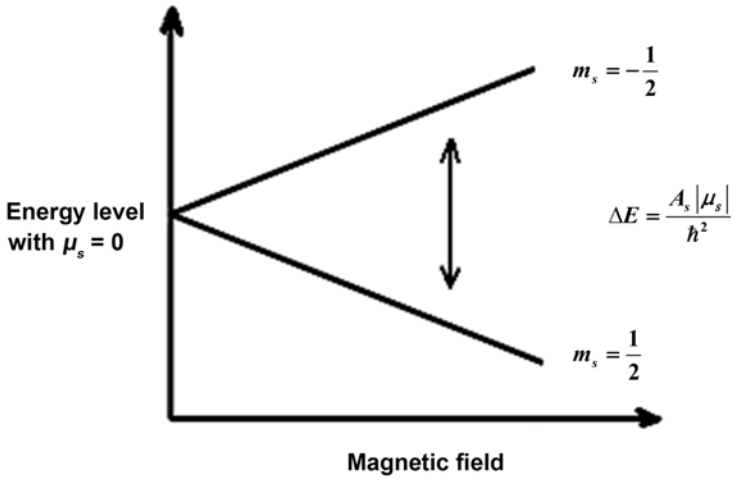

Figure 1. Splitting of energy levels by intrinsic spin dynamics.

an external field. The dependence of quantity A_s on an external field is similar to the case of the inertial mass of an elementary particle that depends on the speed of the particle relative to a coordinate system formulated in Einstein's special relativity as $m = m_0 \big/ \sqrt{1 - v^2/c^2}$. It is interesting to mention here that in fact we have shown in our work on the fluid state of an electromagnetic field that the electric field and the magnetic field can also be identified as velocity fields of a fluid [17].

5. A Generalised Formulation of Intrinsic Dynamics Using Schrödinger Equation

From our discussion of the possibility to describe the spin angular momentum of a quantum particle as an intrinsic dynamics using the Schrödinger wave equation, we may consider further extension by generalising the equation given in Equation (31) to a more general form so that it can be used to describe other intrinsic dynamics that associate with a quantum particle, such as when a hydrogen atom absorbs a photon, the photon may be considered to be correlated with the electron and accordingly behaves as an intrinsic dynamics of the electron. A general equation that include possible intrinsic dynamics associated with an elementary particle can be written as

$$\begin{aligned} &-\frac{\hbar^2}{2\mu}\nabla^2\Psi\left(\boldsymbol{r},\boldsymbol{r}_1,\cdots,\boldsymbol{r}_n\right)+V\left(r\right)\Psi\left(\boldsymbol{r},\boldsymbol{r}_1,\cdots,\boldsymbol{r}_n\right) \\ &+\sum_{s=1}^{N}\left(-\frac{\hbar^2}{2\mu_s}\nabla_s^2\Psi\left(\boldsymbol{r},\boldsymbol{r}_1,\cdots,\boldsymbol{r}_n\right)+V_s\left(\boldsymbol{r}_s\right)\Psi\left(\boldsymbol{r},\boldsymbol{r}_1,\cdots,\boldsymbol{r}_n\right)\right) \\ &=E\Psi\left(\boldsymbol{r},\boldsymbol{r}_1,\cdots,\boldsymbol{r}_n\right) \end{aligned} \tag{49}$$

where each potential $V_s\left(\boldsymbol{r}_s\right)$ is needed to be determined for a particular dynamics associated with the quantum particle under investigation. Even though the quantities m_s have the dimension of mass they should be considered as parameters of the equation because they are related to the intrinsic dynamics

that must be determined based on the characteristics of the motion under consideration. If all intrinsic dynamics are independent then Equation (49) can be separated into a system of equations as follows

$$-\frac{\hbar^2}{2\mu}\nabla^2\psi(\boldsymbol{r})+V(\boldsymbol{r})\psi(\boldsymbol{r})=E_0\psi(\boldsymbol{r}) \tag{50}$$

$$-\frac{\hbar^2}{2\mu_1}\nabla_1^2\chi(\boldsymbol{r}_1)+V_1(\boldsymbol{r}_1)\chi(\boldsymbol{r}_1)=E_1\chi(\boldsymbol{r}_1) \tag{51}$$

$$\vdots$$

$$-\frac{\hbar^2}{2\mu_N}\nabla_N^2\chi(\boldsymbol{r}_N)+V_N(\boldsymbol{r}_N)\chi(\boldsymbol{r}_N)=E_N\chi(\boldsymbol{r}_N) \tag{52}$$

where $E_1+E_2+\cdots+E_N=E$. For example, if we assume that there are N_1 two-dimensional and N_2 three-dimensional intrinsic dynamics so that $N_1+N_2=N$, and all intrinsic dynamics have the intrinsic potentials of the form $V_s(\boldsymbol{r}_s)=A_s/r_s$ then using Equations (8) and (42) we would obtain an expression for the total energy spectrum as

$$E(n,n_s,m_s)=-\frac{\mu}{2\hbar^2}\left(\frac{Zq^2}{4\pi\varepsilon_0}\right)^2\frac{1}{n^2}-\sum_{s=1}^{N_1}\frac{A_s^2\mu_s}{2\hbar^2\left(n_s+m_s+\frac{1}{2}\right)^2}-\sum_{s=1}^{N_2}\frac{A_s^2\mu_s}{2\hbar^2n_s^2} \tag{53}$$

As an example for the case of a three-dimensional intrinsic dynamics, let us consider an intrinsic dynamics that can be described as a spin dynamics of a photon when it is absorbed and then emitted from a hydrogen atom. If the photon exhibits a three-dimensional intrinsic dynamics then we would obtain not only the normal three-dimensional Schrödinger wave equation for the hydrogen atom but also an intrinsic three-dimensional Schrödinger wave equation for the photon, similar to the system of equations given in Equations (32) and (33). In this case the total energy spectrum can be found as

$$E(n,n_s)=-\frac{\mu}{2\hbar^2}\left(\frac{Zq^2}{4\pi\varepsilon_0}\right)^2\frac{1}{n^2}-\frac{A_s^2\mu_s}{2\hbar^2n_s^2} \tag{54}$$

When the electron of the hydrogen atom at the energy level n absorbs a photon and moves to a higher energy level n', we may suggest that the photon also changes its energy levels from the level n_s to the level n_s'. We then obtain the new total energy level

$$E(n',n_s')=-\frac{\mu}{2\hbar^2}\left(\frac{Zq^2}{4\pi\varepsilon_0}\right)^2\frac{1}{(n')^2}-\frac{A_s^2\mu_s}{2\hbar^2(n_s')^2} \tag{55}$$

If we also assume that the energy difference $E(n',n_s')-E(n,n_s)$ equals the Planck energy $h\nu$ then we obtain

$$h\nu=\frac{\mu}{2\hbar^2}\left(\frac{Zq^2}{4\pi\varepsilon_0}\right)^2\left(\frac{1}{n^2}-\frac{1}{(n')^2}\right)+\frac{A_s^2\mu_s}{2\hbar^2}\left(\frac{1}{n_s^2}-\frac{1}{(n_s')^2}\right) \tag{56}$$

The quantity μ_s may be identified with the mass of a photon. It is seen that,

unless the photon is massive, *i.e.* $\mu_s \neq 0$, Equation (56) reduces to the familiar energy spectrum of the hydrogen atom as shown in quantum mechanics.

6. Conclusion

We have shown in this work the possibility to formulate the spin dynamics associated with a quantum particle using Schrödinger equation in quantum mechanics. Contrary to the general assumption that spin dynamics belongs to the domain of relativistic quantum mechanics that cannot be represented by a wavefunction, we have shown that spin dynamics can be formulated by a non-relativistic Schrödinger wave equation by considering possible intrinsic dynamics conferred on quantum particles. Similar to the normal dynamics, intrinsic dynamics can also be expressed in terms of Schrödinger wave equation by using intrinsic coordinates. Since intrinsic coordinates are independent to external coordinates, the total Schrödinger wave equation can be separated into a system of Schrödinger wave equations each of which can be solved separately to obtain exact solutions and their corresponding eigenvalues for the energy. To illustrate, we have applied the formulations to the spin angular momentum for the electron of a hydrogen atom and shown that the quantum numbers associated with the spin angular momentum can take half-integral values, and these results can be used to explain the Stern-Gerlach experiment and other experiments that involve the electron spin resonance. Furthermore, we have also applied the formulation to a possible spin dynamics associated with the radiation of a photon from a hydrogen atom.

Acknowledgements

We would like to thank the reviewers for their constructive comments and we would also like to thank Jane Gao of the administration of JMP for her editorial advice during the preparation of this work.

Conflicts of Interest

The author declares no conflicts of interest regarding the publication of this paper.

References

[1] Bransden, B.H. and Joachain, C.J. (1990) Physics of Atoms and Molecules. Longman Scientific & Technical, New York.

[2] Pons, D.J., Pons, A.D. and Pons, A.J. (2019) *Journal of Modern Physics*, **10**, 835-860. https://doi.org/10.4236/jmp.2019.107056

[3] Dirac, P.A.M. (1928) *Proceedings of the Royal Society A*: *Mathematical, Physical and Engineering Sciences*, **117**, 610-624. https://doi.org/10.1098/rspa.1928.0023

[4] Ho, V.B. (2019) *Journal of Modern Physics*, **10**, 1065-1082. https://doi.org/10.4236/jmp.2019.109069

[5] Schrödinger, E. (1982) Collected Papers on Wave Mechanics. AMS Chelsea Publishing, New York.

[6] Bransden, B.H. and Joachain, C.J. (1989) Introduction to Quantum Mechanics. Longman Scientific & Technical, New York.

[7] Ho, V.B. (2018) *Journal of Modern Physics*, **9**, 2402-2419. https://doi.org/10.4236/jmp.2018.914154

[8] Newton, I. (1687) The Mathematical Principles of Natural Philosophy. Translated into English by Andrew Motte (1846).

[9] Einstein, A. (1952) The Principle of Relativity. Dover Publications, New York.

[10] Ho, V.B. (2017) *International Journal of Physics*, **6**, 105-115. https://doi.org/10.12691/ijp-6-4-2

[11] Ho, V.B. (2018) *Global Journal of Science Frontier Research*, **18**, 37-58.

[12] Thaller, B. (1992) The Dirac Equation. Springer-Verlag, New York.

[13] Strauss, W.A. (1992) Partial Differential Equation. John Wiley & Sons, Inc., New York.

[14] Ho, V.B. (1994) *Journal of Physics A*: *Mathematical and General*, **27**, 6237-6241. https://doi.org/10.1088/0305-4470/27/18/031

[15] Ho, V.B. and Morgan, M.J. (1996) *Journal of Physics A*: *Mathematical and General*, **29**, 1497-1510. https://doi.org/10.1088/0305-4470/29/7/019

[16] Ho, V.B. (1996) Geometrical and Topological Methods in Classical and Quantum Physics. PhD Thesis, Monash University, Clayton.

[17] Ho, V.B. (2018) Fluid State of the Electromagnetic Field.

Appendix

In this appendix we show in details the formulation of Maxwell field equations from the system of linear first order partial differential equations given in Equation (10) of Section 3. The system of equations given in Equation (10) can be written the following matrix form

$$\left(A_0\frac{\partial}{\partial t}+A_1\frac{\partial}{\partial x}+A_2\frac{\partial}{\partial y}+A_3\frac{\partial}{\partial z}\right)\psi=A_4J \tag{1}$$

where $\psi=(\psi_1,\psi_2,\psi_3,\psi_4,\psi_5,\psi_6)^{\mathrm{T}}$, $J=(j_1,j_2,j_3,0,0,0)^{\mathrm{T}}$ and the matrices A_i are given as follows

$$A_0=\begin{pmatrix}-1&0&0&0&0&0\\0&-1&0&0&0&0\\0&0&-1&0&0&0\\0&0&0&1&0&0\\0&0&0&0&1&0\\0&0&0&0&0&1\end{pmatrix},\quad A_1=\begin{pmatrix}0&0&0&0&0&0\\0&0&0&0&0&-1\\0&0&0&0&1&0\\0&0&0&0&0&0\\0&0&-1&0&0&0\\0&1&0&0&0&0\end{pmatrix},$$

$$A_2=\begin{pmatrix}0&0&0&0&0&1\\0&0&0&0&0&0\\0&0&0&-1&0&0\\0&0&1&0&0&0\\0&0&0&0&0&0\\-1&0&0&0&0&0\end{pmatrix},\quad A_3=\begin{pmatrix}0&0&0&0&-1&0\\0&0&0&1&0&0\\0&0&0&0&0&0\\0&-1&0&0&0&0\\1&0&0&0&0&0\\0&0&0&0&0&0\end{pmatrix}, \tag{2}$$

$$A_4=\begin{pmatrix}\mu&0&0&0&0&0\\0&\mu&0&0&0&0\\0&0&\mu&0&0&0\\0&0&0&0&0&0\\0&0&0&0&0&0\\0&0&0&0&0&0\end{pmatrix}$$

The system of equations given in Equation (1) becomes

$$-\frac{\partial\psi_1}{\partial t}+\frac{\partial\psi_6}{\partial y}-\frac{\partial\psi_5}{\partial z}=\mu j_1 \tag{3}$$

$$-\frac{\partial\psi_2}{\partial t}+\frac{\partial\psi_4}{\partial z}-\frac{\partial\psi_6}{\partial x}=\mu j_2 \tag{4}$$

$$-\frac{\partial\psi_3}{\partial t}+\frac{\partial\psi_5}{\partial x}-\frac{\partial\psi_4}{\partial y}=\mu j_3 \tag{5}$$

$$\frac{\partial\psi_4}{\partial t}+\frac{\partial\psi_3}{\partial y}-\frac{\partial\psi_2}{\partial z}=0 \tag{6}$$

$$\frac{\partial\psi_5}{\partial t}+\frac{\partial\psi_1}{\partial z}-\frac{\partial\psi_3}{\partial x}=0 \tag{7}$$

$$\frac{\partial\psi_6}{\partial t}+\frac{\partial\psi_2}{\partial x}-\frac{\partial\psi_1}{\partial y}=0 \tag{8}$$

Using the identification $\boldsymbol{E}=(\psi_1,\psi_2,\psi_3)$ and $\boldsymbol{B}=(\psi_4,\psi_5,\psi_6)$, the above system of equations can be rewritten in the familiar form given in classical electrodynamics as

$$\nabla\cdot\boldsymbol{E}=\frac{\rho_e}{\epsilon} \tag{9}$$

$$\nabla\cdot\boldsymbol{B}=0 \tag{10}$$

$$\nabla\times\boldsymbol{E}+\frac{\partial\boldsymbol{B}}{\partial t}=0 \tag{11}$$

$$\nabla\times\boldsymbol{B}-\epsilon\mu\frac{\partial\boldsymbol{E}}{\partial t}=\mu\boldsymbol{j}_e \tag{12}$$

where the charge density ρ_e and the current density $\boldsymbol{j}_e$ satisfy the conservation law

$$\nabla\cdot\boldsymbol{j}_e+\frac{\partial\rho_e}{\partial t}=0 \tag{13}$$

From the matrices A_i given in Equation (2) we obtain

$$A_0^2=\begin{pmatrix}1&0&0&0&0&0\\0&1&0&0&0&0\\0&0&1&0&0&0\\0&0&0&1&0&0\\0&0&0&0&1&0\\0&0&0&0&0&1\end{pmatrix},\quad A_1^2=\begin{pmatrix}0&0&0&0&0&0\\0&-1&0&0&0&0\\0&0&-1&0&0&0\\0&0&0&0&0&0\\0&0&0&0&-1&0\\0&0&0&0&0&-1\end{pmatrix},$$

$$A_2^2=\begin{pmatrix}-1&0&0&0&0&0\\0&0&0&0&0&0\\0&0&-1&0&0&0\\0&0&0&-1&0&0\\0&0&0&0&0&0\\0&0&0&0&0&-1\end{pmatrix},\quad A_3^2=\begin{pmatrix}-1&0&0&0&0&0\\0&-1&0&0&0&0\\0&0&0&0&0&0\\0&0&0&-1&0&0\\0&0&0&0&-1&0\\0&0&0&0&0&0\end{pmatrix},$$

$$A_4^2=\begin{pmatrix}\mu^2&0&0&0&0&0\\0&\mu^2&0&0&0&0\\0&0&\mu^2&0&0&0\\0&0&0&0&0&0\\0&0&0&0&0&0\\0&0&0&0&0&0\end{pmatrix},\quad A_1A_2+A_2A_1=\begin{pmatrix}0&1&0&0&0&0\\1&0&0&0&0&0\\0&0&0&0&0&0\\0&0&0&0&1&0\\0&0&0&1&0&0\\0&0&0&0&0&0\end{pmatrix}$$

$$A_1A_3+A_3A_1=\begin{pmatrix}0&0&1&0&0&0\\0&0&0&0&0&0\\1&0&0&0&0&0\\0&0&0&0&0&1\\0&0&0&0&0&0\\0&0&0&1&0&0\end{pmatrix},\quad A_2A_3+A_3A_2=\begin{pmatrix}0&0&0&0&0&0\\0&0&1&0&0&0\\0&1&0&0&0&0\\0&0&0&0&0&0\\0&0&0&0&0&1\\0&0&0&0&1&0\end{pmatrix}$$

$$A_0A_i+A_iA_0=0\ \text{ for } i=1,2,3 \tag{14}$$

Now, if we apply the differential operator $\left(A_0\,\partial/\partial t + A_1\,\partial/\partial x + A_2\,\partial/\partial y + A_3\,\partial/\partial z\right)$ to Equation (1) then we arrive at

$$\begin{aligned}
&\left(\begin{pmatrix}1&0&0&0&0&0\\0&1&0&0&0&0\\0&0&1&0&0&0\\0&0&0&1&0&0\\0&0&0&0&1&0\\0&0&0&0&0&1\end{pmatrix}\frac{\partial^2}{\partial t^2}+\begin{pmatrix}0&0&0&0&0&0\\0&-1&0&0&0&0\\0&0&-1&0&0&0\\0&0&0&0&0&0\\0&0&0&0&-1&0\\0&0&0&0&0&-1\end{pmatrix}\frac{\partial^2}{\partial x^2}\right.\\
&+\begin{pmatrix}-1&0&0&0&0&0\\0&0&0&0&0&0\\0&0&-1&0&0&0\\0&0&0&-1&0&0\\0&0&0&0&0&0\\0&0&0&0&0&-1\end{pmatrix}\frac{\partial^2}{\partial y^2}+\begin{pmatrix}-1&0&0&0&0&0\\0&-1&0&0&0&0\\0&0&0&0&0&0\\0&0&0&-1&0&0\\0&0&0&0&-1&0\\0&0&0&0&0&0\end{pmatrix}\frac{\partial^2}{\partial z^2}\\
&+\begin{pmatrix}0&1&0&0&0&0\\1&0&0&0&0&0\\0&0&0&0&0&0\\0&0&0&0&1&0\\0&0&0&1&0&0\\0&0&0&0&0&0\end{pmatrix}\frac{\partial^2}{\partial x\partial y}+\begin{pmatrix}0&0&1&0&0&0\\0&0&0&0&0&0\\1&0&0&0&0&0\\0&0&0&0&0&1\\0&0&0&0&0&0\\0&0&0&1&0&0\end{pmatrix}\frac{\partial^2}{\partial x\partial z}\\
&\left.+\begin{pmatrix}0&0&0&0&0&0\\0&0&1&0&0&0\\0&1&0&0&0&0\\0&0&0&0&0&0\\0&0&0&0&0&1\\0&0&0&0&1&0\end{pmatrix}\frac{\partial^2}{\partial y\partial z}\right)\psi=-\left(\begin{pmatrix}\mu&0&0&0&0&0\\0&\mu&0&0&0&0\\0&0&\mu&0&0&0\\0&0&0&0&0&0\\0&0&0&0&0&0\\0&0&0&0&0&0\end{pmatrix}\frac{\partial}{\partial t}\right)J
\end{aligned}\tag{15}$$

From Equation (15), we obtain the following system of equations for the electric field $\boldsymbol{E}=\left(E_x,E_y,E_z\right)=\left(\psi_1,\psi_2,\psi_3\right)$

$$\frac{\partial^2\psi_1}{\partial t^2}-\frac{\partial^2\psi_1}{\partial y^2}-\frac{\partial^2\psi_1}{\partial z^2}+\frac{\partial}{\partial x}\left(\frac{\partial\psi_2}{\partial y}+\frac{\partial\psi_3}{\partial z}\right)=-\mu\frac{\partial j_1}{\partial t}\tag{16}$$

$$\frac{\partial^2\psi_2}{\partial t^2}-\frac{\partial^2\psi_2}{\partial x^2}-\frac{\partial^2\psi_2}{\partial z^2}+\frac{\partial}{\partial y}\left(\frac{\partial\psi_1}{\partial x}+\frac{\partial\psi_3}{\partial z}\right)=-\mu\frac{\partial j_2}{\partial t}\tag{17}$$

$$\frac{\partial^2\psi_3}{\partial t^2}-\frac{\partial^2\psi_3}{\partial x^2}-\frac{\partial^2\psi_3}{\partial y^2}+\frac{\partial}{\partial z}\left(\frac{\partial\psi_1}{\partial x}+\frac{\partial\psi_2}{\partial y}\right)=-\mu\frac{\partial j_3}{\partial t}\tag{18}$$

If the electric field also satisfies Gauss's law

$$\nabla\cdot\boldsymbol{E}=\frac{\partial\psi_1}{\partial x}+\frac{\partial\psi_2}{\partial y}+\frac{\partial\psi_3}{\partial z}=\frac{\rho_e}{\epsilon}\tag{19}$$

then we obtain the following relations

$$\frac{\partial}{\partial x}\left(\frac{\partial\psi_2}{\partial y}+\frac{\partial\psi_3}{\partial z}\right)=\frac{\partial}{\partial x}\left(\frac{\rho_e}{\epsilon}-\frac{\partial\psi_1}{\partial x}\right)=-\frac{\partial^2\psi_1}{\partial x^2}+\frac{\partial}{\partial x}\left(\frac{\rho_e}{\epsilon}\right)\tag{20}$$

$$\frac{\partial}{\partial y}\left(\frac{\partial \psi_1}{\partial x}+\frac{\partial \psi_3}{\partial z}\right)=\frac{\partial}{\partial y}\left(\frac{\rho_e}{\epsilon}-\frac{\partial \psi_2}{\partial y}\right)=-\frac{\partial^2 \psi_2}{\partial y^2}+\frac{\partial}{\partial y}\left(\frac{\rho_e}{\epsilon}\right) \tag{21}$$

$$\frac{\partial}{\partial z}\left(\frac{\partial \psi_1}{\partial x}+\frac{\partial \psi_2}{\partial y}\right)=\frac{\partial}{\partial z}\left(\frac{\rho_e}{\epsilon}-\frac{\partial \psi_3}{\partial z}\right)=-\frac{\partial^2 \psi_3}{\partial z^2}+\frac{\partial}{\partial z}\left(\frac{\rho_e}{\epsilon}\right) \tag{22}$$

From Equations (16-18) together with relations given in Equations (20-22), we obtain, in vector form, the wave equation for the electric field as

$$\frac{\partial^2 \boldsymbol{E}}{\partial t^2}-\nabla^2 \boldsymbol{E}=\nabla\left(\frac{\rho_e}{\epsilon}\right)-\mu\frac{\partial \boldsymbol{J}_e}{\partial t} \tag{23}$$

where $\boldsymbol{J}_e=\left(j_1, j_2, j_3\right)$. Similarly for the magnetic field $\boldsymbol{B}=\left(B_x, B_y, B_z\right)=\left(\psi_4, \psi_5, \psi_6\right)$ we obtain the following equations and relations

$$\frac{\partial^2 \psi_4}{\partial t^2}-\frac{\partial^2 \psi_4}{\partial y^2}-\frac{\partial^2 \psi_4}{\partial z^2}+\frac{\partial}{\partial x}\left(\frac{\partial \psi_5}{\partial y}+\frac{\partial \psi_6}{\partial z}\right)=0 \tag{24}$$

$$\frac{\partial^2 \psi_5}{\partial t^2}-\frac{\partial^2 \psi_5}{\partial x^2}-\frac{\partial^2 \psi_5}{\partial z^2}+\frac{\partial}{\partial y}\left(\frac{\partial \psi_4}{\partial x}+\frac{\partial \psi_6}{\partial z}\right)=0 \tag{25}$$

$$\frac{\partial^2 \psi_6}{\partial t^2}-\frac{\partial^2 \psi_6}{\partial x^2}-\frac{\partial^2 \psi_6}{\partial y^2}+\frac{\partial}{\partial z}\left(\frac{\partial \psi_4}{\partial x}+\frac{\partial \psi_5}{\partial y}\right)=0 \tag{26}$$

$$\nabla \cdot \boldsymbol{B}=\frac{\partial \psi_4}{\partial x}+\frac{\partial \psi_5}{\partial y}+\frac{\partial \psi_6}{\partial z}=0 \tag{27}$$

$$\frac{\partial}{\partial x}\left(\frac{\partial \psi_5}{\partial y}+\frac{\partial \psi_6}{\partial z}\right)=-\frac{\partial^2 \psi_4}{\partial x^2} \tag{28}$$

$$\frac{\partial}{\partial y}\left(\frac{\partial \psi_4}{\partial x}+\frac{\partial \psi_6}{\partial z}\right)=-\frac{\partial^2 \psi_5}{\partial y^2} \tag{29}$$

$$\frac{\partial}{\partial z}\left(\frac{\partial \psi_4}{\partial x}+\frac{\partial \psi_5}{\partial y}\right)=-\frac{\partial^2 \psi_6}{\partial z^2} \tag{30}$$

$$\frac{\partial^2 \boldsymbol{B}}{\partial t^2}-\nabla^2 \boldsymbol{B}=0 \tag{31}$$

Journal of Modern Physics, 2019, 10, 1394-1400
https://www.scirp.org/journal/jmp
ISSN Online: 2153-120X
ISSN Print: 2153-1196

Control of Deuteron Ions to Escape from the Magnetic Mirror Bottle by a Perpendicular Supplemental Mirror

Mitsuaki Nagata

Soft Creator Company, Shinmachi, Nakagyo-ku, Kyoto, Japan
Email: nagata@heian-kogyo.jp

How to cite this paper: Nagata, M. (2019) Control of Deuteron Ions to Escape from the Magnetic Mirror Bottle by a Perpendicular Supplemental Mirror. *Journal of Modern Physics*, **10**, 1394-1400.
https://doi.org/10.4236/jmp.2019.1011092

Received: June 28, 2019
Accepted: October 26, 2019
Published: October 29, 2019

Copyright © 2019 by author(s) and Scientific Research Publishing Inc.
This work is licensed under the Creative Commons Attribution International License (CC BY 4.0).
http://creativecommons.org/licenses/by/4.0/
Open Access

Abstract

We have inquired into a means to decrease the number of charged particles escaping from a loss cone of a magnetic mirror reactor as many as possible. We previously reported the way of installing a supplemental magnetic mirror (which has a cyclotron heating space within) at the exit of a main magnetic bottle. The cyclotron heating space was set to increase a reflection-efficiency of the supplemental mirror. We could not suppress the loss of the escaping deuteron ions sufficiently even with a very long mirror and a very powerful electric field. Then, in this work we propose a new plan of installing another supplemental mirror besides the previous supplemental mirror. A new mirror is set perpendicularly to the center axis of the main bottle. By the addition of the perpendicular mirror, an efficiency of sending back of escaping deuteron ions is considerably theoretically improved. Also in the previous work, since we did not touch how to supply a high-frequency electric field to the cyclotron heating space, here we consider supplying it by an extraordinary-wave with a cyclotron frequency. It is mentioned that propagation of an extraordinary-wave with an electron cyclotron frequency depends on a magnetic field strength and density of escaping electrons.

Keywords

Magnetic Mirror Reactor, Control of Escaping Deuteron Ions, Electron and Deuteron Ion Heating by Extraordinary Waves

1. Introduction

It is considered that the most sincere problem in research with respect to a fusion reactor of magnetic mirror-type is that escaping loss of charged particles from the loss cone is still too much [1]. We first examined a means [2] of setting

a supplemental magnetic mirror (with a cyclotron resonance space within) at the exit of a main magnetic bottle. The principal aim in Ref. [2] was to reduce the half-vertical angle (called the loss angle) of the loss cone by the cyclotron resonance heating [3]. However, we could not sufficiently suppress the loss of escaping deuteron ions even with a very powerful electric field and a very long magnetic mirror. So, we proposed introduction of a means for replenishing a large quantity of deuteron ions from the outside. But in this work, we mention an idea that, by setting another supplemental magnetic mirror (called Perp-mirror) perpendicularly to the center line of the supplemental mirror (called Para-mirror) which is set in parallel with the center line of the main bottle, we may be able to induce "most of charged particles escaping from the exit (plane $d_1d_0d_4$ in **Figure 1**) of Para-mirror" outside the loss cone of Perp-mirror. Based on this idea, we mention in §3 a new plan to reclaim escaping charged particles themselves.

We did not touch in Ref. [2] how to supply a high frequency electric field to the cyclotron resonance heating space. Then, in this work we consider transmitting an extraordinary wave with an electron cyclotron frequency or with a cyclotron frequency for a deuteron ion D^+ to a heating space. It is mentioned in §2 that propagation of an extraordinary wave with an electron cyclotron frequency depends on plasma density and magnetic field strength.

2. Heating by an Extraordinary Wave

The refractive index n_x [4] [5] [6] [7] for an extraordinary wave (called X-wave) with a frequency ω is given by

$$n_x^2 = \frac{\left(1-\beta_i^2\right)\left(1-\beta_e^2\right)-2\alpha^2\left(1-\beta_i\beta_e\right)+\alpha^4}{\left(1-\beta_i^2\right)\left(1-\beta_e^2\right)-\alpha^2\left(1-\beta_i\beta_e\right)} \tag{1}$$

Here,

$$\beta_e = \omega_c/\omega, \quad \beta_i = \omega_i/\omega,$$

$\omega_c \simeq qB/m_e$, an electron cyclotron frequency

(B: a magnetic field strength, $-q$: the electron charge, m_e: the rest mass of an electron),

$\omega_i \simeq qB/m_i$, a cyclotron frequency for a deuteron ion D^+ (a deuteron mass $m_i \simeq 3680m_e$),

$$\alpha^2 = \left(\frac{\omega_{pe}}{\omega}\right)^2 + \left(\frac{\omega_{pi}}{\omega}\right)^2$$

$\omega_{pe} = \left(\frac{n_e q^2}{m_e \varepsilon_0}\right)^{1/2}$ a plasma frequency for electrons (n_e: electron density, ε_0: the dielectric constant of vacuum),

$\omega_{pi} = \left(\frac{n_i q^2}{m_i \varepsilon_0}\right)^{1/2}$ a plasma frequency for ions (n_i: deuteron ion density = n_e)

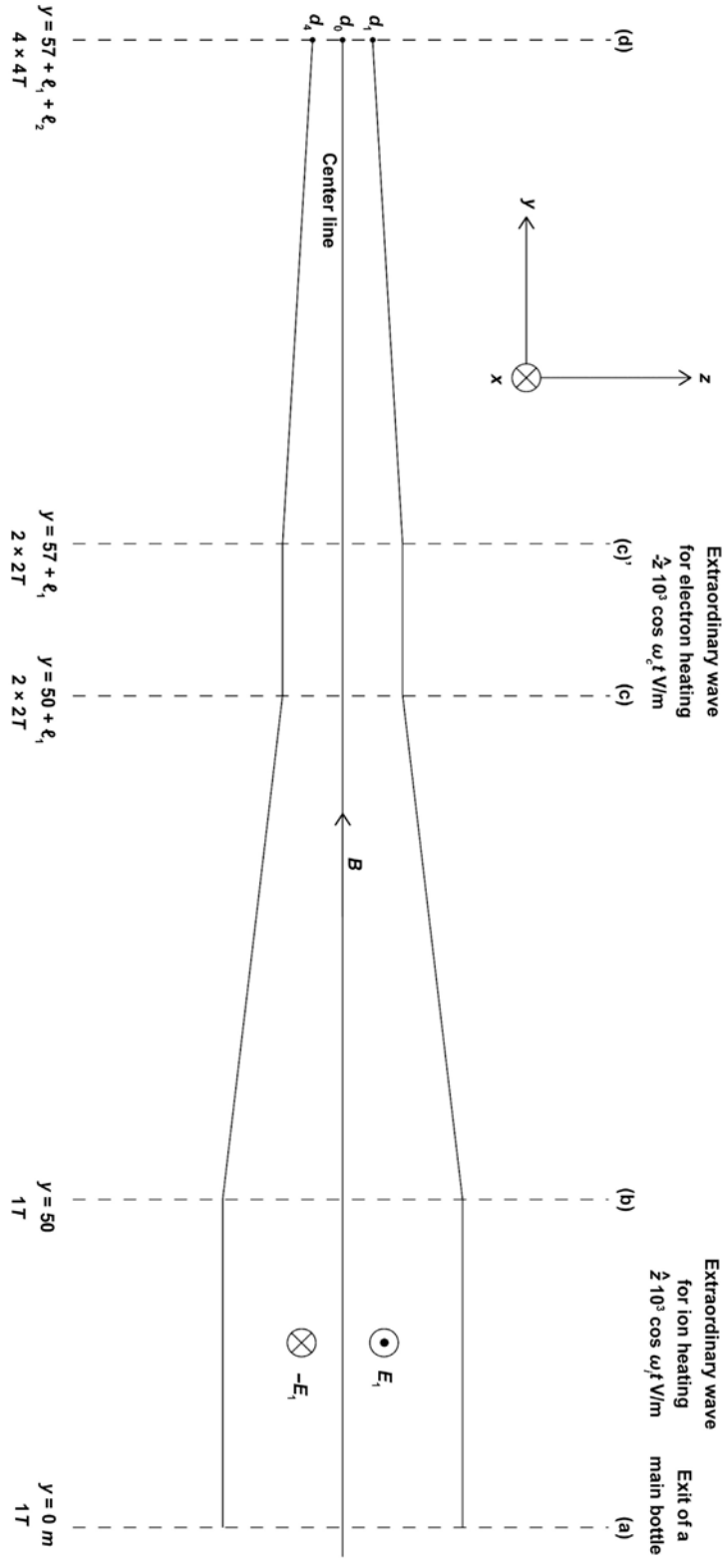

Figure 1. A supplemental magnetic mirror (called Para-mirror) for reclaiming charged particles to escape from the exit (plane (a)) of the main bottle. Constant electric fields $\pm\boldsymbol{E}_1$ V/m are for making charged particles go near the central plane perpendicular to the z-axis, $\boldsymbol{B}$ is a magnetic field which is a function of position.

We examine whether two kinds of X-wave with frequencies ω_c and ω_i can pass through a plasma.

2.1. About X-Wave with $\omega = \omega_c$

Since $\beta_e = 1$ and $\beta_i = \omega_i/\omega_c = m_e/m_i \ll 1$ we have

$$n_x^2 \simeq \frac{-2\alpha^2 + \alpha^4}{-\alpha^2} = 2 - \alpha^2 > 0 \quad \text{or} \quad \alpha^2 < 2 \tag{2}$$

When a value of B is set, an upper limit of n_e is determined from (2). We consider a supplemental mirror (Para-mirror) as shown in Figure 1. X-wave with $\omega = \omega_c$ is supplied between planes (c) and (c)'. Then, we have

$$B = 4\text{T},$$

$$\omega_c = 0.704 \times 10^{12}\ \text{sec}^{-1},$$

$$\alpha^2 \simeq \left(\omega_{pe}/\omega_c\right)^2 < 2 \quad \text{or} \quad \omega_{pe} \lesssim 10^{12}, \therefore n_e \lesssim 3 \times 10^{20}\ \text{m}^{-3}. \tag{3}$$

Since it is presumed that a target density for electron density in a main bottle is $10^{21}\ \text{m}^{-3}$, we have set an electron heating space behind mirror (b)-(c).

2.2. About X-Wave with $\omega = \omega_i$

We set a heating space for deuteron ions D^+ between planes (a)-(b). Since $\alpha^2 > 2$, $\beta_i = 1$ and $\beta_e = \omega_c/\omega_i = m_i/m_e \gg 1$, we have from (1)

$$n_x^2 \simeq \frac{2\alpha^2\beta_e + \alpha^4}{\alpha^2\beta_e} > 0 \tag{4}$$

There is no essential restriction for values of α^2 and β_e.

3. Sending Back of Escaping Deuteron Ions by a Perpendicular Mirror

Even if Para-mirror of such a large scale as shown in Figure 1 is used, it is clear, based on the examination in Ref. [2], that the escaping loss of charged particles is still too large. Then, we propose a means of installing another magnetic mirror (Perp-mirror) perpendicularly to the center line of the Para-mirror, as shown in Figure 2. Using Perp-mirror, we plan to reclaim charged particles themselves escaping from Para-mirror. In Figure 2, plane $d_1d_0d_4$ is the exit of Para-mirror. It is assumed that most of the magnetic force lines coming out of plane $d_1d_0d_4$ enter into surfaces a_1a_2 and a_3a_4 of the ferromagnetic substance. Our plan to reclaim deuteron ions (called the test ions) escaping from plane d_1d_0 and going to surface a_1a_2 is through the following procedure:

1) Under the force in the direction of $\boldsymbol{E}_1 \times \boldsymbol{B}_1$ ($\boldsymbol{E}_1$: a constant electric field, $\boldsymbol{B}_1$: a magnetic field which is a function of position), the test ions get out of region $d_1d_0a_2a_1$, pass through plane a_2a_3 and go to plane b_2b_3. Here, it is expected that each incident angle of the test ions when passing plane b_2b_3 (each inclination from the direction parallel to the centerline) is considerably smaller than 90˚.

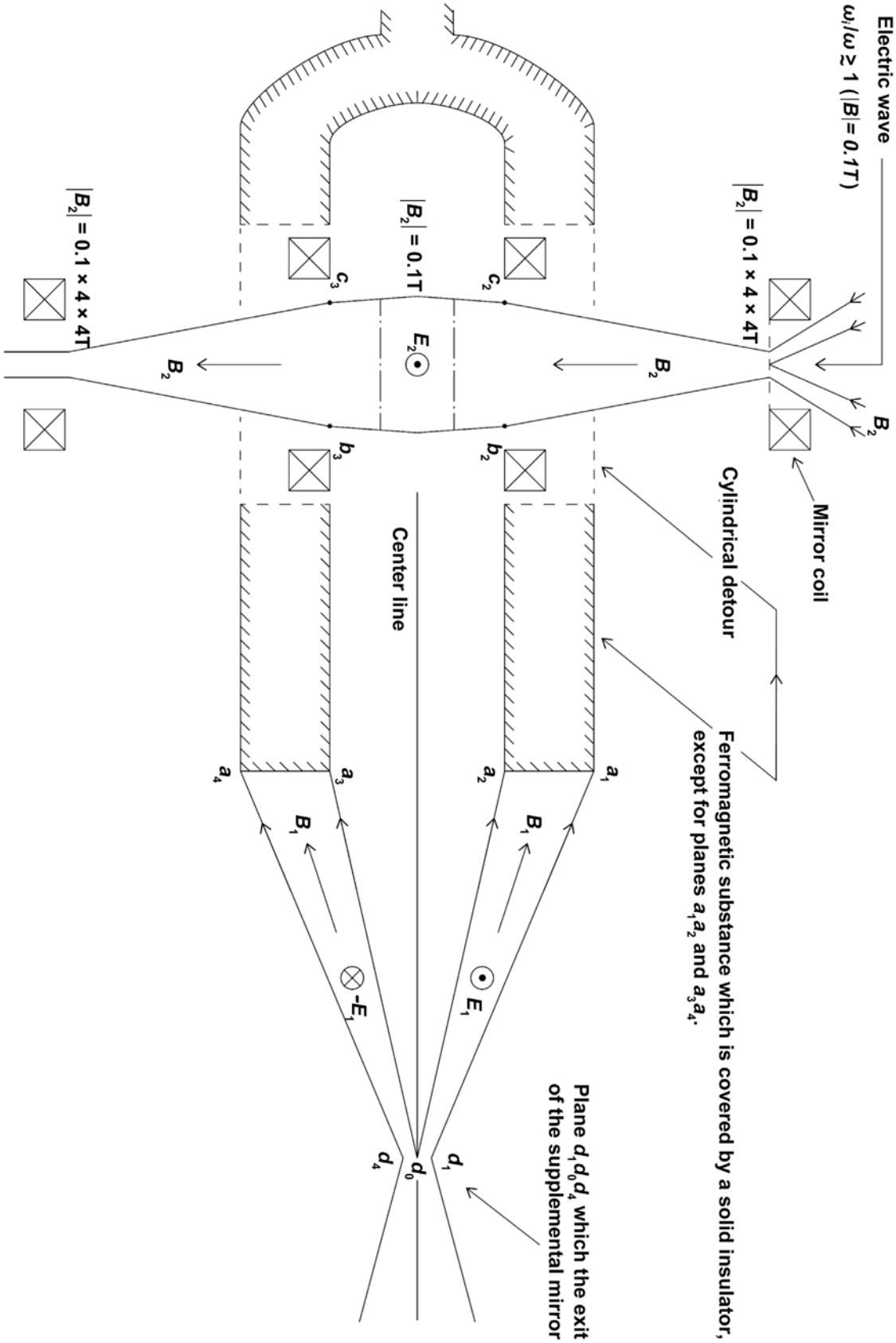

Figure 2. A schematic diagram of an apparatus (called Perp-mirror) to reclaim the escaping deuteron ions.

2) Magnetic fields in the central part and the exit of Perp-mirror are 0.1 T, 0.1 × 4 × 4 T, respectively. The loss angle of this mirror is 14.5˚. Then, the test ions having entered within region $b_2b_3c_3c_2$ will begin roundtrip motions between the upper and lower reflection-parts of Perp-mirror.

3) In the above situation, when a constant electric field $\boldsymbol{E}_2$ is supplied within the central part $b_2b_3c_3c_2$, as shown in Figure 2, the test ions drift in the direction of $\boldsymbol{E}_2\times\boldsymbol{B}_2$ ($\boldsymbol{B}_2$: a magnetic field which is a function of position) and finally jump out in the right-hand side of plane b_2b_3. These test ions are expected to return to plane $d_1d_0d_4$. It should be noted that a part of particles may collide with planes a_1a_2, a_3a_4, a_2b_2, a_3b_3 and may become loss particles.

Since it can be expected that deuteron ions will not rush to the exits of Perp-mirror, an electric wave can be transmitted in parallel with the center line of Perp-mirror, by diverting aside the directions of the strong magnetic force lines from the mirror axis, as shown in Figure 2. The wave with the frequency ω which satisfies $\omega_i/\omega \gtrsim 1$ $\left(\omega_i = q\left|\boldsymbol{B}_2\right|/m_i, \left|\boldsymbol{B}_2\right| = 0.1\text{ T}\right)$ can pass through Perp-mirror. The left-circularly polarized wave contributes to heating of deuteron ions. From the examination in Ref. [2], in order to shorten the length between planes (a) and (b) in Figure 1 but to heat heavy deuteron ions sufficiently, another heating region is necessary.

In this plan, the troublesome problem is that a necessary magnitude for $\boldsymbol{E}_1$ and a necessary length for d_0a_2 are extremely large. A ratio of $\left|\boldsymbol{E}_1\times\boldsymbol{B}_1\right|/\boldsymbol{B}_1^2$ $\left(\boldsymbol{E}_1\perp\boldsymbol{B}_1\right)$ to the mean thermal velocity $\bar{v}_i$ $\left(\simeq 2\times10^6\text{ m/s}\right)$ of deuteron ions at temperature 4×10^8 K is given by, for instance, when $\left|\boldsymbol{B}_1\right| = 16$ T and $\left|\boldsymbol{E}_1\right| = 20\times10^4$ V/m,

$$\frac{\left|\boldsymbol{E}_1\right|}{\left|\boldsymbol{B}_1\right|}:\bar{v}_i = \frac{20\times10^4}{16}:2\times10^6 = 1:160 \tag{5}$$

Even if such a powerful electric field is used, a necessary length for d_0a_2 is about $160\left(d_1d_0\right)$. However, this problem can be solved by setting constant electric fields $\pm\hat{x}\left|\boldsymbol{E}_1\right|$ also in the space with the smaller magnetic field 1 T between planes (a)-(b) in Figure 1.

4. Conclusions

We have mentioned the means for sending back most of escaping charged particles to the main bottle by the help of Para-mirror (Figure 1) and Perp-mirror (Figure 2). An efficiency of sending back depends on whether charged particles escaping from plane $d_1d_0d_4$ can pass through plane b_2b_3 or not. As a simple countermeasure, it is considered to make $\left|\boldsymbol{E}_1\right|$ between planes d_1d_4 and a_1a_4 smaller and instead to make $\left|\boldsymbol{E}_1\right|$ between planes (a) and (b) of Figure 1 bigger. Also, it is necessary to decrease the number of charged particles escaping from plane $d_1d_0d_4$ as many as possible, because scatterings (collisions) by the Coulomb forces ought to obstruct an orderly drift-movement in the direction of $\boldsymbol{E}_1\times\boldsymbol{B}_1$.

Further, we consider that charged particles heating should be done outside the

main bottle in order not to disturb the stability of a plasma within the main bottle. Both Para-mirror and Perp-mirror are heaters to warm charged particles very slowly.

Conflicts of Interest

The author declares no conflicts of interest regarding the publication of this paper.

References

[1] Ågren, Å.O. and Moiseenko, V.E. (2014) *Plasma Physics and Controlled Fusion*, **56**, Article ID: 095026.

[2] Nagata, M. and Sawada, K. (2019) *Journal of Modern Physics*, **10**, 145-156.

[3] Ivanov, A.A., Burdakov, A.V. and Bagryansky, P.A. (2015) *Fusion Science and Technology*, **68**, 56.

[4] Sitenko, A.G. and Stepanov, K.N. (1957) *Journal of Experimental and Theoretical Physics*, **4**, 512.

[5] Linhart, J.G. (1960) Plasma Physics. North Holland, Amsterdam.

[6] Stix, T.H. (1962) The Theory of Plasma Waves. McGraw-Hill, New York.

[7] Allis, W.P., Buchsbaum, S.J. and Bers, A. (1963) Waves in Anisotropic Plasmas. MIT Press, Cambridge, Mass.

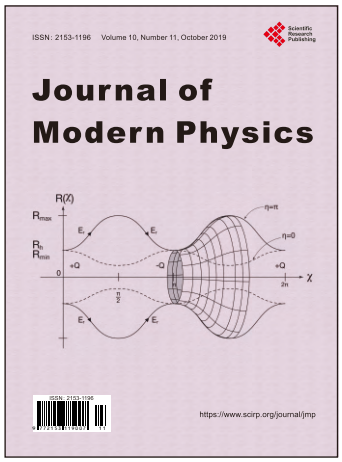

Call for Papers

Journal of Modern Physics

ISSN: 2153-1196 (Print) ISSN: 2153-120X (Online)
https://www.scirp.org/journal/jmp

Journal of Modern Physics **(JMP)** is an international journal dedicated to the latest advancement of modern physics. The goal of this journal is to provide a platform for scientists and academicians all over the world to promote, share, and discuss various new issues and developments in different areas of modern physics.

Editor-in-Chief

Prof. Yang-Hui He City University, UK

Subject Coverage

Journal of Modern Physics publishes original papers including but not limited to the following fields:

Biophysics and Medical Physics
Complex Systems Physics
Computational Physics
Condensed Matter Physics
Cosmology and Early Universe
Earth and Planetary Sciences
General Relativity
High Energy Astrophysics
High Energy/Accelerator Physics
Instrumentation and Measurement
Interdisciplinary Physics
Materials Sciences and Technology
Mathematical Physics
Mechanical Response of Solids and Structures
New Materials: Micro and Nano-Mechanics and Homogeneization
Non-Equilibrium Thermodynamics and Statistical Mechanics
Nuclear Science and Engineering
Optics
Physics of Nanostructures
Plasma Physics
Quantum Mechanical Developments
Quantum Theory
Relativistic Astrophysics
String Theory
Superconducting Physics
Theoretical High Energy Physics
Thermology

We are also interested in: 1) Short Reports—2-5 page papers where an author can either present an idea with theoretical background but has not yet completed the research needed for a complete paper or preliminary data; 2) Book Reviews—Comments and critiques.

Notes for Intending Authors

Submitted papers should not have been previously published nor be currently under consideration for publication elsewhere. Paper submission will be handled electronically through the website. All papers are refereed through a peer review process. For more details about the submissions, please access the website.

Website and E-Mail

https://www.scirp.org/journal/jmp **E-mail: jmp@scirp.org**

What is SCIRP?

Scientific Research Publishing (SCIRP) is one of the largest Open Access journal publishers. It is currently publishing more than 200 open access, online, peer-reviewed journals covering a wide range of academic disciplines. SCIRP serves the worldwide academic communities and contributes to the progress and application of science with its publication.

What is Open Access?

All original research papers published by SCIRP are made freely and permanently accessible online immediately upon publication. To be able to provide open access journals, SCIRP defrays operation costs from authors and subscription charges only for its printed version. Open access publishing allows an immediate, worldwide, barrier-free, open access to the full text of research papers, which is in the best interests of the scientific community.

- High visibility for maximum global exposure with open access publishing model
- Rigorous peer review of research papers
- Prompt faster publication with less cost
- Guaranteed targeted, multidisciplinary audience

Scientific Research Publishing

Website: https://www.scirp.org

Subscription: sub@scirp.org

Advertisement: service@scirp.org